

# **Investigation of light-induced defects in hydrogenated amorphous silicon by low temperature annealing and pulsed degradation**

DISSERTATION

zur Erlangung des Doktorgrades  
der Naturwissenschaften  
(Dr. rer. nat.)

dem  
Fachbereich Physik  
der Philipps-Universität Marburg  
vorgelegt von

**Stephan Heck**  
aus Karlsruhe

Marburg/Lahn 2002

Vom Fachbereich Physik der Philipps-Universität Marburg/Lahn  
als Dissertation angenommen am: 16. Oktober 2002

Erstgutachter: Prof. Dr. W. Fuhs  
Zweitgutachter: Prof. Dr. P. Thomas

Tag der Disputation: 4. November 2002

*Dedicated to*

*Maria Heck*

*and*

*Solveig Anders*

# Table of contents

<b><u>ZUSAMMENFASSUNG</u></b> .....	<b>6</b>
<b><u>TABLE OF SYMBOLS</u></b> .....	<b>9</b>
<b><u>1. INTRODUCTION</u></b> .....	<b>11</b>
<b><u>2. FUNDAMENTALS</u></b> .....	<b>16</b>
2.1. PHOTOCONDUCTIVITY IN HYDROGENATED AMORPHOUS SILICON (A-Si:H) .....	16
2.2. LOCATION OF RECOMBINATION CENTERS IN THE BANDGAP AND THEIR MEASUREMENT WITH THE CONSTANT PHOTOCURRENT METHOD (CPM) .....	18
2.2.1. <i>Occupancy of the gap states: shallow and deep defect states</i> .....	19
2.2.2. <i>The constant photocurrent method (CPM)</i> .....	23
2.3. ANNEALING OF LIGHT-INDUCED DEFECTS .....	25
<b><u>3. EXPERIMENTAL DETAILS</u></b> .....	<b>28</b>
3.1. SAMPLES .....	28
3.2. SET-UP .....	29
3.3. DUAL WAVELENGTH CONSTANT PHOTOCURRENT METHOD (DWCPM) .....	31
3.4. THE INVERSE MOBILITY LIFETIME PRODUCT ( $\mu\tau$ ) <sup>-1</sup> .....	33
3.4.1. <i>Defects determining photoconductivity</i> .....	33
3.4.2. <i>(<math>\mu\tau</math>)<sup>-1</sup> during light soaking</i> .....	34
3.5. LIGHT-SOAKING AND ANNEALING PROCEDURES .....	37
3.5.1. <i>Pulsed or ‘interrupted’ continuous light-induced degradation</i> .....	37
3.5.2. <i>Measurements at room temperature: Isochronal step-wise annealing</i> .....	40
3.5.3. <i>Measurements at elevated temperatures: Light-induced degradation and         isothermal annealing at elevated temperature</i> .....	41
<b><u>4. CREATION AND ANNEALING OF LIGHT-INDUCED DEFECTS</u></b> .....	<b>45</b>
4.1. PULSED VERSUS CONTINUOUS DEGRADATION .....	45
4.1.1. <i>Pulsed degradation with constant pulse length</i> .....	45
4.1.2. <i>The rise of the sample temperature during illumination</i> .....	49
4.1.3. <i>Pulsed degradation with constant duty cycle</i> .....	50
4.1.4. <i>Consequences and concluding remarks on pulsed degradation of a-Si:H</i> .....	51

---

<u>4.2. ANNEALING OF LIGHT INDUCED DEFECTS</u> .....	53
<u>4.2.1. Isochronal step-wise annealing</u> .....	53
<u>4.2.2. Isothermal annealing at elevated temperatures</u> .....	61
<u>4.2.3. Connection between step-wise isochronal and isothermal annealing</u> .....	69
<u>4.3. LIGHT-INDUCED DEGRADATION AT ELEVATED TEMPERATURES</u> .....	73
<u>4.4. SUMMARY OF RESULTS</u> .....	81
<b><u>5. DISCUSSION</u></b> .....	<b>82</b>
<u>5.1. ONE OR TWO LIGHT-INDUCED RECOMBINATION CENTERS?</u> .....	82
<u>5.1.1 One-defect model</u> .....	83
<u>5.1.2 Two-defect model</u> .....	85
<u>5.2. CONSEQUENCES OF A SECOND RECOMBINATION CENTER</u> .....	87
<u>5.2.1. Linear relationship between <math>(\mu\tau)^{-1}</math> and <math>\alpha_{1,25}</math></u> .....	89
<u>5.2.2. Temperature dependence of light-induced degradation</u> .....	90
<u>5.2.3. Annealing of pr-centers</u> .....	92
<u>5.2.4. Change in <math>(\mu\tau)^{-1}</math> degradation for long exposure times</u> .....	92
<u>5.3. <math>\tilde{\alpha}_{1,1}</math> DURING DEGRADATION AND ANNEALING</u> .....	94
<u>5.4. SIMULATION</u> .....	98
<u>5.5. SUMMARY AND CONCLUSIONS</u> .....	101
<b><u>REFERENCES</u></b> .....	<b>104</b>
<b><u>ACKNOWLEDGEMENTS</u></b> .....	<b>109</b>

## Zusammenfassung

Nach 25 Jahren zum Teil intensiver Forschung ist die lichtinduzierte Degradation der elektronischen Eigenschaften des hydrogenisiertem amorphen Siliziums (a-Si:H) [1], noch immer nicht verstanden [2]. Bei diesem sogenannten Staebler-Wronski Effekt (SWE) handelt es sich um die Verringerung der Dunkel- und Photoleitfähigkeit des a-Si:H durch Beleuchtung dieses Materials mit Licht von der Intensität der Sonneneinstrahlung ( $\approx 100 \text{ mW/cm}^2$ ). Dies ist besonders für die Anwendung des a-Si:H in Solarzellen von erheblichem Nachteil, ist aber auch für andere großflächige Anwendung von Bedeutung, wie z.B. in Flachbildschirmen. Der SWE ist metastabil: die lichtinduzierte Degradation kann durch Ausheilen des Materials bei Temperaturen über  $150^\circ\text{C}$  wieder rückgängig gemacht werden. Ein wichtiger Schritt auf der Suche nach den Ursachen des SWE war 1980/81 die Entdeckung, dass mit der Degradation der elektronischen Eigenschaften auch die Dichte der neutralen ungesättigten Siliziumvalenzen (die sogenannten "dangling bonds"), ansteigt [3, 4]. Die zwei damit verbundene Kernfragen, nämlich wie diese dangling bonds mikroskopisch entstehen und in welchen Zusammenhang sie mit dem SWE stehen, sind jedoch immer noch offen.

Der mikroskopische Entstehungsprozess der dangling bonds wird in dieser Arbeit durch Degradationsexperimente mit gepulstem Licht untersucht. Gepulste Beleuchtung kann Degradationsprozesse aufspüren, deren Zeitkonstanten im Bereich der Pulslängen liegen. Im Gegensatz zur herkömmlichen gepulsten Laserdegradation sind in der vorliegenden Arbeit Lichtintensitäten für die gepulste Degradation verwendet worden, die den Vergleich mit Degradation durch kontinuierliche Beleuchtung gleicher Intensität erlauben. Es ergibt sich eine Obergrenze für die Degradationszeitkonstante (die langsamer sein kann als die Rekombination lichtinduzierten Ladungsträger) von  $40 \mu\text{s}$  [5]. Über die ursprüngliche Fragestellung hinaus haben die Ergebnisse der gepulsten Degradationsexperimente gezeigt, dass die Photoleitfähigkeit zu einem unerwarteten großen Maß bereits bei Zimmertemperatur ausheilt.

Die Ausheilung der Photoleitfähigkeit bei Zimmertemperatur führt unmittelbar zu der Frage, wodurch die Photoleitfähigkeit im a-Si:H bestimmt wird. Dabei gelangt man zur Problematik der Rekombination lichtinduzierter Ladungsträger im a-Si:H, die besonders beim SWE deutlich wird.

Aus dem Anstieg der dangling bond Dichte wurde geschlossen, dass diese die dominierenden Rekombinationskanäle im a-Si:H sind und deshalb der SWE unmittelbar mit dem Anstieg und dem Ausheilen der DB-Dichte verbunden ist [6-8]. Dieser Ansatz steht im

Widerspruch zu den bereits 1983 veröffentlichten Resultaten von Han und Fritzsche [9], welche besagen, dass es zu einem Wert der DB-Dichte zwei Werte für die Photoleitfähigkeit gibt. Die Photoleitfähigkeit kann also nicht einzig und allein von der DB-Dichte abhängen. Han und Fritzsche schlugen als Lösung die Erzeugung zweier unabhängiger Defektarten während der lichtinduzierten Degradation vor: die eine bestimmte die Photoleitfähigkeit, die anderen seien die DBs. Bis heute ist nicht geklärt, ob die Photoleitfähigkeit tatsächlich durch einen zweiten Rekombinationskanal bestimmt wird, oder ausschließlich durch die Rekombination über DBs.

In der vorgestellten Arbeit wird diese Problematik aufgegriffen und gezeigt, wie die gemessenen Daten zusammen mit Resultaten aus der Literatur auf die Existenz mindestens eines weiteren Rekombinationszentrums hindeuten, das im weiteren als *primary recombination center* (pr-Zentrum) bezeichnet wird. Dieses pr-Zentrum hat drei wesentliche Merkmale: Es ist ein sehr effektives Rekombinationszentrum, es kann nicht mit Standardmethoden wie Elektronenspinresonanz oder optischer Absorption nachgewiesen werden, und seine Ausheilenergie ist wesentlich geringer als für die DBs.

In den besprochenen Experimenten werden a-Si:H Proben durch Beleuchtung schrittweise degradiert und ebenso schrittweise thermisch wieder ausgeheilt. Während der lichtinduzierten Degradation sind die inverse Photoleitfähigkeit und die dangling bond Dichte linear zueinander. Genau dies ist zu erwarten, wenn die dangling bonds für die Rekombination verantwortlich sind. Die Ausheilung besteht jedoch aus einem zweistufigen Prozess: Zuerst erholt sich die Photoleitfähigkeit drastisch und ohne eine wesentliche Änderung der dangling bond Dichte. Diese nimmt erst mit fortschreitender Ausheilung ab. Zusammenhänge dieser Art belegen, dass die Photoleitfähigkeit nicht alleine von der DB-Dichte abhängen kann. Mit den pr-Zentren als weiterem Rekombinationspfad ist das Verhalten der Photoleitfähigkeit jedoch leicht zu verstehen. Die pr-Zentren heilen vor den DBs aus, und da sie sehr effektive Rekombinationszentren sind, erholt sich die Photoleitfähigkeit dramatisch, ohne dass sich die DB-Dichte wesentlich ändert.

Überraschenderweise ergibt sich während der ersten Phase des Ausheilprozesses ein Anstieg der energieabhängigen optischen Defektabsorption (die als Maß für die DB Dichte dient) in einem Energiebereich, welcher den DBs oberhalb der Bandmitte zugeordnet wird. Auf den ersten Blick erscheint dies als Erhöhung der DB-Dichte, was im Widerspruch steht zur drastischen Erholung der Photoleitfähigkeit in dieser ersten Phase des Ausheilens. Es ist bemerkenswert, dass der Anstieg der Absorption während dieser ersten Phase der Ausheilung linear zu dem drastischen Anstieg der Photoleitfähigkeit ist. In dieser Arbeit wird durch eine

Simulation demonstriert, wie mit dem Ausheilen der pr-Zentren die DBs so umbesetzt werden, dass sich der erwähnte Anstieg in der Absorption ergibt.

Um die Ausheilenergien der pr-Zentren und der DBs zu bestimmen, wurden die degradierten Proben auf mehreren verschiedenen Temperaturen gehalten und jeweils die thermisch aktivierte Ausheilung verfolgt. Die Ausheilenergie der Photoleitfähigkeit ( $\approx 0.85$  eV), die der Ausheilenergie der pr-Zentren entspricht, ist um etwa 0.3 eV kleiner als die der DBs. Dabei ist zu beachten, dass dieser Wert für die Degradation bei Zimmertemperatur gilt. Es stellt sich heraus, dass die pr-Zentren mit einem Ausheilenergiespektrum erzeugt werden, deren kleinster Wert bis mindestens 0.2 eV reicht. Die Erholung der Photoleitfähigkeit, wie sie bei Zimmertemperatur beobachtet wird, ist nur der "Hochtemperaturrest" eines Erholungsvorgangs der Photoleitfähigkeit, der während der Beleuchtung kontinuierlich stattfindet.

Die große Effektivität der pr-Zentren für den Elektroneinfang lässt vermuten, dass dieser Zustand positiv geladen ist. Mögliche Kandidaten für einen solchen Zustand sind positiv geladene dangling bonds, deren Existenz oberhalb der Bandmitte vorhergesagt ist [10], oder positiv geladener mobiler Wasserstoff, der durch Dissoziation von H-Si Bindungen freigesetzt wird [11].

Dass die Kontrolle der pr-Zentren während des a-Si:H Wachstums oder durch eine Nachbehandlung eine wesentliche Verbesserung für die Anwendungen dieses Materials bedeutet, wird in dieser Arbeit durch die Untersuchung von a-Si:H Proben belegt, die auf verschiedene Weisen gewachsen wurden. Der geringste Anteil an pr-Zentren ergibt sich, wenn während des Wachstums von a-Si:H zusätzlich Wasserstoff in die Depositionskammer geleitet wird. Dieses Verfahren wird bereits kommerziell angewendet und führt zu stabileren a-Si:H Solarzellen mit höheren Wirkungsgraden. Ein erweitertes Verständnis der pr-Zentren wird zu deren verbesserten Kontrolle und dadurch zu höheren Effizienzen vor allem für großflächige Anwendungen führen, z.B. für Solarzellen, aber auch für die kommerziell wichtigen Flachbildschirme.



## Table of Symbols

Symbol	Explanation
$\alpha$	absorption coefficient
$\alpha_{hv}$	absorption coefficient at energy $h\nu$ in eV
$\tilde{\alpha}_{1.1}$	integrated $\alpha_{hv}$ for $h\nu \leq 1.1$ eV
$\eta$	duty cycle defined as $t_p/(t_p + t_d)$
$\mu$	electron mobility
$\nu$	frequency or rate
$\nu_0$	prefactor
$\sigma$	conductivity
$\sigma_d$	dark conductivity
$\sigma_{ph}$	photo conductivity
$\tau$	electron life time
$\lambda$	wavelength
$A_{CPM}$	proportionality constant between $N_{db}$ and $\alpha_{1.25}$ ( $A_{CPM} = N_{db}/\alpha_{1.25}$ )
$d$	film thickness
$E_{CB}$	conduction band mobility edge energy level
$E_{VB}$	valence band mobility edge energy level
$E_g$	bandgap
$E_F$	Fermi energy
$E_a$	annealing activation energy
$E_d$	demarcation annealing activation energy
$F$	light intensity
$G$	generation rate density
$h$	Planck's constant
$k_B$	Boltzmann factor
$l$	contact length
$M$	number of pulses
$m$	slope in a $(\mu\tau)^{-1}$ versus $\alpha_{1.25}$ plot
$n$	free electron density
$N_s$	electron spin density
$N_{db}$	density of light-induced neutral dangling bonds
$N_{pr}$	density of light-induced primary recombination centers
$p$	free hole density
$r(S)$	ratio of electron to hole capture efficiency depending on the species S
$R$	reflectance
$t$	time

$t_a$	anneal time
$t_p$	pulse length
$t_d$	time between pulses
$t_{exp}$	exposure time
$t_{tot}$	total experimental time
$T$	temperature
$T_a$	anneal temperature
$T_{exp}$	exposure temperature
$w$	contact width

<b>Abbreviation</b>	<b>Explanation</b>
CPM	constant photocurrent method
CB	conduction band
DOS	density of states
DB	dangling bond
$D^0$	neutral dangling bond
$D^+$	positively charged dangling bond
$D^-$	negatively charged dangling bond
ESR	electron spin resonance
HWCVD	hot wire chemical vapor deposition
LID	light-induced defects
pr-center	primary recombination center
PECVD	plasma enhanced chemical vapor deposition
SWE	Staebler Wronski Effect
VB	valence band

## 1. Introduction

More than 25 years ago, D. Staebler and C. Wronski discovered that the electronic quality of hydrogenated amorphous silicon (a-Si:H) degrades under illumination. Even at moderate light intensities (for example by exposure to sun light), its photo and dark conductivities decrease with illumination [1]. The deleterious influence of this Staebler-Wronski Effect (SWE) can be mitigated by various techniques, but so far it has not been possible to eliminate the SWE or even fully understand it. The lack of comprehension and the inability to completely suppress the SWE has slowed the application of this inexpensive semiconductor material, which is of particular interest for solar cell and flat panel display applications.

Research related to the SWE made an important step forward in 1980 and 1981. It was discovered that the light-induced decrease in photo and dark conductivity is accompanied by an increase in the electron spin resonance signature of the unsaturated threefold-coordinated ‘dangling’ silicon bond [3, 4]. These dangling bonds play a central role in a-Si:H. If the material contains no hydrogen, which is achieved by thermally evaporating amorphous silicon, the material has a large number of defects due to its disorder, as well as  $10^{19} - 10^{20} \text{ cm}^{-3}$  dangling bond (DB) defects [12]. Fortunately, the introduction of 2 to 15% hydrogen drastically reduces the DB density to about  $10^{15} \text{ cm}^{-3}$ . The hydrogen, which may be introduced by various deposition techniques [13-16], terminates the DBs and releases strain in the material. Such hydrogenated amorphous silicon is photoconductive and well suited for solar cells and flat panel display applications. The discovery of the increase in DB density with illumination pointed to the cause of the SWE, because the DBs have states at mid-bandgap. These states act as efficient recombination centers for photo-generated charged carriers, such that the lifetime of the photo-induced carriers (and therefore  $\sigma_{\text{ph}}$ ) decreases with increasing DB density. Further, the identification of the microscopic entity responsible for the SWE allowed researchers to examine how the DBs are created in this material. Remarkably, neither the recombination of light induced carriers nor the creation mechanism of DBs has been settled satisfactorily, despite the great amount of information that has accumulated since the discovery of the SWE [2]. In this thesis, these two crucial aspects of the SWE are investigated by utilizing photoconductivity as the principal tool.

Nearly all workers agree that the SWE originates from the light induced charged carrier recombination [17]. However, there are three competing views of the microscopic consequences: (1) The breaking of strained weak Si-Si bonds in the a-Si:H network each into two DBs [18], (2) the Si-H bond dissociation into a DB and a hydrogen atom, which diffuses

into the network [19] and (3) structural changes [20]. These structural changes might either directly influence  $\sigma_{\text{ph}}$  [21] or, by development of strain, lead to DB creation (see the discussion in [22]). A significant difference between these three mechanisms for the DB creation is their different microscopic dynamics. This difference may allow to distinguish them. In the weak-bond breaking model the time constant to reach steady state degradation is determined by the time it takes to establish a steady state concentration of recombining charged carriers. If hydrogen mediates the DB creation, its dynamics may be determined by the hydrogen [11]. Similarly, structural changes [23], like the volume expansion of a-Si:H simultaneously to the light-induced degradation of  $\sigma_{\text{ph}}$  [24], could have a distinctive dynamic behavior after it was set in motion by electron and/or hole recombination.

By degrading a-Si:H samples with pulsed illumination, this thesis establishes an upper bound for a possible slower process involved in the SWE [5]. High intensity pulsed laser illumination dramatically increases the fraction of direct electron hole recombination and is therefore highly effective in degrading a-Si:H [25-27]. In contrast to these laser pulsed degradations, the novel approach of this work is to use pulsed exposures of moderate light intensities. The intensities are low enough that the degradation of the samples can be compared with continuous (CW) illumination of same peak intensity. If the light pulses are long enough to achieve near-identical recombination dynamics as during CW illumination, but at the same time are short enough to be in the range of a possibly slower SWE time constant, then a significant difference between pulsed and CW induced degradation should be measurable [5, 28]. While such a difference is indeed observed [28], it is, however, identified with the enhanced recovery of  $\sigma_{\text{ph}}$  during pulsed degradation [5]. This enhanced recovery of  $\sigma_{\text{ph}}$  always masks a possible unique difference between pulsed and CW induced degradation and severely limits the application of this experimental approach. Because it is experimentally possible to compensate for this enhanced recovery of  $\sigma_{\text{ph}}$  during pulsed degradation, it is, nevertheless, possible to determine an upper limit for slow processes connected with the SWE [5].

The other central controversy concerns the origin of the increased recombination of light-induced charged carriers in the SWE. Soon after the discovery of the light-induced increase in DB density, the DBs were soon suspected to be the dominant recombination center in a-Si:H [6, 7]. The conclusive answer seemed to be found by Stutzmann et al., who deduced from their systematic study that only the neutral DBs ( $D^0$ s) act as recombination centers for the light induced charged carriers, and therefore are solely responsible for the SWE [8]. However, by 1983 Han and Fritzsche had already demonstrated that for one  $D^0$  density ( $N_{\text{db}}$ )

value there are two possible values for  $\sigma_{\text{ph}}$  depending on sample history [9]: While during light-induced degradation  $\sigma_{\text{ph}}$  and  $N_{\text{db}}$  are inversely proportional to each other [7, 8, 29-31], this is not the case during thermal annealing. Two distinct different regimes become visible [31, 32]: In the first regime,  $\sigma_{\text{ph}}$  recovers ‘fast’ to about 75% of its degraded value, with almost no reduction in  $N_{\text{db}}$ . Then, in the second regime, the rest of  $\sigma_{\text{ph}}$  recovers ‘slowly’ and only then, simultaneously to  $\sigma_{\text{ph}}$ ,  $N_{\text{db}}$  decreases. Han and Fritzsche [9] suggested the existence of two possibly independent defects. One controls  $\sigma_{\text{ph}}$  and anneals easily, the other is harder to anneal and can be identified with the  $D^0$ s. If, however, the  $D^0$ s were indeed the only recombination centers, then they cannot be identical. Some must have higher recombination efficiencies than others, and this recombination efficiency must be closely connected to the ease of annealing these defects [32-34]. In the investigation of the SWE, remarkably little attention has been paid to the annealing regime below about 100°C (exceptions are [31, 35-37]), where the major part of the degraded  $\sigma_{\text{ph}}$  recovers. Fig. 1.1 supports this assertion by plotting the numbers of publications that have cited the original SWE [1], the Stutzmann et al. [8] and the Han and Fritzsche [9] paper. The fast increase in citations of the original SWE paper after its publication in 1977 indicates the soaring

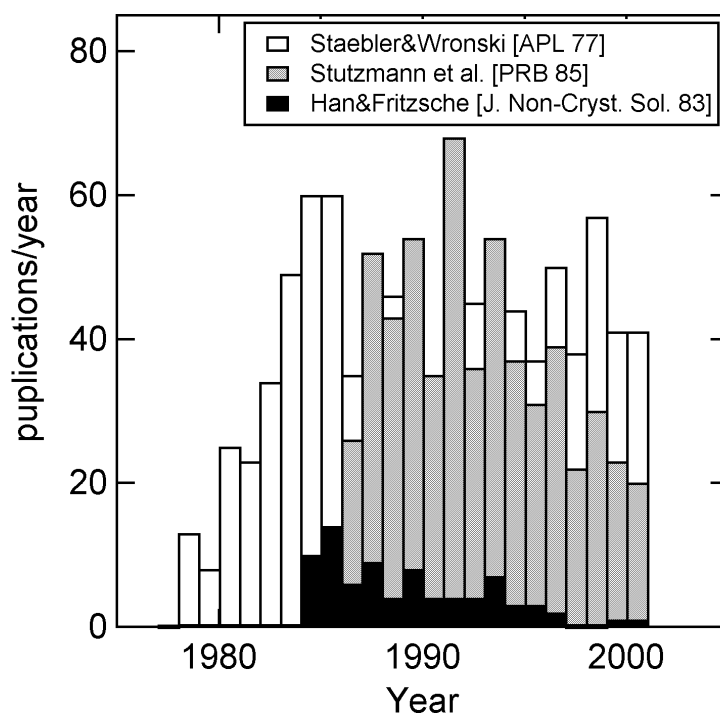


**Figure 1.1:** Number of publications per year, which quoted the three indicated publications. Result of a Science Citation Index search.

scientific and technological interest in this problem. The number of citations of Stutzmann et al.'s work shall represent here the popularity of the 'one-defect' approach described above. It appears as if, right after its publication, this paper has been quoted simultaneously whenever research in this field has dealt with the SWE. Surprisingly, the Han and Fritzsche result, which deal with  $\sigma_{\text{ph}}$ , the central subject of the SWE, and the correlation between  $\sigma_{\text{ph}}$  and  $D^0$ , has fallen into oblivion.

The second part of this thesis examines this controversial correlation between  $\sigma_{\text{ph}}$  and  $D^0$  by exploring the annealing regime below 100°C. The results are compared to the behavior of the material during light-induced degradation and to the annealing regime above 100°C. The results strongly support the Han and Fritzsche proposal of two recombination centers. We will see later that there is no conflict between this proposal and the observed inverse proportionality of  $\sigma_{\text{ph}}$  and  $D^0$  during degradation. To gain more information about the intrinsic character of a-Si:H, experiments are done with a-Si:H films deposited with various techniques, which result in materials more resistant to light-induced degradation than the conventional deposition technique. The results lead to conclusions about the creation of two kinds of defects, depending on the deposition technique.

The  $D^0$  density ( $N_{\text{db}}$ ) is measured in the experiments by optical defect absorption ( $\alpha$ ) and revealed two new and surprising effects: First,  $\alpha$  measured at the longest wavelengths *increases* during annealing, which is counterintuitive, because this increase seems to indicate an increase of defects. Such an increase has been measured previously only in low temperature exposure and anneal experiments [37]. The explanation of Stradins et al. [38], a shift in the dark Fermi level, is unsatisfactory, because the material is not in thermal equilibrium during these experiments. Also, no physical reason is given for such a shift. Second, this apparent increase in defect density is linearly proportional to the recovery of  $\sigma_{\text{ph}}$  in the first 'fast' annealing regime. Such a correlation cannot be detected in low temperature experiments, because the recombination of charged carriers at these temperatures is no longer determined by deep defects. However, assuming the creation and independent annealing of two kinds of recombination centers, a numerical simulation reproduces the behavior of  $\sigma_{\text{ph}}$  and  $\alpha$  during degradation in the fast and slow annealing regime.

From the experimental results and the simulations, a self-consistent picture of photoconductivity during light-induced degradation and thermal annealing emerges. A two-defect model appears as the most likely origin of the observed recombination processes. This thesis clearly demonstrates that any research seeking a correlation between defects and  $\sigma_{\text{ph}}$  in the framework of the SWE must cover all of the regimes identified in this thesis: degradation,

fast, and slow annealing of  $\sigma_{\text{ph}}$ . The analysis of samples deposited with various techniques in these regimes provides important information about the SWE and could lead to new approaches for even better materials. The picture of a plain neutral silicon dangling bond responsible for photoconductivity in a-Si:H is clearly too simple. In order to understand light-induced degradation of a-Si:H, it is necessary to refocus our attention on the lifetime of the charged carriers in this material.

## 2. Fundamentals

For the investigation of the light-induced photoconductivity ( $\sigma_{\text{ph}}$ ) decrease in a-Si:H (the SWE), we first have to establish by which parameters it is determined. This chapter describes fundamental aspects of  $\sigma_{\text{ph}}$ , recombination of charged carriers and annealing of light-induced defects.

### 2.1. Photoconductivity in hydrogenated amorphous silicon (a-Si:H)

This section describes the relevant parameters for the degradation of  $\sigma_{\text{ph}}$ . The disorder in a-Si:H results in strained bonds and distorted bond angles, which leads to localized states reaching into the forbidden gap from the conduction band (CB) and valence band (VB). The density of these so-called ‘tail’ states decreases roughly exponentially into the bandgap and connects smoothly with the density of states (DOS) in the CB; the same applies for the VB tail and its DOS [39, 40]. As the densities of the localized states increase towards the bands, the states overlap more and more until at certain energy levels the overlap is sufficiently large to allow charged carriers to easily move from state to state. These energy levels define mobility edges at energies  $E_{\text{CB}}$  for the CB and  $E_{\text{VB}}$  for the VB for electrons and holes, respectively. For the investigation at hand, it can safely be assumed that there is no electronic transport between the mobility edges, i.e.  $\mu_n = \mu_p = 0$  for  $E_{\text{CB}} > E > E_{\text{VB}}$ , where  $\mu_n$  and  $\mu_p$  are electron and hole mobility, respectively. For  $E > E_{\text{CB}}$  and  $E < E_{\text{VB}}$ ,  $\mu_n$  and  $\mu_p$ , respectively, can be regarded as constant, because transport will take place close to  $E_{\text{CB}}$  and  $E_{\text{VB}}$ . With these assumptions conductivity in a-Si:H can be written as:

$$\sigma = e(\mu_n n + \mu_p p), \quad (2.1)$$

with  $e$  the electron charge, and  $n$  and  $p$  the density of free electrons and holes, respectively. In a-Si:H,  $\mu_n$  is at least ten times greater than  $\mu_p$  [40-42]. In the intrinsic samples used in this study,  $n \approx p$ , and therefore electrons dominate  $\sigma$  and the hole contribution can be neglected. For simplicity,  $\mu$  stands for  $\mu_n$  throughout this thesis. Further, because the samples in this study are device quality,  $\sigma_{\text{ph}}$  is at least one order of magnitude larger than  $\sigma_{\text{d}}$  for the light intensities used in the experiments. Therefore only the contribution of the light-induced carriers to  $\sigma_{\text{ph}}$  needs to be considered. Introducing  $G$  as the generation rate density for electron-hole pairs and  $\tau$  as the electron lifetime, Equ. 2.1 becomes:



$$\sigma_{ph} = e\mu\tau G. \quad (2.2)$$

With  $\mu$  constant during light soaking [6, 43-46], all the changes in  $\sigma_{ph}$  are a result of changes in  $\tau$ . The recombination rate  $\tau^{-1}$  can be written as

$$\tau^{-1} = \sum_i C_i^{AGD} N_i^{AGD} + \sum_j C_j^{LID} N_j^{LID}, \quad (2.3)$$

where the  $N$ 's are the densities of the different recombination centers and the  $C$ 's their different proportionality constants for electron recombination. The right hand side of Equ. 2.3 consists of two terms: The first term is the sum over all the as-grown defect types acting as recombination centers, which does not change during light soaking and annealing. The second term on the right hand side represents the increase in  $\tau^{-1}$  due to light soaking. The  $N_j^{LID}$ s stand for the increase in the densities of the light-induced recombination centers, i.e. in the annealed state (commonly referred to as state A) all  $N_j^{LID} = 0$  and  $\tau^{-1}$  is determined by the as-grown recombination centers alone ( $\tau^{-1} = \sum_i C_i^{AGD} N_i^{AGD}$ ).

The physical meaning of the proportionality constants ( $C$ s) depends on how an electron is captured by the recombination centers, which is a very complex mechanism. The easiest approach is probably the ballistic model. Here, the  $C$ s are identified with the product of the thermal velocity of the photo-induced charged carrier and the capture cross section of a recombination center. A necessary requirement for this model is that the capture radius is smaller than the mean free path for scattering [47]. However, in a low mobility material like a-Si:H [40, 41, 47, 48] it must be expected that the capture depends on the difficulty of the electrons to diffuse to a recombination center [49]. Consequently, the  $C$ s will be a function of  $\mu$ . The focus of this study is, however, not to investigate the details of the capture mechanism of photo-induced charged carriers by recombination centers, but to explore how the densities of recombination centers and their proportionality constants change with light-soaking and thermal annealing. Chapter 5 will discuss the physical meaning of these changes. Here, it is therefore sufficient to summarize the capture process in the constants as defined in Equ. 2.3. This equation also covers the possibility that there are different recombination paths for the same recombination center. In this case, there are products  $CN$  in Equ. 2.3 for each of the different recombination paths of a recombination center. Each of these products for a given

recombination center has a different  $C$  that represents the different capture efficiencies for the various paths.  $N$  remains the same.

This work addresses only the light-induced changes in  $\sigma_{ph}$ . Therefore, we will concentrate on the second term on the right hand side of Equ. 2.3, which describes the increase in  $\tau^{-1}$ :

$$\Delta(\tau^{-1}) = \sum_j C_j^{LID} N_j^{LID}, \quad (2.4)$$

where  $\Delta(\tau^{-1})$  stands for the increase in the recombination rate with light soaking. From Equ. 2.4 it follows that there are only three possibilities for the origin of the Staebler-Wronski Effect (SWE): Either the  $C_j^{LID}$ , the  $N_j^{LID}$ , or both simultaneously increase under light illumination. The creation of additional recombination centers due to light-soaking is well established: As a-Si:H is light-soaked, the density of unsaturated neutral Si dangling bonds ( $N_{db}$ ), measured with electron spin resonance (ESR), increases [3, 4]. The neutral Si dangling bonds ( $D^0$ ) have deep states in the gap and therefore will act as recombination centers. However, this increase in  $N_{db}$  alone cannot explain the  $\sigma_{ph}$  data during degradation and annealing [9, 21, 31, 36, 37, 50, 51]. In Chapter 4, the central problem in the relationship between  $\sigma_{ph}$  and  $N_{db}$  will be clearly defined, and new results clarifying and elucidating this relationship will be presented. In Chapter 5, we will discuss the consequences of these results and present arguments strongly suggesting another recombination center than the  $D^0$ .

## ***2.2. Location of recombination centers in the bandgap and their measurement with the constant photocurrent method (CPM)***

As described in Section 2.1., changes in the recombination center density control  $\sigma_{ph}$  in a-Si:H during light soaking and annealing. Not each state in the bandgap acts as recombination center during illumination. For example, shallow defect states close to the mobility edges will act as traps, i.e. charged carriers captured there are more likely to be thermally reemitted to the adjacent band than to recombine. In contrast, carriers captured in states close to mid-bandgap will most likely recombine. The next section explains how the occupancy of the states in the bandgap during illumination is calculated. Demarcation levels emerge, which naturally separates shallow from deep defect states (we will use the name deep defects synonymously to recombination centers in this thesis). Further, the occupancy of the

$D^0$  states in the bandgap is a requirement for the measurement of their density with the constant photocurrent method, which is the subject of Section 2.2.2.

### 2.2.1. Occupancy of the gap states: shallow and deep defect states

In thermal equilibrium (in the dark), the occupancy of the bandgap is described by the Fermi statistics. This equilibrium is disturbed by illumination, when a non-equilibrium density of electron-hole pairs is created. A steady state establishes as soon as the continuous generation of electrons and holes is balanced by their recombination. At moderate light intensities, as used in the present investigation, recombination is dominated by capture of electrons and holes by states in the gap. For disordered materials, like a-Si:H with its continuous distribution of states, the introduction of demarcation levels leads to a convenient definition of shallow and deep defects, separating traps from recombination centers [52]. A rigorous mathematical treatment is provided by Simmons and Taylor, which is briefly described in the following.

The occupation of the states in the bandgap is determined by two mechanisms: (1) The capability of a state to capture electrons and holes and (2) the thermal excitation from such a state to the adjacent band. In a first step to calculate the occupancy function, one may assume that there is a light-induced non-equilibrium carrier concentration in the bands. We eliminate the second mechanism by considering the material at  $T = 0$ , i.e. there are no thermal excitations from anywhere in the bandgap to the adjacent bands. In this case, the occupancy is determined by the electron and hole capture efficiency of the individual state. It turns out that, for a given state at energy  $E$  in the bandgap, not the absolute value of the capture efficiencies is important, but their ratio,  $r(S)$ :

$$r(S) = \frac{C_n(S, E)}{C_p(S, E)}. \quad (2.5)$$

Here  $C_n$  and  $C_p$  stand for the capture efficiencies of a state for electrons and holes, respectively. This equation defines species ( $S$ ) of states, i.e. all states with the same ratio  $r(S)$  have the same occupancy function independent of their absolute values for  $C_n$  and  $C_p$  and their position in the bandgap. After the occupancy functions for the different species are calculated, they are combined to the final occupancy function. Equ. 2.5 represents a dramatic simplification for the calculation of the bandgap states occupation. In the wide spectrum of continuous distributions of states in the bandgap, it is easier to calculate the occupancy

function for a species (e.g. as defined in Equ. 2.5) than a detailed balance for each different state [53]. At  $T = 0$  the occupancy of states with identical  $r(S)$  is

$$f = \frac{r(S)n}{r(S)n + p}, \quad (2.6)$$

with  $f$  the occupancy function. In this case all states in the gap continuously capture the light-induced electrons and release them (capture holes), i.e. all states participate in the recombination of an electron (the same is true for the capture/release of holes). Here, all states act as recombination centers.

For finite temperatures, the thermal excitation of electrons to the CB and of holes to the VB must be considered. Instead of recombining with a hole (electron) in the VB (CB), the electron (hole) will be re-excited to the CB (VB). The influence of thermal excitation leads to a modulated Fermi function for  $f$ . For electrons above the dark Fermi energy level, this modulated Fermi function can be written as a modification of Equ. 2.6:

$$f = \frac{r(S)n}{r(S)n + p} \times \left\{ 1 + \exp\left(\frac{E - E_F^n}{kT}\right) \right\}^{-1}. \quad (2.7)$$

$E_F^n$  defines here the quasi-Fermi level for trapped electrons at which  $f$  is just one half of the modulation ( $r(S)n/\{r(S)n + p\}$ ). Below the dark Fermi energy level it is easier to demonstrate the modulated Fermi function as  $1-f$ , i.e. the occupancy of the states with holes:

$$1 - f = \frac{r(S)n}{r(S)n + p} \times \left\{ 1 + \exp\left(\frac{E - E_F^p}{kT}\right) \right\}^{-1}, \quad (2.8)$$

with the equivalent definition for the quasi-Fermi level for holes ( $E_F^p$ ). The number of states which can act as recombination centers is reduced in comparison to the  $T = 0$  case, because the charged carriers outside of the energy range between the quasi-Fermi levels are thermally re-excited into their nearest band. Now, all states between the two quasi Fermi levels act as recombination centers. Fig. 2.1 shows  $f$  for  $r(S) = 2$  and  $n = p = 10^8 \text{ cm}^{-3}$ , indicating the modulation amplitude and the quasi-Fermi levels for the trapped carriers. Two features of the

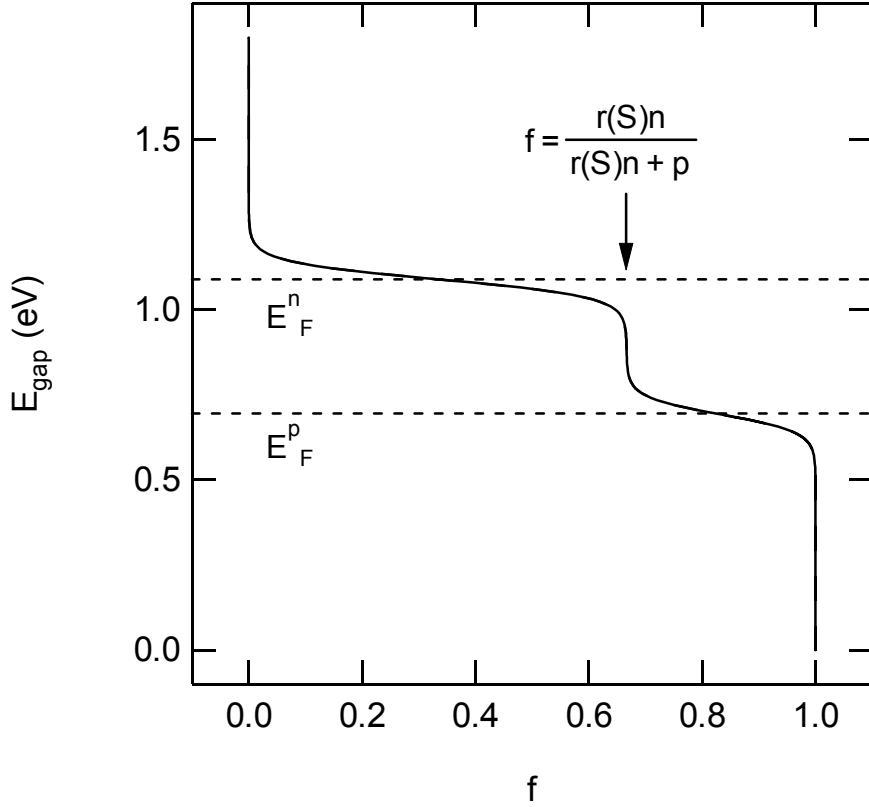


**Figure 2.1:** Occupancy function calculated with the Simmons and Taylor statistics[60] for  $n = p = 10^8 \text{ cm}^{-3}$ . The quasi-Fermi levels are indicated, as well as the modulation level.

presented statistics will be important for the discussion: (1) The quasi-Fermi levels for the trapped carriers depend significantly on  $n$  and  $p$  (Equ. 2.7 and 2.8), i.e. on the light intensity. In comparison, (2) the modulation amplitude is insensitive to light intensity (Equ. 2.6), as long as the ratio  $n/p$  remains roughly constant.

The absolute density of the electron distribution in the gap during illumination is obtained by summing up the product of  $f$  with the DOS for each individual species of states (Equ. 2.5). Typical parameters used to model the DOS are listed in table 2.1. They are taken from the investigated samples and the literature (e.g. [18, 32, 40, 54-57]). Here all energies are referenced to the VB edge. The density of  $D^0$ 's is approximated with a Gaussian [54], the tail states with an exponentially decaying function [39, 40]. The CB state density is well described by  $g(\epsilon) = 8 \times 10^{21} \times (E_{CB} - \epsilon)^{1/2} \text{ cm}^{-3} \text{ eV}^{-1}$  [58, 59], similar to the DOS in crystalline semiconductors. The DOS versus energy ( $\epsilon$ ) in the bandgap is shown in Fig. 2.2, together

$E_g$	1.8 eV
intrinsic $N_{db}$ (annealed state)	$5.0 \times 10^{15} \text{ cm}^{-3}$
$N_{db}$ : full width at half maximum	0.2 eV
maximum of $N_{db}$ at	0.7 eV
CB tail width	0.025 eV
VB tail width	0.05 eV

**Table 2.1** Bandgap parameters used for the calculations in this section.

with the product  $f_{db} \times N_{db}(\epsilon)$ , with  $f$  from Fig. 2.1 ( $N_{db}(\epsilon)$  is the density of  $N_{db}$  at a given  $\epsilon$  in the gap). This description leaves out correlation energy effects, i.e. doubly occupied negatively charged DBs ( $D^-$ ) and their occupancy. Detailed balanced calculations show that at

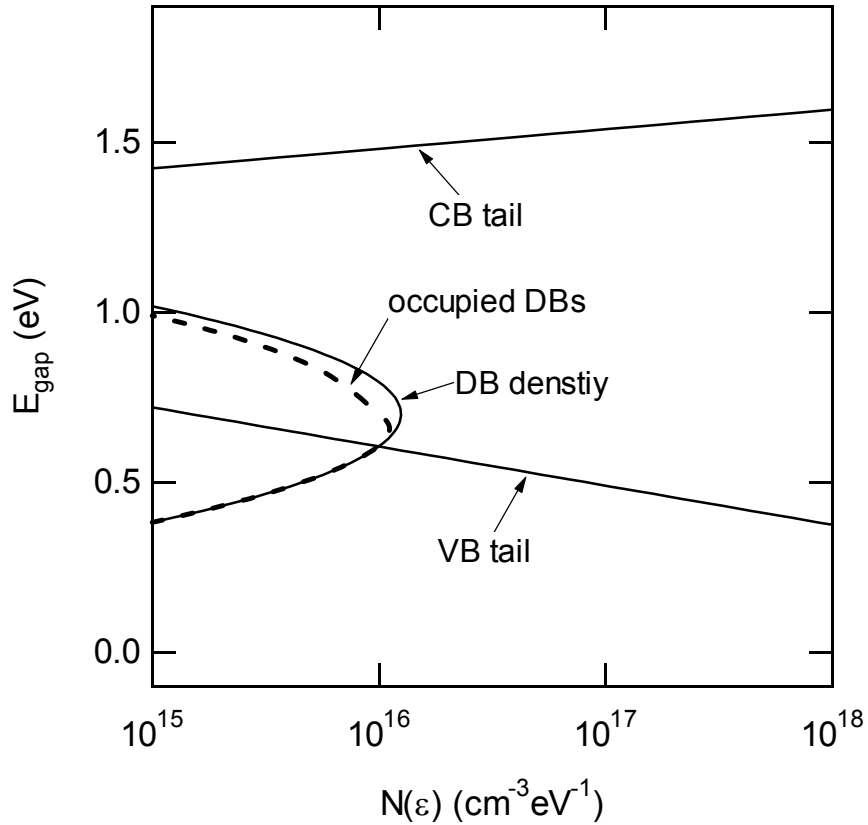


**Figure 2.2:** Model for the density of states (DOS) in the bandgap using the parameters of table 2.1. The density of DBs is approximated by a Gaussian function. The dashed line is the occupancy of the DBs calculated with the Simmons and Taylor statistics [60].

moderate light intensities less than 2% of the DBs are doubly occupied [61]. This conclusion is supported by ESR measurements. If a substantial part of neutral DBs ( $D^0$ ) recharged into non-paramagnetic  $D^-$ , then ESR measurements would detect a significant decrease in spin density as soon as the sample is illuminated, which is not observed [62, 63]. It is therefore justified to ignore the contribution of the  $D^-$  to the total occupation function of the DBs. We will come back to the role of the  $D^-$  as recombination centers in the discussion. The change in occupancy during light soaking and annealing plays a crucial role in this investigation, for example in the measurements of the absorption coefficient by the constant photocurrent method (CPM).

### 2.2.2. The constant photocurrent method (CPM)

Optical absorption ( $\alpha$ ) measurements can give us access to the DOS, provided that the measuring technique is sufficiently sensitive to detect the small signals involved. The  $\alpha$  of the deep defects is of the order of  $0.1 - 10 \text{ cm}^{-1}$ , far below the sensitivity of conventional transmission instruments. The method used in this investigation is a version of the constant photocurrent method (CPM) introduced by Vanecek et al. [64]. Currents can easily and with sufficient accuracy be measured with various commercial instruments. The CPM takes advantage of this fact and is at the same time easier to use and to interpret than alternative methods. Here, the basic concepts of the CPM will be described. In Chapter 3, the version used in this work will be introduced, and its equivalence to the standard CPM will be demonstrated.

For the CPM measurement, the sample is illuminated with light of different wavelengths ( $\lambda$ ), while simultaneously the photocurrent through the sample is monitored. By adjusting the light intensity ( $F$ ), the photocurrent is kept constant at a pre-selected value. In this case (Equ. 2.2)  $G$  will be constant for all wavelengths. With the thickness ( $d$ ) of the film,  $G(\lambda)$  can be written as

$$G(\lambda) = F(\lambda) \frac{1 - \exp(-\alpha(\lambda)d)}{d} \approx F(\lambda) \times \left[ \alpha(\lambda) - \frac{1}{2} \alpha^2 d + \dots \right] \quad (2.9)$$

and  $\alpha(\lambda)$  can be calculated. In this regime,  $0.1 < \alpha < 10$ , depending on the sample and degradation state, and  $\alpha d \ll 1$  for the thickness of the samples used for this investigation. With the left hand side being constant, 2.9 can therefore be reduced to

$$\alpha(\lambda)F(\lambda) = \text{const.} \Leftrightarrow \alpha(\lambda) \propto \frac{\text{const.}}{F(\lambda)}. \quad (2.10)$$

In general, the  $1/F(h\nu)$  spectrum is measured with CPM. The resulting absorption spectrum is calibrated with  $\alpha(h\nu)$ , which is determined in the range that is accessible by standard optical measurements. It is of importance that only transitions to the CB from gap states that are occupied with at least one electron result in a photocurrent [65], which means that only the *occupied* states are accessible with CPM for absorption measurements. This statement will become quite relevant in Chapter 5, when an unexpected dependency of  $\sigma_{\text{ph}}$  of one of the CPM signals is explained. It should also be noted that the possibility to detect a state by either CPM or ESR cannot classify a defect state as a good recombination center.

There is a linear relationship between  $N_{\text{db}}$  measured with ESR and defect absorption for  $h\nu = 1.25$  eV photons measured with CPM [32]. With the calibration factor gained from this relationship,  $\alpha(1.25\text{eV})$  can be converted into  $N_{\text{db}}$ . Further, once the energy dependent absorption coefficient  $\alpha(E)$  is known, the DOS can be derived using [58, 59, 66]:

$$\alpha(E) = \frac{k}{E} \int_{E_{\text{CB}} - E}^{\infty} fN(\varepsilon)g(\varepsilon + E)d\varepsilon, \quad (2.11)$$

where  $E$  is the energy of the incoming monochromatic light,  $f$  the occupancy function and  $N(\varepsilon)$  the density of states in the bandgap at energy  $\varepsilon$ . For simplicity a single species of states is assumed here. Are there different species present in the gap, then  $\alpha(E)$  is the sum of integrals of each species. The matrix element for transitions between gap and CB states is assumed to be independent of  $E$ . This matrix element contributes to the constant,  $k$ , which is found to be  $4.34 \times 10^{38}$  [58, 59, 66]. Equ. 2.11 expresses that  $\alpha(E)$  is comprised of transitions from occupied states in the gap to the CB within  $E$  of  $E_{\text{CB}}$ . Using the DOS, and after calculating their occupation as described in the previous section, it is now possible with Equ. 2.11 to calculate the absorption spectrum as measured by CPM. The result is displayed in Fig. 2.3. The steep decrease of  $\alpha$  with energy for  $E > 1.4$  eV is referred to as Urbach edge and is dominated by transitions from VB tails to the CB. Consequently, it can be used to determine the slope of the VB tail. The dotted line indicates how the Urbach edge would continue, if there was no contribution of the DBs. For  $1 \text{ eV} < E < 1.4 \text{ eV}$ , the excitations from



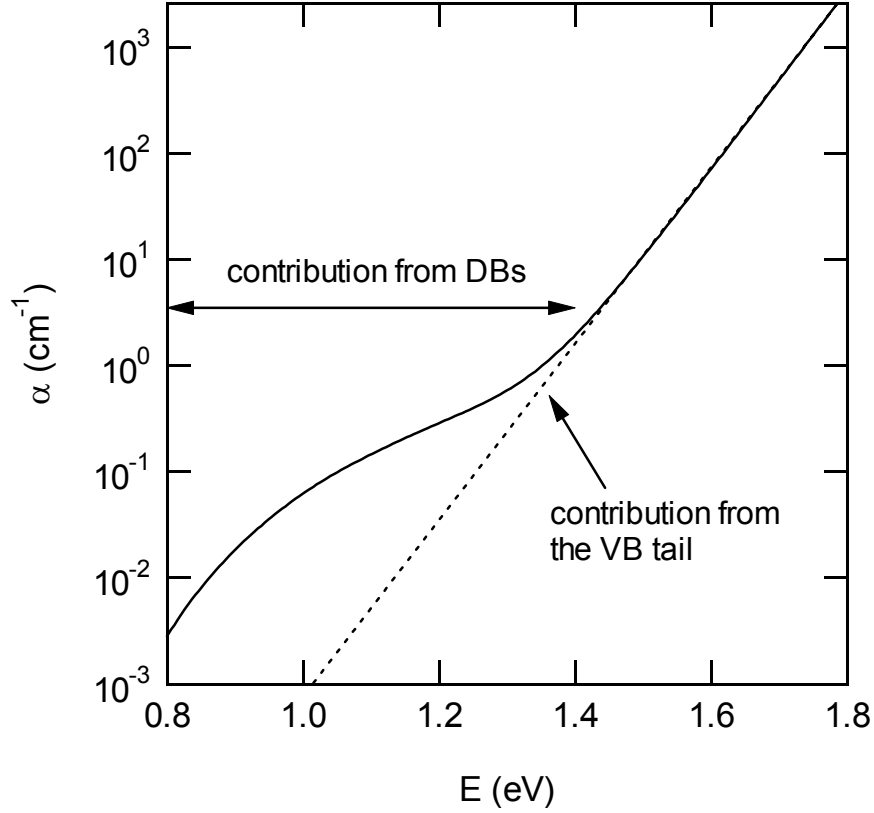


**Figure 2.3:** *Calculated absorption spectrum from a CPM measurement using Equ. 2.11 together with the DOS and the occupation statistics from the previous section. The dotted line is the extension of the Urbach edge, indicating how the absorption would look like without the transitions from the DBs.*

the VB tail become very small and the transitions from DBs dominate the spectrum. For  $E < 1$  eV, the density of occupied DBs drops off together with  $\alpha$ .

### 2.3. Annealing of light-induced defects

A substantial part of the light-degraded  $\sigma_{\text{ph}}$  anneals below 100°C. Surprisingly, this annealing regime is and has been neglected in the investigation of  $\sigma_{\text{ph}}$ . By annealing light-induced defects we gain more information about their nature. The rate equation for annealing applies independently to each kind of defect in Equ. 2.4:

$$\frac{dN_j^{LID}(t_a)}{dt} = -vN_j^m(t_a), \quad (2.12)$$

where  $t_a$  is the annealing time,  $\nu$  the annealing rate and  $m$  the order of the kinetics. For kinetics of order  $m \geq 2$  [67, 68], the annealing of  $N_j^{\text{LID}}$  would strongly depend on its initial value, which is not observed [69, 70]. It is therefore generally accepted that  $m = 1$ . An energetic barrier exists between the metastable (light induced) and the stable (annealed) state of the sample. Information about the annealing activation energy ( $E_a$ ), which is a measure for this separating energy, is contained in the rate constant  $\nu$ . The annealing rate can be written as

$$\nu = \nu_0 \exp\left(\frac{E_a}{k_B T_a}\right), \quad (2.13)$$

where  $\nu_0$  is a prefactor,  $k_B$  the Boltzmann factor and  $T_a$  the anneal temperature. For a unique type of defect with a single value of  $E_a$ , the solution of Equ. 2.12 is an exponentially decaying function  $N_j^{\text{LID}}(t_a) = N_j^{\text{LID}}(0)\exp(\nu t_a)$ , with a well defined life time ( $1/\nu$ ) for the annealing defects. However,  $N_j^{\text{LID}}(t_a)$  does not decay in a simple exponential manner. To fit the data, a lifetime distribution is needed, which translates into an  $E_a$  distribution  $P(E_a)$ . This is a reasonable result considering the disorder in this material and the possible complex microscopic mechanisms involved in the annealing of defects. For completeness, another effect must be mentioned: the Meyer-Neldel rule [71]. It states that  $\nu_0$  in Equ. 2.13 is not independent of  $E_a$  [72], instead

$$\nu_0 = \nu_{00} \exp\left(\frac{E_a}{E_{MN}}\right), \quad (2.14)$$

with the two Meyer-Neldel parameters  $\nu_{00}$  and  $E_{MN}$ . This relationship is observed and must be accounted for in the experimental results of Chapter 4, but otherwise has no effect on the subject of the SWE.

The distribution  $P(E_a)$  is derived from isothermal experiments in the following way [73]: The probability of finding a subset of  $N_j^{\text{LID}}(0)$  with a given  $E_a$  is  $N_j^{\text{LID}}(0) \times P(E_a)$ . With the assumption that such a subset has annealed out after about  $1/\nu$ , where  $\nu$  is given by Equ. 2.13, all defects with

$$E_a \leq E_d = k_B T_a \ln(v_0 t_a) \quad (2.15)$$

will have annealed out. Here,  $E_d$  represents a demarcation energy growing logarithmically with  $t_a$  at a given anneal temperature  $T_a$ . The total number of defects remaining after  $t_a$  is then

$$N_j(t_a) \approx \int_{E_d}^{\infty} N_j(0) P(E_a) dE_a \quad (2.16)$$

and differentiating Equ. 2.16 with respect to  $E_d$

$$\frac{dN_j}{dE_d} = -N_j(0) P(E_a) \quad (2.17)$$

yields  $P(E_a)$ . Applying this procedure to the annealing of  $D^0$ s yields  $v_0 = 10^{10} \text{ s}^{-1}$  and a maximum of their  $E_a$  distribution at about 1.1 eV [8, 36]. In Chapter 4, the same procedure is applied to the anneal data below 100°C, illuminating the role of  $D^0$ s on  $\sigma_{\text{ph}}$  in this regime. In the discussion section this approach is extended to exposure data at the different temperatures of Chapter 4. This leads to the conclusion that thermal annealing is an ongoing process during light-induced degradation at temperatures as low as 150K.

### 3. Experimental Details

#### 3.1. Samples

The samples used for this study are undoped a-Si:H films deposited by plasma enhanced chemical vapor deposition (PECVD) under standard conditions, and by hot wire chemical vapor deposition (HWCVD). The samples were made at the Electrotechnical Laboratory (ETL) in Tsukuba (Japan), the University of Chicago, Penn State University and the National Renewable Energy Laboratory (NREL). The Penn State sample is deposited from diluted silane: H<sub>2</sub> gas is mixed into the SiH<sub>4</sub> gas at a flow ratio of 10:1. A selection of these high-quality samples of various types are chosen for this investigation and listed in table 3.2, together with some of their characteristic parameters.

The thicknesses ( $d$ ) and optical absorption ( $\alpha$ ) at 650 nm of the films are determined by a commercial instrument (n&k analyzer, Photonic Instruments), which uses a fitting routine with the reflectance data of the samples as input. The energy differences between the dark Fermi energy and the conduction band (CB) ( $E_{CB}-E_F$ ) are calculated from the dark conductivity ( $\sigma_d$ ) using  $\sigma_d = \sigma_0 \times \exp(-E_F/kT)$ , with  $\sigma_0 = 150 \Omega^{-1}cm^{-1}$  [55]. The neutral dangling bond ( $D^0$ ) densities ( $N_{db}$ ) are measured by optical absorption ( $\alpha_{hv}$ ) measurements,

sample	deposition laboratory	deposition technique	$T_{sub}$ (°C)	$d$ ( $\mu m$ )	$\sigma_d$ ( $\Omega^{-1}cm^{-1}$ ) annealed, 300K	$E_{CB}-E_F$ (eV)	$N_{db}$ ( $cm^{-3}$ ) annealed
A	ETL	PECVD	250	1.2	$3.6 \times 10^{-11}$	0.75	$2.3 \times 10^{15}$
B	ETL	PECVD	250	1.2	$1.2 \times 10^{-11}$	0.78	$4.0 \times 10^{15}$
C	NREL	PECVD	230	0.69	$1.8 \times 10^{-10}$	0.71	$6.3 \times 10^{15}$
D	U. of Chicago	PECVD	230	1.1	$9.6 \times 10^{-11}$	0.74	$1.0 \times 10^{16}$
E	NREL	HW CVD	340	0.73	$1.3 \times 10^{-10}$	0.72	$7.7 \times 10^{15}$
F	Penn State University	PECVD diluted 1:10	200	1.1	$8.3 \times 10^{-12}$	0.78	$3.0 \times 10^{15}$

**Table 3.1:** Characteristics of the samples that are used for this investigation.  $N_{db}$  is calculated from  $\alpha$  at 1.25 eV with a proportionality constant of  $7.0 \times 10^{15} cm^{-2}$ .

where  $h\nu$  specifies the energy in eV at which  $\alpha$  is measured with the dual wavelength constant photocurrent method (DWCPM) described later in this chapter. Combined electron spin resonance (ESR) and CPM measurements show a linear relationship between  $\alpha_{1.25}$  and  $N_{\text{db}}$ , with a proportionality constant between the two of about  $2 - 8 \times 10^{15} \text{ cm}^{-2}$  [32]. For the calculation of  $N_{\text{db}}$  in table 3.1 a proportionality constant of  $7.0 \times 10^{15} \text{ cm}^{-2}$  was used [32]. For sample D only  $\alpha_{1.3}$  is available, which gives generally about 20% higher values than  $\alpha_{1.25}$ . Therefore, a 20% smaller proportionality constant is used to calculate  $N_{\text{db}}$  from  $\alpha_{1.3}$  for this sample. For the present investigation, the absolute values of  $N_{\text{db}}$  are of little concern, while the relative changes in the measured quantities are relevant. The main results do not depend on the choice of the proportionality constant between ESR and  $\alpha_{1.25}$ . The contacts are thermally evaporated coplanar chromium pads separated by 0.5 mm. On a sample of Marburg University magnesium as well as chromium contacts were deposited, with no measurable difference in the results.

### 3.2. Set-up

For good reproducibility of the data, the samples are annealed, degraded and measured in-situ: once a sample is mounted, it is not moved between experiments. A cartridge heater enclosed in the sample holder is used for the in-situ annealing. The sample temperature ( $T$ ) is measured with a thermocouple pressed on a piece of 7059 Corning substrate within 1 cm of the sample. The samples are first pre-annealed for several hours at  $190^\circ\text{C}$ . Then, prior to each subsequent exposure, the sample is re-annealed at  $190^\circ\text{C}$  for 20 - 30 minutes (referred to as state A) slowly cool ( $\Delta T/\Delta t > 10^\circ\text{C}/\text{min}$ ) to room temperature for the experiments.  $\text{N}_2$  gas flows through the sample compartment to provide cooling and avoid oxidation. The sample is degraded by illumination with a red laser diode of  $\lambda = 653 \pm 2 \text{ nm}$  (1.90 eV) at an intensity of 200 or 300  $\text{mW}/\text{cm}^2$ . For sample A and B  $\alpha_{1.9} = 1.2 \times 10^4 \text{ cm}^{-1}$ , which is a typical value for the investigated samples. A rather homogenous spacial degradation was demonstrated under these conditions [74]. Fig. 3.1. shows a schematic of the set-up.

To obtain the deep defect densities, we use their  $\alpha$ , measured with a corresponding version of the CPM [64]; the validity of this approach will be demonstrated in Section 3.3. Normally a monochromator is used as light source for CPM measurements, because it provides continuously tunable monochromatic light, so that a continuous  $\alpha$  versus  $h\nu$  spectrum can be measured. In the present investigation, the spectra are recorded, for

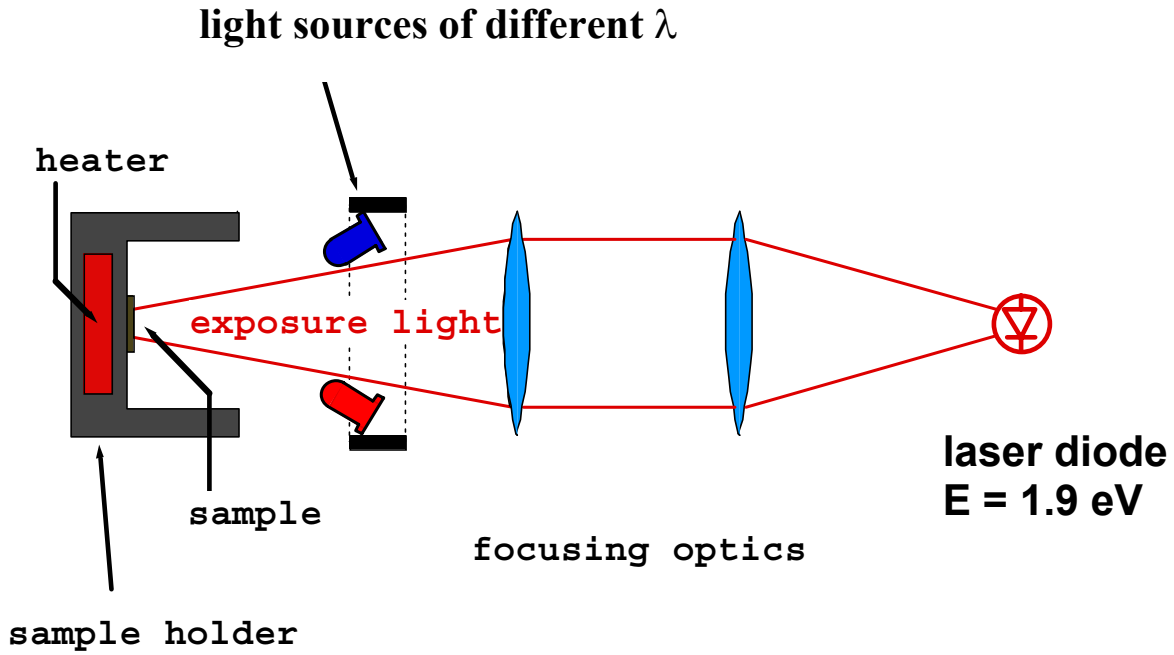


**Figure 3.1:** Schematic of the set-up. From left: sample holder with integrated heater for annealing, ring of light sources for optical absorption measurement, focusing optics, and red diode laser for degradation.

simplicity and quickness, for just seven  $\alpha$ s at seven photon energies. The required monochromatic light of different wavelength is provided by five LEDs ranging from  $\lambda = 590$  to 940 nm and by the filtered light of two incandescent lamps. One filter is a bandpass filter at 990 nm (1.25 eV), the other a cut-off filter passing  $\lambda \geq 1100$  nm ( $h\nu \leq 1.1$  eV). The 1.25 eV light excites electrons from all  $D^0$ s, which is the reason why  $\alpha_{1.25}$  can be calibrated with ESR to yield  $N_{db}$ , as described above. In comparison, the  $h\nu \leq 1.1$  eV light source only excites electrons from deep defect states within 1.1 eV from the CB. If the CPM measurement was done with a monochromatic 1.1 eV light source, then the result could easily be understood as  $\alpha_{1.1}$  (Equ. 2.11). However, the photocurrent at this energy is so small that it is difficult to measure. Therefore, the cut-off filter is used yielding a higher photocurrent. As a consequence the CPM measurement with this cut-off filter is now an integral of  $\alpha_{h\nu}$  with  $h\nu \leq 1.1$  eV. As an indicator that this measurement is an integrated  $\alpha$ , the symbol  $\tilde{\alpha}_{1.1}$  will be used for it. The light sources are mounted on a ring close to the sample with the optical axis at its center, and are operated at 90% of their specified nominal voltage to slow the intensity loss due to aging. The light intensity at each wavelength is measured through a small, defined aperture of  $6.6 \times 10^{-3}$  cm<sup>2</sup> area. The measurement is made with a Newport crystalline silicon

photodiode that is calibrated against a standard from the U.S. National Institute of Standards and Technology. All components can be remotely controlled, which allows us to automate the annealing, exposure and conductivity measurements. The main purpose of the automation is to have an identical measurement protocol every time the master program calls the CPM routine. This improves the reproducibility and accuracy of the measurements. The inverse mobility lifetime product  $((\mu\tau)^{-1})$  (see Section 3.4.) and  $\alpha$  in the energy regime of the deep defects are the main parameters used to characterize the degradation state of the samples.

### **3.3. Dual wavelength constant photocurrent method (DWCPM)**

In the standard CPM technique,  $\sigma_{ph}(\lambda)$  is kept constant by adjusting the impinging light intensity  $F(\lambda)$  while the entire  $\lambda$  range is scanned [64] (see Section 2.2.2.). This procedure is designed to ensure a constant carrier life time during the measurement. The measured  $1/F(\lambda)$  spectrum is calibrated by direct transmission-reflection measurement of  $\alpha$  at one (or more) strongly absorbed wavelength,  $\lambda_{ref}$ . Then, at any wavelength

$$\alpha(\lambda) = \alpha(\lambda_{ref}) \frac{F(\lambda_{ref})}{F(\lambda)}, \quad (3.1)$$

CPM provides a measurement of  $\alpha(\lambda)$  across the entire subgap region of interest.

The dual wavelength CPM (DWCPM) technique gives results identical to CPM but can be faster when measurements of  $\alpha(\lambda_i)$  are needed at only a small number of subgap wavelengths  $\lambda_i$ . DWCPM is formally equivalent to CPM, though for convenience,  $\alpha$  at each  $\lambda_i$  may be measured with a different value of  $\sigma_{ph}$ . By first measuring the entire dependence  $\sigma_{ph}(F)$  at  $\lambda_{ref}$ , it becomes possible to compute  $\alpha(\lambda_i)$  simply by measuring only  $\sigma_{ph}(\lambda_i)$  at any arbitrary known value of  $F(\lambda_i)$ . We use  $\lambda_{ref} = 650$  nm in our measurements and  $G(650\text{nm})$  instead of its approximation  $\alpha(650\text{nm}) \times F(650\text{nm})$  in Equ. 3.1 (see Equ. 2.9 in Section 2.2.2.). DWCPM at a given wavelength ( $\lambda_i$ ) is comprised of the following steps:

- 1) Obtain transmission-reflection measurements of  $R(650$  nm) and  $T(650$  nm). Use these to compute  $G(650$  nm).
- 2) Measure  $\sigma(650$  nm) versus  $F(650$  nm) at enough points to permit confident interpolation across the entire regime of interest. Use results of Step 1 to convert to a plot of  $\sigma(650$  nm) versus  $G(650\text{nm})$  as in Fig. 3.2.

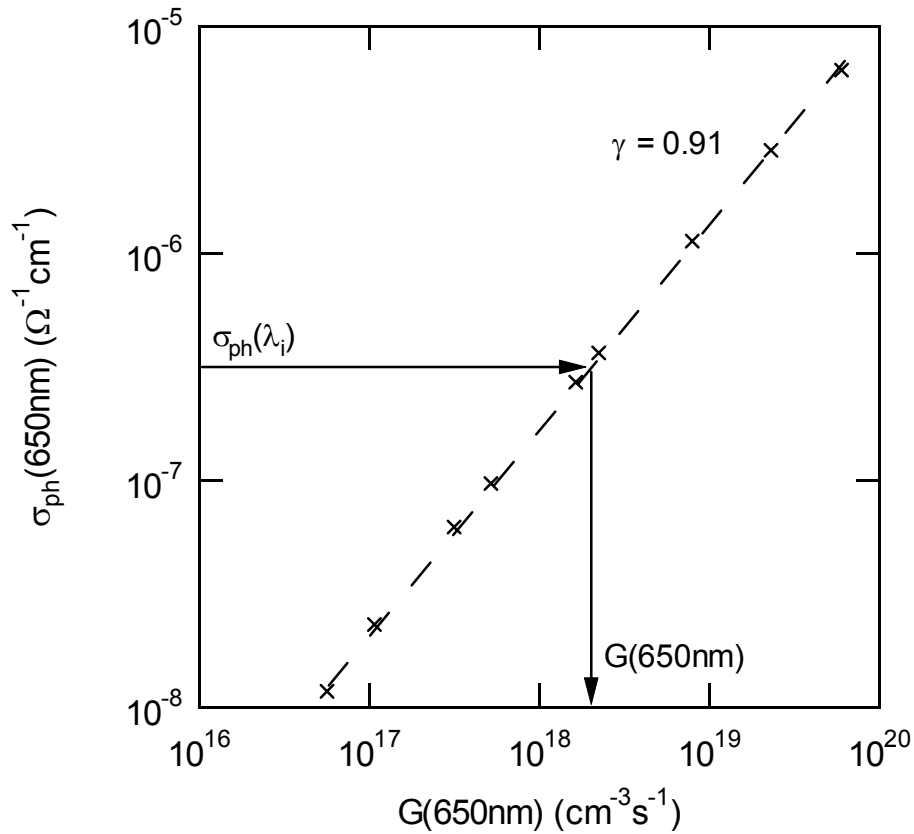


**Figure 3.2:** Generation rate dependence of  $\sigma_{ph}$  for sample B in the annealed state A. The straight line gives a power law dependence of 0.91. The arrows indicate how - for a given value of  $\sigma_{ph}(\lambda_i)$  - the corresponding  $G(650\text{nm})$  is obtained.

- 3) Measure  $\sigma(\lambda_i) = \sigma_i$  at any known intensity  $F(\lambda_i)$ .
- 4) Find the value of  $G(650\text{ nm})$  corresponding to  $\sigma(650\text{ nm}) = \sigma_i$  (using results of Step 2), as indicated by the arrows in Fig. 3.2.
- 5) Use Equ. (3.1) to compute  $\alpha(\lambda_i)$ .

The equivalence of DWCPM and standard CPM is shown in Fig. 3.3. The absorption of sample B and a companion sample at ETL, both in the annealed state, are measured with DWCPM and standard CPM, respectively. There is very good agreement between the two data sets.



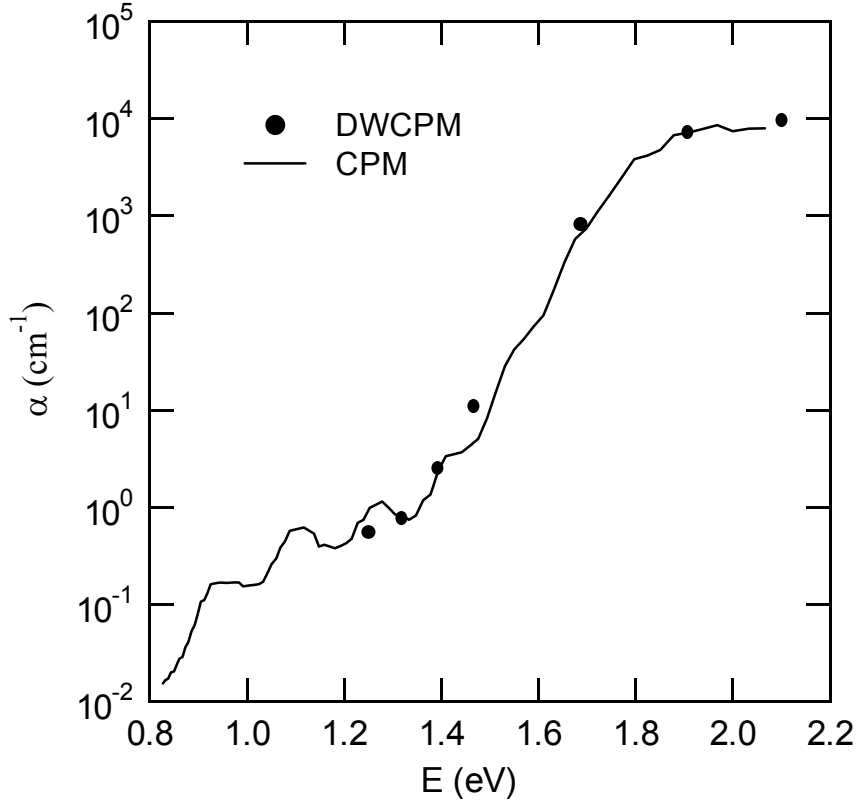


**Figure 3.3 :** Absorption data for sample B in the annealed state, measured with the DWCPM. For comparison the  $1/F(\lambda)$  spectra of a companion sample is shown, measured at ETL with the standard CPM.

### 3.4. The inverse mobility lifetime product $(\mu\tau)^{-1}$

#### 3.4.1. Defects determining photoconductivity

The second part of this thesis concentrates on the still controversially discussed relationship between the neutral dangling bond density  $D^0$  and  $\sigma_{ph}$ . The measurement of  $D^0$  has been the subject of the previous sections. In this section, we introduce a measure for the density of the recombination centers, which determine the lifetime  $\tau$  of free electrons and therefore are responsible for the light- and annealing-induced changes in  $\sigma_{ph}$ . Such a measure has to be derived from  $\sigma_{ph}$  measurements. By combining Equ. 2.2 and 2.3, we can see that the inverse mobility-lifetime product  $(\mu\tau)^{-1}$  serves this purpose:

$$\frac{eG}{\sigma_{ph}} = (\mu\tau)^{-1} = \mu^{-1} \sum_i C_i^{AGD} N_i^{AGD} + \mu^{-1} \sum_j C_j^{LID} N_j^{LID}. \quad (3.2)$$

The far left hand side are quantities that are either constants or accessible to measurements. The invariance of the mobility with light soaking [6, 43-45] permits us to treat  $\mu^{-1}$  as an invariant pre-factor. The exact value of  $\mu$  is sample dependent, but is of minor concern in this study. In the annealed state A all  $N_j^{LID} = 0$  and  $(\mu\tau)^{-1}$  is determined by the sum of the invariant intrinsic defects  $\sum C_i^{AGD} N_i^{AGD}$ . While the sample is light soaked,  $\sum C_j^{LID} N_j^{LID}$  increases. Representing light-induced changes by the symbol  $\Delta$ , we have

$$\Delta \left( \frac{eG}{\sigma_{ph}} \right) = \frac{eG}{\sigma_{ph}} - \frac{eG}{\sigma_{ph}}(annealed) = (\mu\tau)^{-1} - (\mu\tau)^{-1}(annealed) = \mu^{-1} \sum_j C_j^{LID} N_j^{LID}. \quad (3.3)$$

Alternatively, we can normalize quantities to their state A value to obtain

$$\frac{\frac{eG}{\sigma_{ph}}}{\frac{eG}{\sigma_{ph}}(annealed)} = \frac{(\mu\tau)^{-1}}{(\mu\tau)^{-1}(annealed)} = 1 + \frac{\sum_j C_j^{LID} N_j^{LID}}{\sum_i C_i^{AGD} N_i^{AGD}}, \quad (3.4)$$

an expression for the relative increase of the light-induced recombination center density with respect to the intrinsic invariant recombination center density. To ensure that the changes under investigation are not complicated by different quasi-Fermi level splittings, it is best to calculate  $(\mu\tau)^{-1}$  at a fixed level of  $\sigma_{ph}$ . Throughout this investigation  $\sigma_{ph} = 10^{-7} \Omega^{-1} \text{cm}^{-1}$  is used, unless otherwise noted. For all experiments reported,  $\sigma_{ph}$  is at least one order of magnitude higher than the dark conductivity. The next section demonstrates the usefulness of this approach on the SWE.

### 3.4.2. $(\mu\tau)^{-1}$ during light soaking

The increase of recombination centers during light soaking becomes obvious by using  $(\mu\tau)^{-1}$  as a measure for their density. For Fig. 3.4, sample B has been light soaked for over 14 days at  $300 \text{ mW/cm}^2$ .  $\sigma_{ph}$  has been measured at frequent intervals with a generation rate of  $6.0 \times 10^{19} \text{ cm}^{-3} \text{ s}^{-1}$ . The Fig. shows the 'classic' "Staebler-Wronski Effect" [1]:  $\sigma_{ph}$  decreases roughly with exposure time ( $t_{exp}$ ) as  $t_{exp}^{-1/3}$  until about  $10^3$  min, then it appears to slowly approach its saturation value. Because of the unreasonable long times to reach saturation with the present set-up,  $t_{exp}$  remains below 100 min for all experiments. As part of the automated

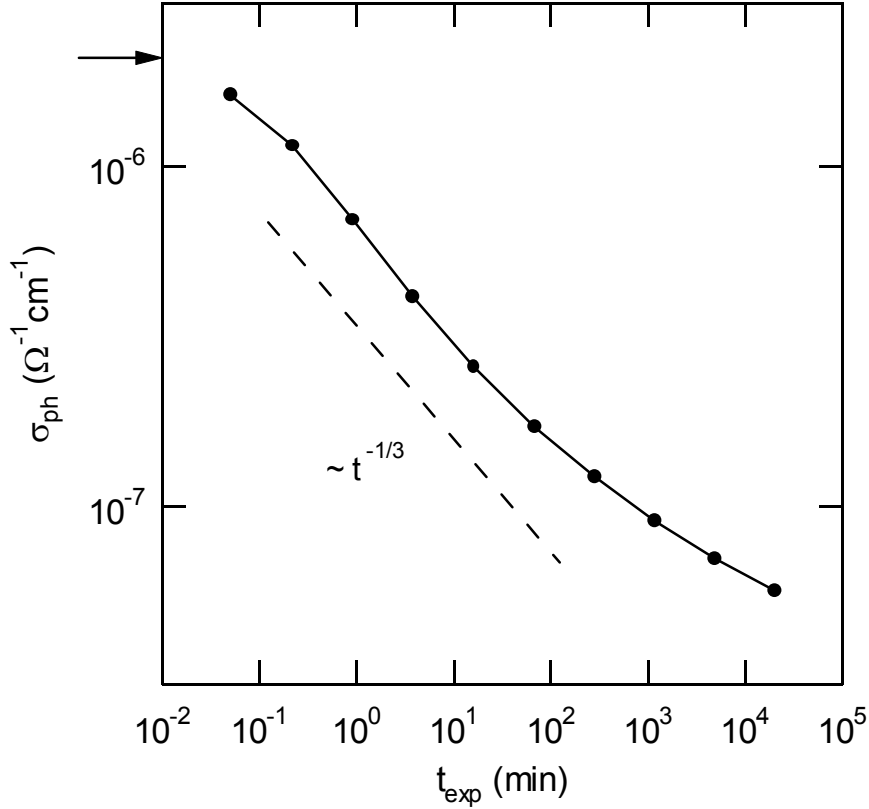


**Figure 3.4:** Degradation of  $\sigma_{ph}$  for an exposure of sample B with  $300 \text{ mW/cm}^2$ . The values are taken from Fig. 3.5 at the highest  $G$ . The arrow indicates the annealed value, and the slope of  $-1/3$  is added for reference.

DWCPM (Fig. 3.2), the dependence of  $\sigma_{ph}$  on  $G$  is measured at each data point of Fig 3.4 and plotted in Fig. 3.5. The top line in this figure is the first measurement taken immediately after annealing. The bottom line is the last measurement at the end of the light-induced degradation. The vertical arrow along the ends of the lines indicates how  $\sigma_{ph}$  measured at a fixed  $G$  decreases with ongoing exposure (Fig. 3.4). The horizontal arrow at  $\sigma_{ph} = 10^{-8} \text{ } \Omega^{-1} \text{ cm}^{-1}$  in Fig. 3.5 illustrates how  $(\mu\tau)^{-1}$  is obtained in the present experiments. For increasing  $t_{exp}$ , the arrow crosses the data lines at increasing  $G$  values. Multiplied with  $e/\sigma_{ph}$ , these yield  $(\mu\tau)^{-1}$ . Fig. 3.6 shows the SWE degradation of  $(\mu\tau)^{-1}$  determined at three different levels of  $\sigma_{ph}$  (indicated in the figure). Each level of  $\sigma_{ph}$  corresponds to a horizontal line cutting through Fig. 3.4. As expected from Equ. 3.3, each  $(\mu\tau)^{-1}$  curve increase with  $t_{exp}$  due to the light-induced creation of recombination centers. For higher  $\sigma_{ph}$  levels, the  $(\mu\tau)^{-1}$

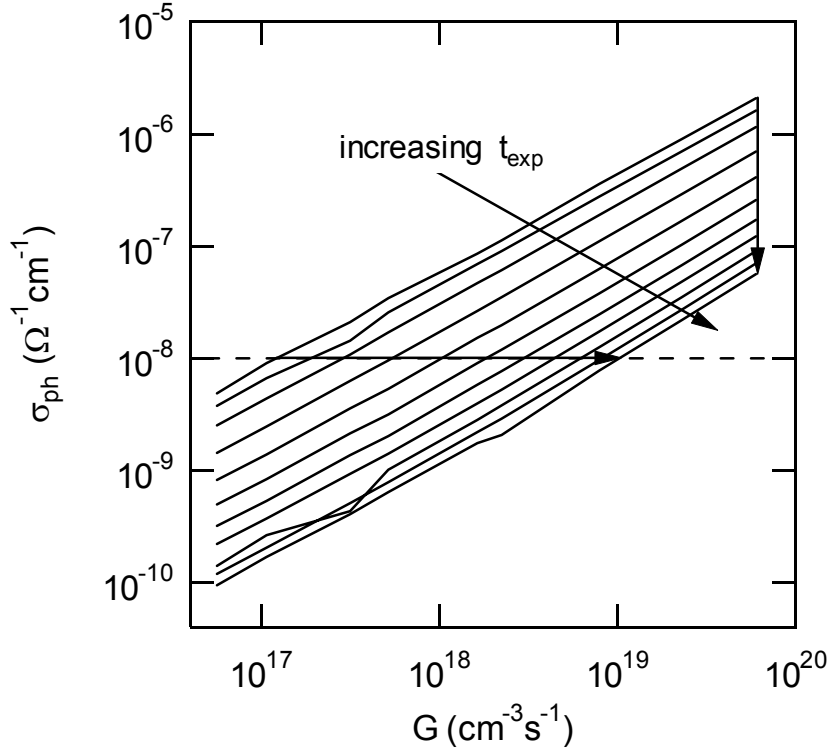


**Figure 3.5:** *Dependence of  $\sigma_{ph}$  on  $G$  during light soaking of sample B for over 14 days at  $300 \text{ mW/cm}^2$ . The uppermost curve was taken in the annealed state of the sample, the bottom curve is the final measurement at the end of light-soaking. The highest value of  $G = 6.0 \times 10^{19} \text{ cm}^{-3}$  corresponds to  $3 \text{ mW/cm}^3$ .*

curves shift to higher values. This is consistent with the picture of an increase in recombination centers due to a wider quasi-Fermi level split (Section 2.2.1). Otherwise, these three curves are very similar. The dotted line is  $(\mu\tau)^{-1}$  at constant  $G = 6.0 \times 10^{19} \text{ cm}^{-3}$ ; this corresponds to the inverse of the data in Fig. 3.5.  $(\mu\tau)^{-1}$  measured at constant  $G$  shows an analogous behavior; however, in comparison to the  $(\mu\tau)^{-1}$  measurements at a fixed  $\sigma_{ph}$  level, it overestimates the density of the recombination centers for small  $t_{exp}$ .

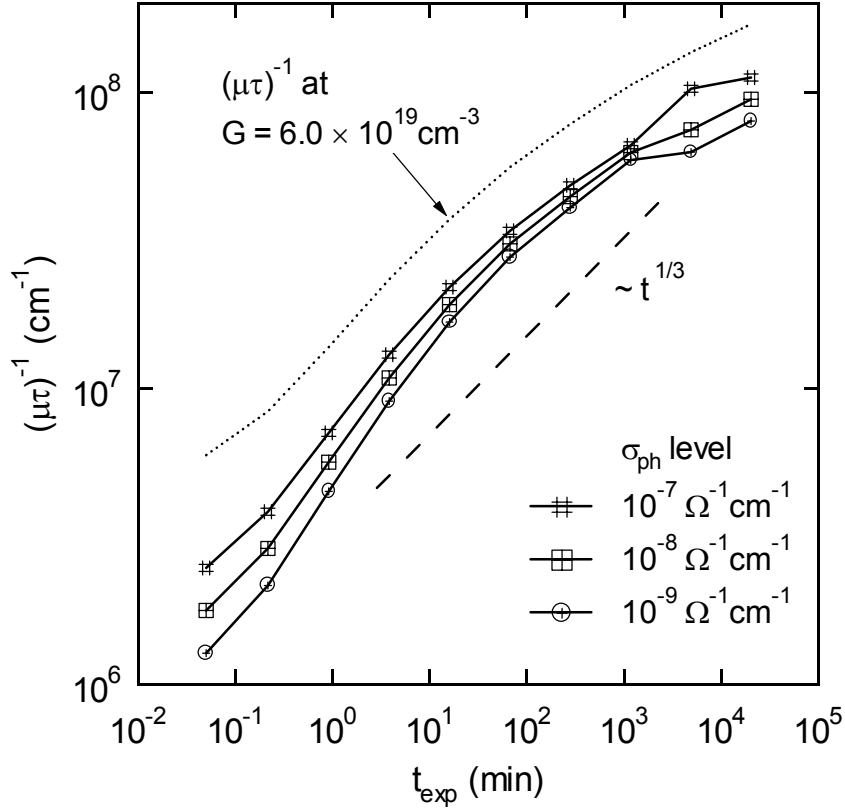


**Figure 3.6:** Light-induced increase of  $(\mu\tau)^{-1}$  with exposure time, measured under different conditions as indicated in the figure and in the text. The slope  $t^{1/3}$  is shown for reference.

### 3.5. Light-soaking and annealing procedures

Probing the defect creation kinetics and testing the relationship of  $\sigma_{ph}$  on defect density in a-Si:H requires changing gradually its density of defects. This is accomplished in this thesis by utilizing the SWE. Electron beam radiation or changing deposition parameters would be other possibilities. Pulsed light-induced degradation is used to find a precursor to degradation that is slower than charged carrier recombination. To explore the different relationships of  $\sigma_{ph}$  on defect density, data of continuous illumination degradation (also at elevated temperature) are compared to step-wise isochronal, and isothermal anneal data.

#### 3.5.1. Pulsed or ‘interrupted’ continuous light-induced degradation

The aim of the experiments described in this section is to compare the degradation of a sample by continuous (CW) light-soaking with the degradation by pulsed illumination of equal peak intensity. This is the central difference from previous laser pulse experiments.

There, the intensities of the pulses are over six orders of magnitude higher compared to CW exposure [27, 75, 76]. The pulsed illumination described in this section can be viewed as an ‘interrupted’ CW exposure.

To create identical conditions during CW and pulsed illumination, it is convenient to use a light source for degradation that can be operated in CW and pulsed mode. We chose a laser diode operated by a current source for light-soaking. The current source is set either to constant current operation, for CW illumination, or externally modulated with a function generator, for pulsed operation. Fig. 3.7 shows the rise of the laser light to full intensity measured by a photodiode (PD). If we define the rise time as the time at which 90 % of the full light intensity is reached, then the rise time for the light intensity is about  $0.5 \mu\text{s}$  (the true rise of the light intensity is probably faster, but the measurement is limited by the speed of the detection circuit). However, because the recombination of free electrons (e) and holes (h)

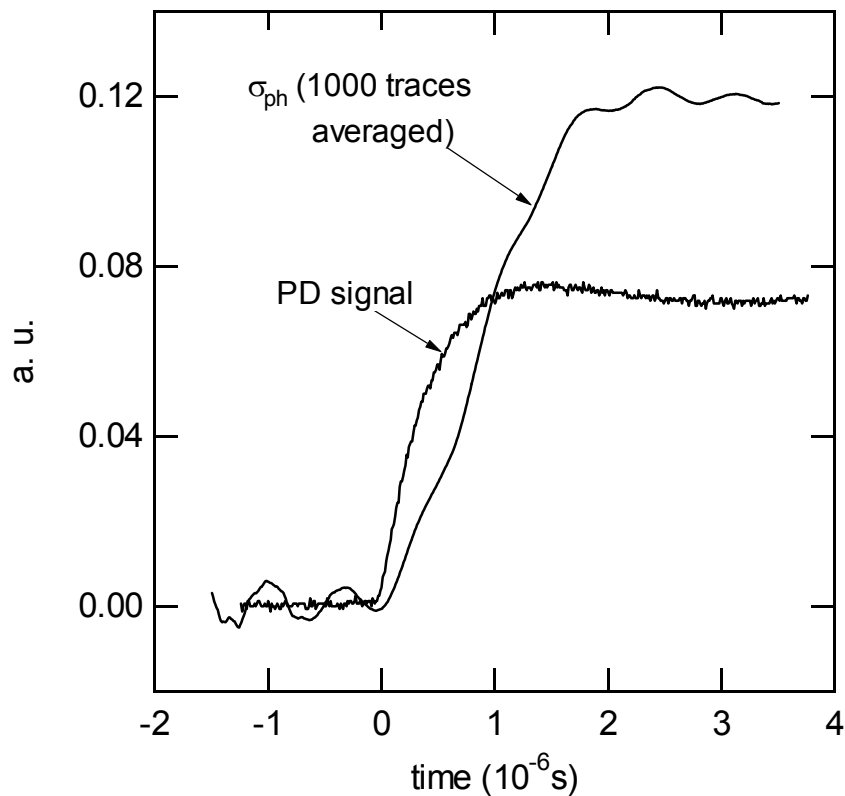


**Figure 3.7:** Rise of a  $300 \text{ mW/cm}^2$  light pulse used for pulsed degradation measured with a photodiode, and  $\sigma_{ph}$ , measured with a fast current-to-voltage amplifier, recorded and averaged with a digital oscilloscope.

drives the degradation in the investigated intrinsic a-Si:H samples [17], the rise time of  $n$  and  $p$  to their steady state value is more important than the rise time of the illuminating light (the purpose of pulsed illumination is really to create rectangular  $n$  and  $p$  pulses). The response of  $\sigma_{ph}$  to a step illumination is used to measure the rise time of  $n$  and  $p$  and is shown in Fig. 3.7. For this measurement, the signal of a fast current to voltage converter is recorded and averaged over 1000 traces in a digital oscilloscope. The rise time of  $\sigma_{ph}$  to 90% of its steady-state value is about 1.5  $\mu\text{s}$ . The decay time of  $\sigma_{ph}$  is not shown, but was also investigated and is also about 1.5  $\mu\text{s}$  (therefore the true rise time of the light is of not critical, as long as it is at least equal or faster than 1.5  $\mu\text{s}$ ). Degradation during the rise and decay time of the electron and hole population can be neglected, when the pulse length ( $t_p$ ) is much longer. The shortest  $t_p$  in this study is therefore chosen as 40  $\mu\text{s}$ . The same restriction applies to the dark intervals ( $t_d$ ) between pulses; for technical reasons  $t_d > 360 \mu\text{s}$  in the present work.

Fig. 3.8 is a sketch of a light pulse train, showing the definitions of  $t_p$  and  $t_d$ , and emphasizing that the intensities used for pulsed and CW exposure are identical. Thus, the pulsed illumination is simply a CW exposure ‘interrupted’ periodically after time  $t_p$  for the duration of  $t_d$ . Disregarding the time for measurements,  $t_{exp}$  is simply the accumulated illumination time. For pulsed illumination,  $t_{exp}$  is defined similarly as  $t_p \times M$ , with  $M$  the total number of pulses. In Chapter 4 changes in the degradation state of the samples between

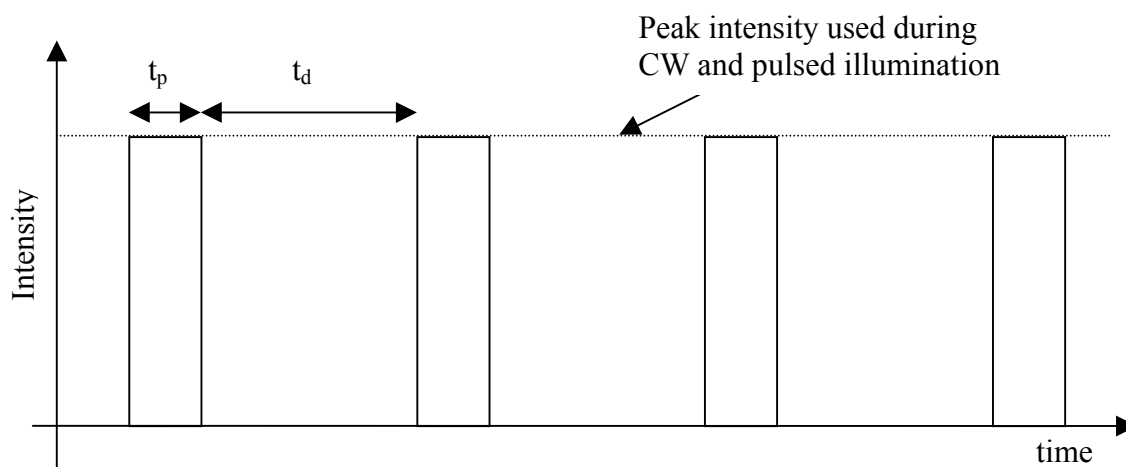


**Figure 3.8:** Schematic of the  $\sigma_{ph}$  pulse train for pulsed illumination. The dashed line indicates the level to which pulsed and CW illuminations are adjusted.

pulses are described. We define the duty cycle ( $\eta$ ) of a pulsed illumination as  $\eta = t_p/(t_p + t_d)$  and the total experimental time ( $t_{\text{tot}}$ ) as the sum of  $t_{\text{exp}}$ , the accumulated dark time ( $t_d \times M$ ), and the time for measurements ( $t_{\text{meas}}$ ):  $t_{\text{tot}} = t_{\text{exp}} + t_d \times M + t_{\text{meas}}$ . We have now the needed tools for the comparison of continuous and pulsed degradation.

### 3.5.2. Measurements at room temperature: Isochronal step-wise annealing

To investigate thermal annealing dynamics, we perform isochronal step-wise anneals of exposed samples. Fig. 3.9 illustrates the procedure. First, right after degradation,  $\sigma$ s and  $\alpha$ s are measured. Then the samples are heated to 50°C, kept there for 30 minutes and cooled slowly ( $\geq 10$  °C/min) down to room temperature, where another measurement is taken. This procedure is repeated for 70°C and continued with steps of 20°C at increasingly higher anneal temperatures up to 190°C. The samples are fully annealed (state A) after the last annealing step at 190°C.

The advantage of this procedure is that all measurements are done at room temperature, which allows for an unambiguous comparison of the data after different pretreatments. However, the investigation of the thermal anneal dynamics with this method is limited by the heating and cooling times.

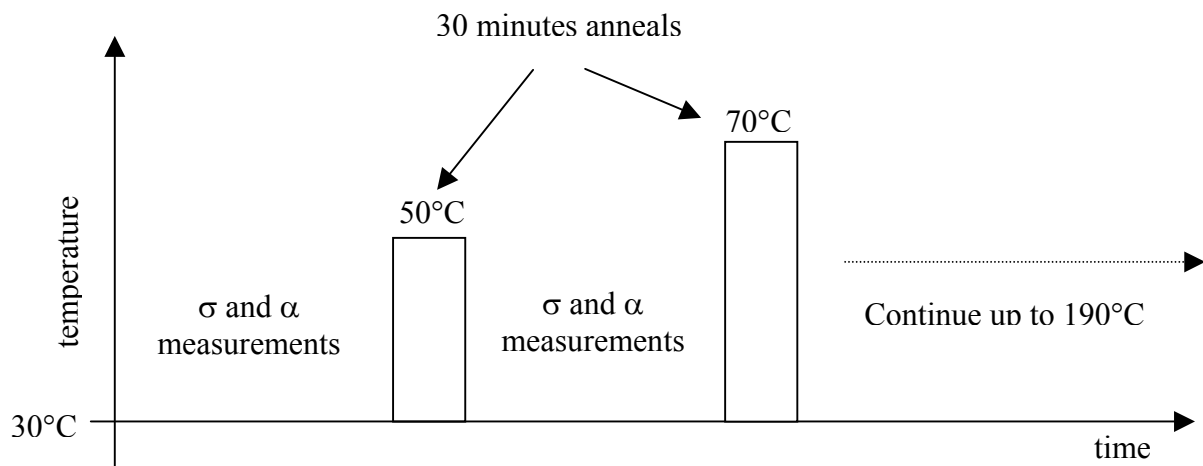


**Figure 3.9:** Schematic of the isochronal step-wise anneal procedure.



### 3.5.3. Measurements at elevated temperatures: Light-induced degradation and isothermal annealing at elevated temperature

Alternatively, annealing dynamics of light-induced defects are also investigated by light soaking and annealing of degraded samples at elevated temperatures. The next two paragraphs briefly describe the experimental procedure for these two kinds of experiments. The remainder of the section deals with the temperature dependent effects of the two main parameters investigated in this work,  $(\mu\tau)^{-1}$  and defect optical absorption measured by DWCPM.

The creation of defects and their properties depend on the exposure temperature [29, 32]. The experimental procedure for investigating these is rather simple: The samples are heated up to the exposure temperature ( $T_{\text{exp}}$ ) and then exposed to the light of the red laser diode. The degradation state is monitored at the same temperature by measuring  $(\mu\tau)^{-1}$  and optical defect absorption. Isothermal anneals means that the light-degraded samples are

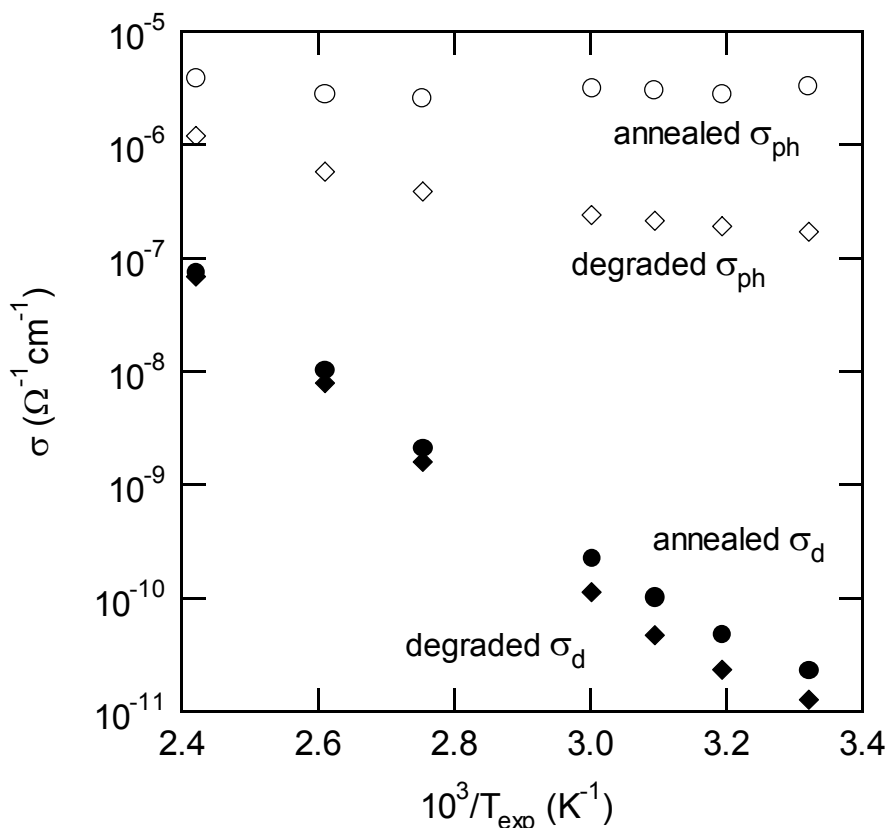


**Figure 3.9:** Photo and dark conductivity of sample B in the annealed state and after 73 min. light soaking at  $300 \text{ mWcm}^{-2}$  versus inverse  $T$ .

heated up to a  $T_a$  and kept there for the duration of the experiment. The degraded sample will anneal with a time constant that depends on  $T_a$  (see 2.3.). The annealing of the samples is monitored by continuously measuring  $(\mu\tau)^{-1}$  and optical absorption by DWCPM. Samples that are exposed at room temperature and then isothermally annealed and samples that are exposed at  $T_a$  show similar annealing behavior [77].

Fig. 3.9 confirms that  $\sigma_{ph}$  is always at least ten times higher than  $\sigma_d$ . It is therefore justified to neglect the contribution of  $\sigma_d$  to the total  $\sigma$ . The dark Fermi level at room temperature for the annealed and degraded sample is 0.78 and 0.79 eV, respectively, and moves for the annealed and degraded state to 0.76 eV at 140°C. This small decrease can be explained by the statistical shift of the dark Fermi level and is within the expected range [55]. This figure shows that light-induced degradation affects  $\sigma_{ph}$  much more than  $\sigma_d$ . While  $\sigma_{ph}$  decreases by about one and a half order of magnitude at room temperature,  $\sigma_d$  decreases by only a factor of about two. At 140°C, the degradation of  $\sigma_{ph}$  is still significant, while  $\sigma_d$

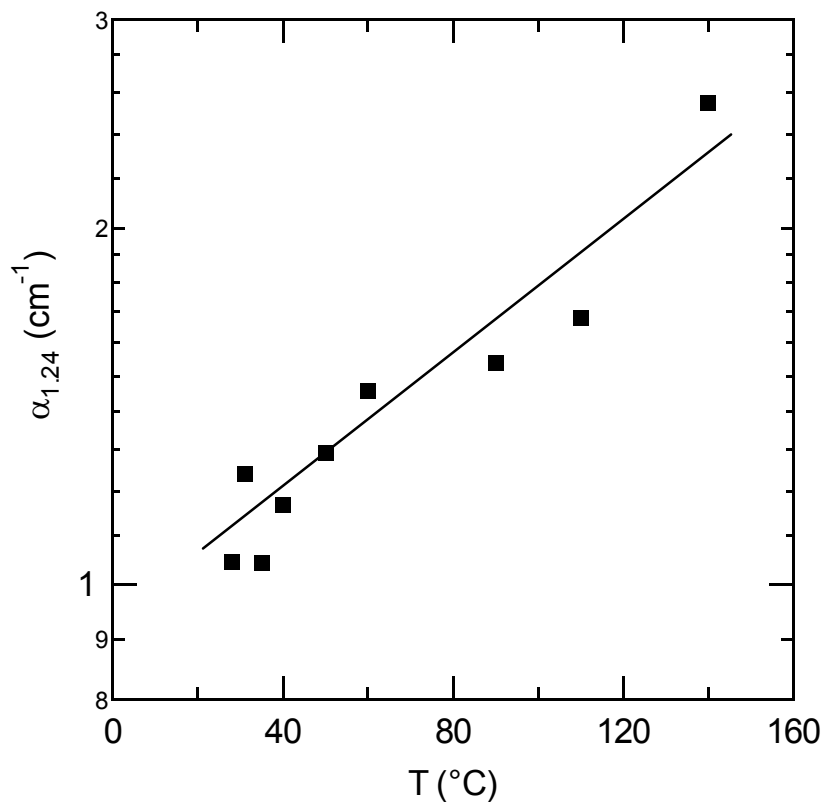


**Figure 3.10:** Absorption coefficient  $\alpha_{1.25}$  of the annealed sample B versus temperature. The line indicates a slope of  $0.024 \text{ cm}^{-1} \text{ K}^{-1}$ .

hardly degrades at all. Overall, there is less degradation at higher temperatures. This finding will be covered in more detail in 4.3.

To investigate the temperature dependence of the optical absorption measurement with DWCPM, sample B was annealed and then heated to various temperatures. Fig. 3.10 shows the increase of  $\alpha_{1.25}$  with temperature by a factor of about two. Because of the shrinking of the bandgap with temperature, such an increase in absorption is expected. For the purpose of this investigation it is possible to take a practical point of view and correct  $\alpha_{1.25}$  measured at elevated temperature according to Fig. 3.10. Similarly, Fig. 3.11 shows the dependence of  $(\mu\tau)^{-1}$  for the annealed sample B on T. At higher T, it can become necessary to determine  $(\mu\tau)^{-1}$  at higher  $\sigma_{ph}$  levels, because otherwise the influence of  $\sigma_d$  cannot be neglected. The decrease of  $(\mu\tau)^{-1}$  with T is due to the smaller quasi Fermi level splitting at higher T for the same free electron density. Thus, there are fewer recombination centers, and  $(\mu\tau)^{-1}$  is lower.

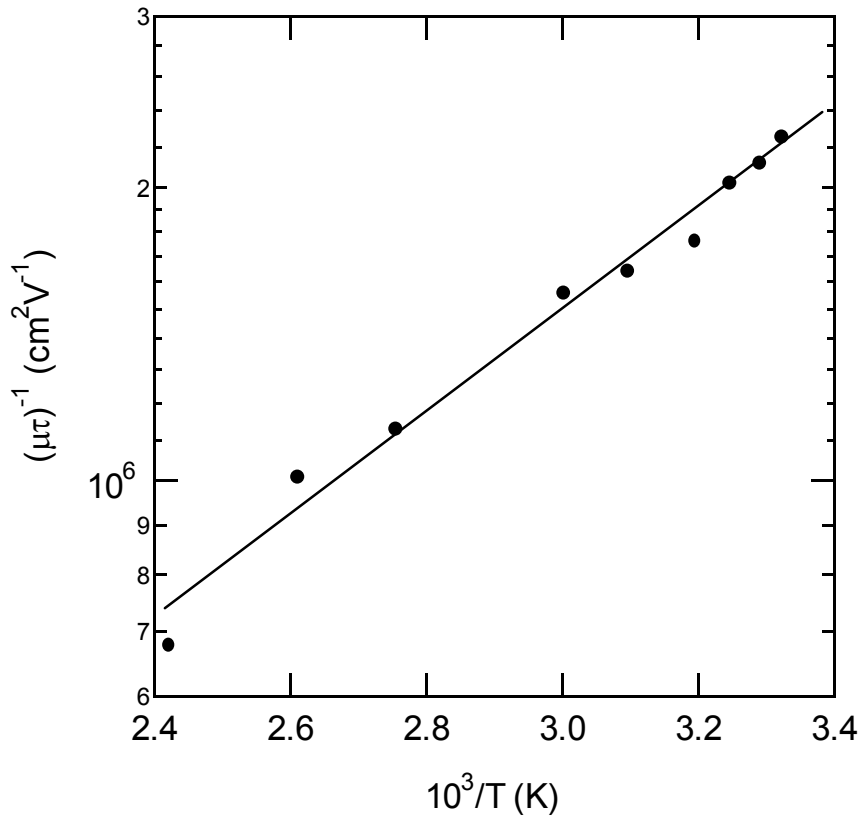


**Figure 3.11:**  $(\mu\tau)^{-1}$  measured for sample B in the annealed state versus inverse temperature. The activation energy is -104 meV.

This section has shown that the temperature dependence of  $\alpha_{1.25}$  and  $(\mu\tau)^{-1}$  has no fundamental new features, which would argue against measurements at elevated temperatures. The knowledge of the temperature dependence is used to correct the data for temperature effects, when data taken at different temperatures are compared. This will be necessary for isothermal annealing  $(\mu\tau)^{-1}$  and absorption data, which is measure at different temperature and will be used to calculate annealing activation energies.

## 4. Creation and annealing of light-induced defects

### 4.1. Pulsed versus continuous degradation

By probing the timescales involved in the Staebler-Wronski Effect (SWE), pulsed illumination exposures are used to explore the creation dynamics of the light-induced defects [28, 75, 78, 79]. It is generally accepted that the recombination of light-generated electrons and holes initiates the Staebler-Wronski Effect (SWE) [17]. The timescales of the creation and recombination of the electrons and holes therefore determines the dynamics of the SWE. If there is a process involved in the SWE that is slower than the electron-hole dynamics, then pulses of appropriate length can be used to detect such a process. This scheme will work if the light pulses are long enough to neglect the light induced increase of the electron and hole density ( $n$  and  $p$ ) to their steady state value, yet short enough that the slower process that is probed does not have enough time to reach steady state. If there is an additional process involved in the SWE, which is slower than the electron hole dynamics, an ‘interrupted’ CW exposure (see Section 3.5.1.) should yield less degradation compared to a ‘standard’ CW degradation experiment. Here, for sufficiently short pulses, this process can never reach the same steady state defect creation rate as during CW illumination (for an extensive discussion see [11]).

#### 4.1.1. Pulsed degradation with constant pulse length

Fig. 4.1 shows typical results for pulsed and continuous (CW) degradation, here demonstrated on sample D. The CW data serves as reference. The CW and pulsed exposures are alternated to ensure reproducibility and to exclude drifts of the experimental setup between measurements. The horizontal axis is the exposure time  $t_{\text{exp}} = M \times t_p$ , as defined in Section 3.5.1. Fig. 4.1a) shows light-induced degradation of  $\sigma_{\text{ph}}$  with pulsed illumination of  $t_p = 40 \mu\text{s}$  and the full period time of  $t_p + t_d = 10 \text{ms}$ , where  $t_d$  is the dark time between pulses. In Fig. 4.1b) the increase of the deep defect density ( $N_{\text{db}}$ ) is measured by monitoring the increase of the deep defect absorption  $\alpha_{1.3}$ . As expected for the scenario with an additional precursor for degradation that is slower than electron-hole recombination, the pulsed illuminated sample clearly shows less degradation than for CW light soaking. This behavior is observed on all good quality samples.

The difference between pulsed and CW light-induced degradation is investigated in more detail in Fig. 4.2 for sample A at fixed  $t_p = 40 \mu\text{s}$  and various  $t_d$ . Intermittently, between

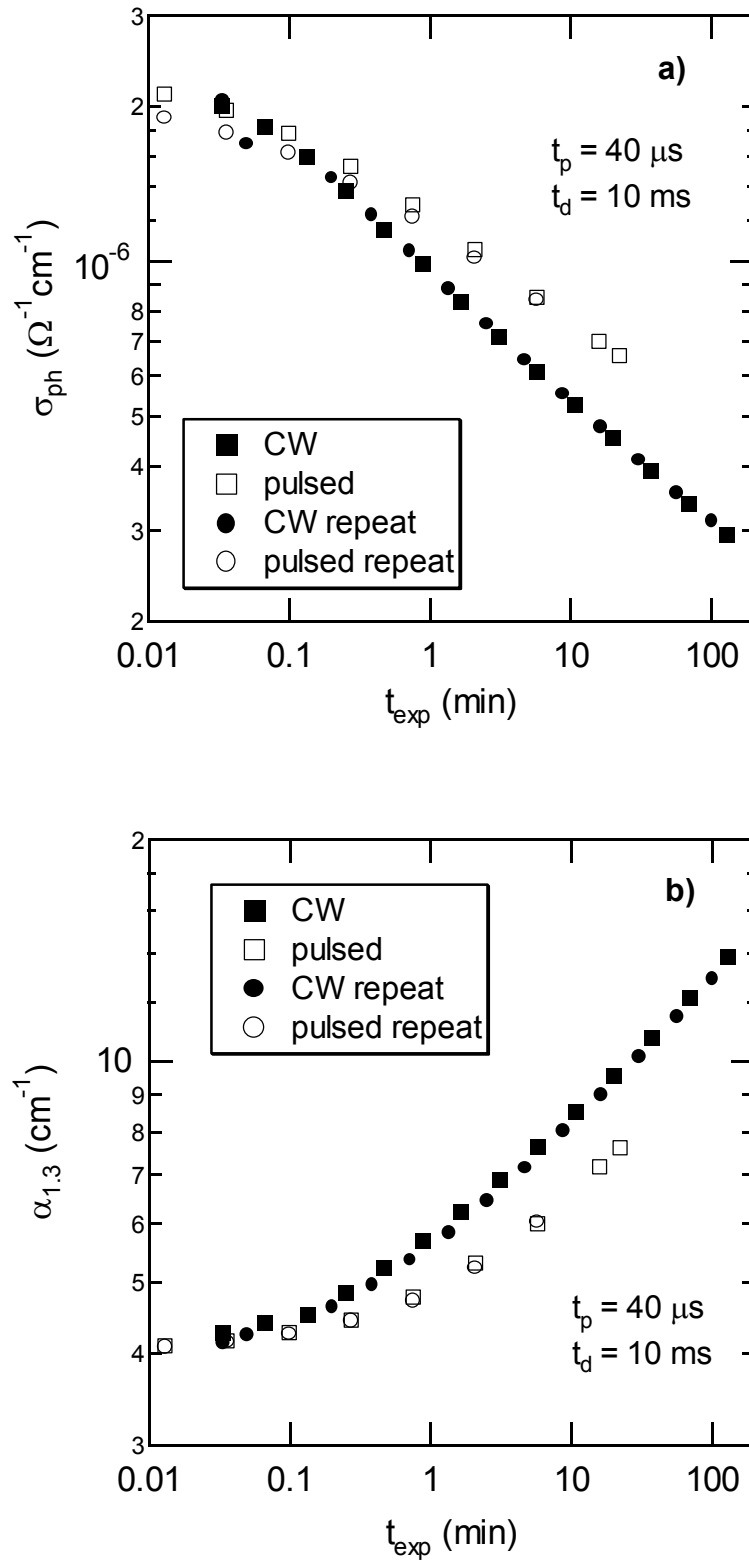


**Figure 4.1:** a) Alternately repeated pulsed and CW  $\sigma_{ph}$  degradation of sample D versus exposure time. b) Increase of  $\alpha_{1,3}$  measured simultaneously with the  $\sigma_{ph}$  degradation of the previous figure.

these pulsed exposures, the sample is degraded with CW light to detect any kind of drift due to the long duration of this experiment. The CW exposures lie on top of each other with high accuracy even after weeks of repeated degradation and anneal experiments, i.e. any kind of drift is so small that it cannot be detected with this set-up. For the pulsed degradations, there is systematically less degradation of  $\sigma_{\text{ph}}$  as  $t_d$  increases. However, considering this small effect of up to about 5 % difference between pulsed and CW degradation, care has to be taken to exclude other possible effects, which could result in a reduced degradation for pulsed illumination. It will be demonstrated in the annealing section of this chapter that part of  $\sigma_{\text{ph}}$  anneals out easily. Especially for long total experimental times ( $t_{\text{tot}} = t_{\text{exp}} + (M \times t_d) + \text{time for measurements}$ ) of up to 15 days (for  $t_p + t_d = 10$  ms in Fig. 4.2), it is conceivable that at least a small part of  $\sigma_{\text{ph}}$  anneals out at room temperature.

The effect of room temperature annealing is investigated by degrading sample A with CW illumination and then monitoring  $\sigma_{\text{ph}}$  while it is left in the dark. Fig. 4.3 shows the CW

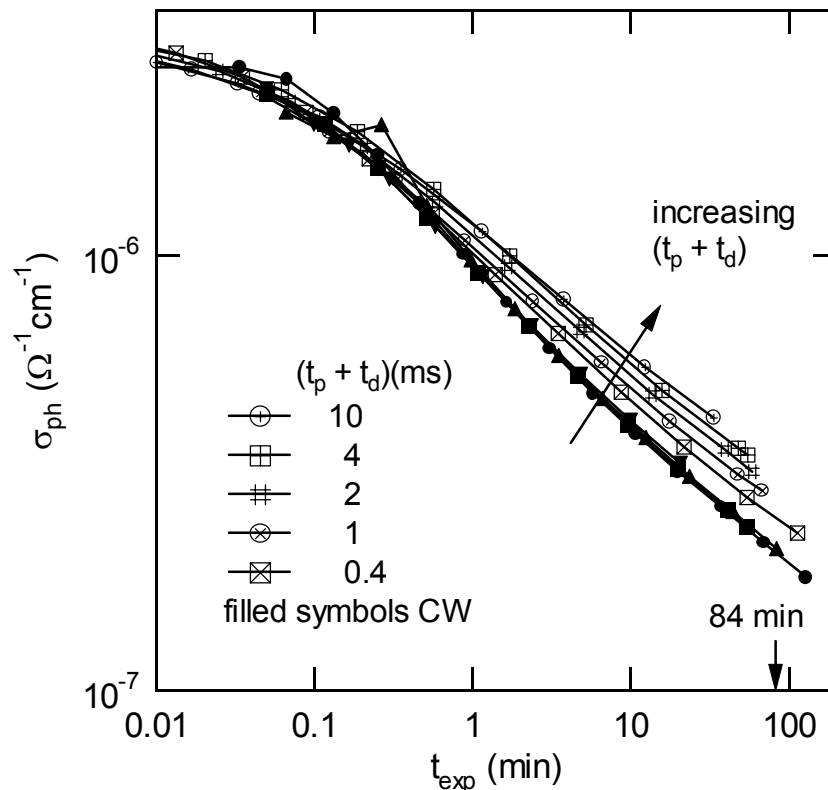


**Figure 4.2:** Pulsed and CW degradation of sample A at fixed  $t_p = 40 \mu\text{s}$  and various  $t_d$ . The arrow on the x-axis indicates  $t_{\text{exp}} = 84$  min, the value to which all the data is either interpolated or extrapolated for the next figure.

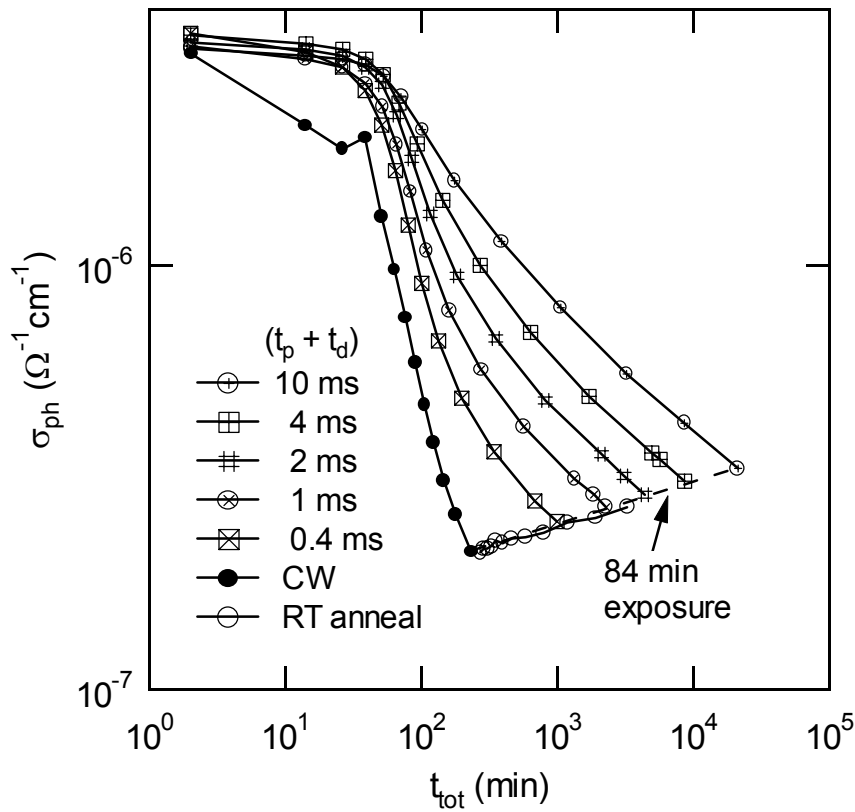


**Figure 4.3:** The same data as in Fig. 4.2, but plotted versus the total experimental time. The last point on each curve is for 84 min total exposure time (extended or interpolated). For clarity, only one CW data set is shown. After the CW measurement, the sample was left to anneal at room temperature (\* points). The dashed line connecting the last points is a guide to the eye.

degradation data as filled circles, and the subsequent room temperature annealing as asterixes. It can be seen that  $\sigma_{\text{ph}}$  recovers by nearly 2 % after about 50 hours in the dark at room temperature. This result leads to the conclusion that at least part of the reduced  $\sigma_{\text{ph}}$  degradation in Fig. 4.3 is due to room temperature annealing. In order to compare the effect of room temperature annealing after the CW and during pulsed degradation, it is best to have the same total experimental times,  $t_{\text{tot}}$ . For this purpose, the curves of the pulsed degradation data of Fig. 4.2 are either interpolated or extrapolated slightly to obtain the final point of each degradation curve in Fig. 4.3. This is an estimated value of  $\sigma_{\text{ph}}$  at  $t_{\text{exp}} = 84$  min, corresponding to the exposure time of the CW exposure in Fig. 4.3. Next,  $t_{\text{tot}}$  is determined by adding to  $t_{\text{exp}}$  both,  $M \times t_{\text{d}}$  and the time for measurements at each data point. The 84 min exposure points can now be seen to lie on a straight line, which corresponds to the RT



annealing of  $\sigma_{\text{ph}}$ . It appears that only the total illumination and dark times determine the state of the sample. No slow precursors can be distinguished on these timescales.

The annealing would be accelerated if the sample temperature would rise significantly during illumination. Before we modified the experimental approach accordingly, we checked for different sample temperatures during CW and pulsed illumination.

#### 4.1.2. The rise of the sample temperature during illumination

The measurement of thin-film temperatures is difficult, therefore various approaches were used. They yielded similar results. The use of a thermocouple in the sample holder of the set-up is acceptable as long as it is ensured that the thin film and the thermocouple are in thermal equilibrium with each other. This is the case during annealing. During illumination, the sample is illuminated locally, and thermal equilibrium between the focal area and the thermocouple is probably not achieved. The thermal probe must be in intimate contact with the film. Alternatively,  $T$  can be measured with intrinsic properties of the film itself.

1. *Resistance change of a Nickel-meander.* A Ni-meander of total dimensions  $2.1 \text{ mm} \times 2.4 \text{ mm}$  pre-deposited on the substrate of an a-Si:H sample has a small thermal mass and is in intimate contact with the film. Its change of resistance with temperature is used to measure the increase of the sample temperature. The change in resistance with  $T$  is calibrated using the thermocouple of the set-up. Then the meander is illuminated with the CW light that is used for degradation. The upper limit of the increase in sample  $T$  ( $\Delta T$ ) under CW illumination was below 2 K.

2. *Temperature dependent change of open circuit voltage ( $V_{\text{oc}}$ ) in a solar cell.* The  $V_{\text{oc}}$  of a solar cell decreases with temperature. A solar cell is mounted instead of the sample, and the change in  $V_{\text{oc}}$  is calibrated against the thermocouple. The upper limit of  $\Delta T$  in this case is determined by the noise of the small change in  $V_{\text{oc}}$ , and was determined to be  $\Delta T < 5 \text{ K}$ .

3. *Change of absorption with temperature.* The increase of absorption with rising  $T$  can be used to measure the change in temperature of the absorbing film. This measurement is done outside the sample holder, because a light sensitive detector must be mounted behind the sample. The light of a Helium-Neon laser ( $\lambda = 648 \text{ nm}$ ) is used as the probe for the change in transmittance, and a crystalline silicon photodiode as detector. The change in transmittance of the film was calibrated in an isothermal oven through which the laser beam passed. After calibration, the sample was mounted on a copper plate, with a small hole through which the laser beam could pass. A halogen lamp of similar intensity as the laser was used for the CW illumination of the sample. The measured  $\Delta T$  is below 5 K and again

determined by the noise of the detector signal. It turns out that the thermal contact with the copper is of importance. If the sample is clamped to a holder only at its corners, then  $\Delta T$  is much higher than if the sample is in thermal contact with the copper plate (as in the set-up).

The  $\Delta T$  for pulsed illumination was not measured, but obviously it can only be smaller than for CW illumination. Therefore, with a negligible increase in  $\Delta T$  during CW illumination, the difference between pulsed and CW illumination can be neglected as well. Overall, the measured  $\Delta T$  are sufficiently small to neglect a possible accelerated annealing of a degraded sample.

Since we have confirmed that an increase in sample T can be excluded as cause for the difference between pulsed and CW illumination, the investigation returns to the pulsed degradation.

#### 4.1.3. Pulsed degradation with constant duty cycle

Room temperature annealing cannot be avoided. Therefore, we degraded the samples such that the room temperature annealing component was always identical. Since only  $t_{\text{tot}}$  and  $t_{\text{exp}}$  determine the degraded state (Fig. 4.3), this can be achieved by comparing the degradation of samples illuminated with pulses of different  $t_d$  and  $t_p$ , but constant duty cycle ( $\eta = t_p/(t_p + t_d)$ ). This is evident with the definition of  $t_{\text{exp}}$  and by rewriting  $\eta$  to  $t_d = t_p \times (\eta^{-1} - 1)$ :

$$t_{\text{tot}} = t_{\text{exp}} + M \times t_p \times \left( \frac{1}{\eta} - 1 \right) = t_{\text{exp}} + t_{\text{exp}} \times \left( \frac{1}{\eta} - 1 \right) = \frac{t_{\text{exp}}}{\eta}, \quad (4.1)$$

with  $t_{\text{tot}}$  and  $t_{\text{exp}}$  independent of  $t_p$  or  $t_d$  as long as  $\eta$  is constant. The experimental time is disregarded in this equation, because its contribution is always the same, i.e. independent of  $\eta$  anyway.

Fig. 4.4 shows degradation curves of sample A for a CW and several  $\eta = 0.01$  pulsed illuminations for pulses of  $t_p = 40 \mu\text{s}$  to 3 ms. The results for all three pulsed exposures are indistinguishable. The results of several duty cycle experiments must be examined to determine whether pulsed light exposure degrades the sample indeed less than CW illumination. Fig. 4.5 summarizes degradations for different  $\eta$ , including the data of Fig. 4.4. This time the data are plotted versus  $t_{\text{tot}}$ , so that different duty cycles can be compared. The pulsed illuminations show reduced  $\sigma_{\text{ph}}$  degradation for smaller  $\eta$ , which is consistent with the

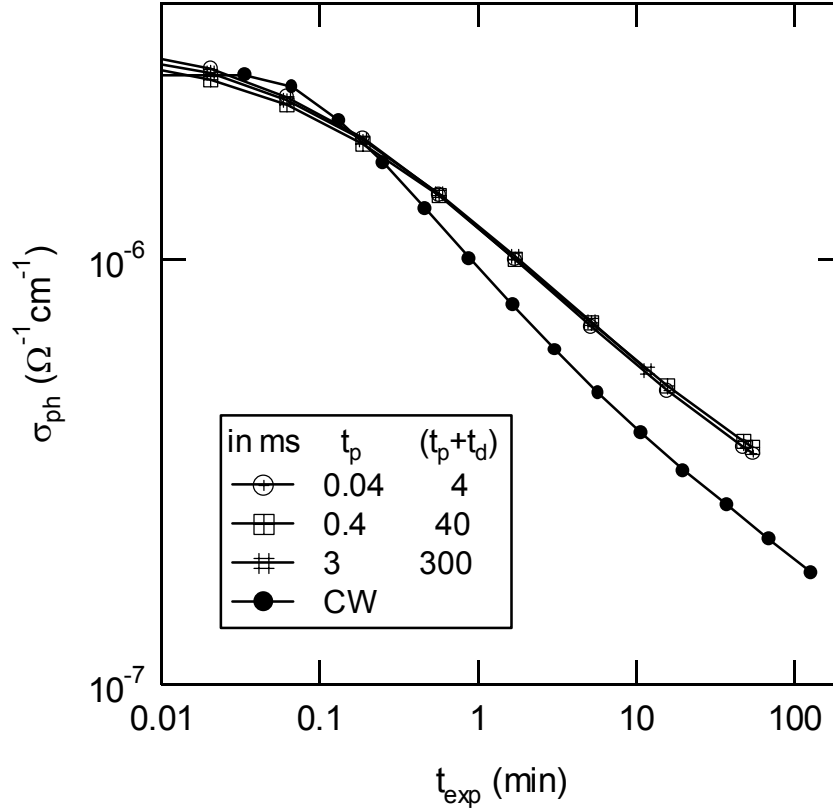


**Figure 4.4:** Pulsed exposure data of constant duty cycle  $\eta = 0.01$  for sample A. The CW exposure is included for reference.

influence of room temperature annealing: Smaller  $\eta$  translates into longer accumulated dark times ( $M \times t_d$ ) for annealing. This graph shows an insensitivity to  $t_p$  and  $t_d$  for each  $\eta$ , which corroborates the assumption that  $\sigma_{ph}$  depends mainly on  $t_{exp}$  and the accumulated dark time and not on  $t_p$  and  $t_d$  themselves. This important null result limits, but does not exclude, any slow precursor process involved in light-induced defect creation. The upper limit for a slower process is determined by the shortest  $t_p$  or  $t_d$  used during degradation with different  $\eta$ , which is 40  $\mu$ s.

#### 4.1.4. Consequences and concluding remarks on pulsed degradation of a-Si:H

The results of the previous section add important information to pulsed degradation results in a-Si:H. Laser pulsed illumination has been used to accelerate [25, 80, 81] and investigate the SWE dynamics [75, 78, 79]. The laser pulsed degradation of undoped a-Si:H has a higher efficiency per absorbed photon than during CW illumination [78]. This result

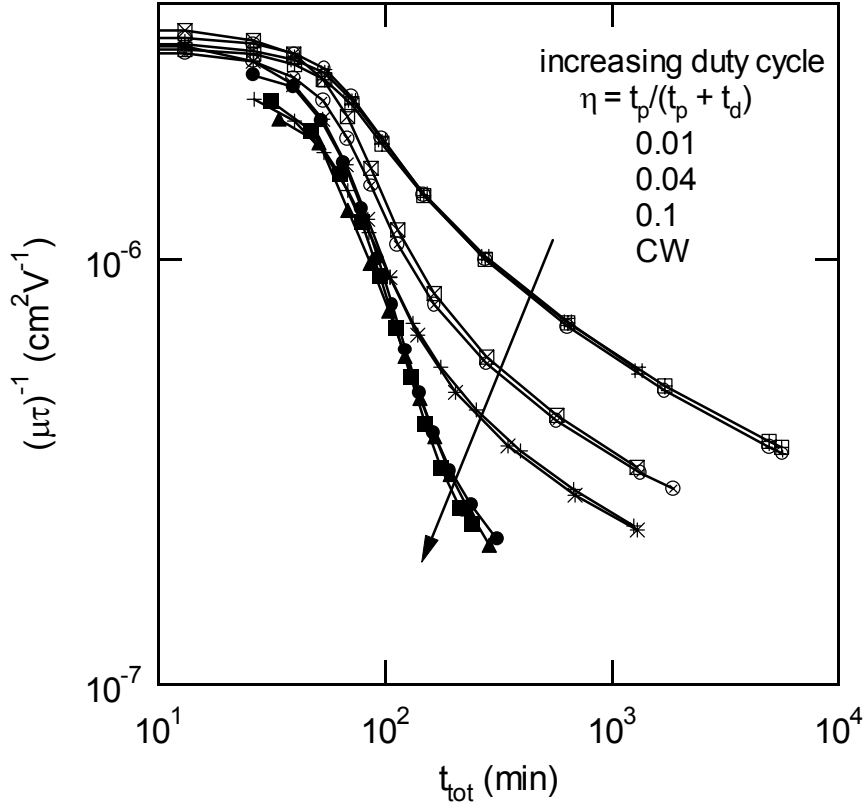


**Figure 4.5:** Pulsed exposure data of constant  $\eta = 0.01, 0.04, \text{ and } 0.1$  versus total exposure time. CW exposures are included for reference.

was explained by the assumption that the degradation of the a-Si:H sample continues between laser pulses, because the electron population has a slower decay time than the light pulse [75]. That means that after each pulse, a relatively slow decaying electron-hole population must exist, which acts as a precursor to degradation. However, fast  $\sigma_{\text{ph}}$  measurements show that  $\sigma_{\text{ph}}$  decays as fast as the light pulse [76]. It remained an open question if the degradation process contains a component significantly slower than the recombination of electron holes. Branz analyzed extensively how a slow precursor would have to rise and decay during and after a light pulses. He concluded that such a precursor can indeed explain the results of the laser pulsed degradation experiments [78] and suggested mobile hydrogen as the precursor to degradation [11]. However, there are other possibilities of a slow precursor. A wide range of these can be summarized as structural changes connected to the SWE [20, 21], such as volume expansion [24, 82] medium and long range order [83, 84].

The results of the previous section show that for moderate light intensities the degradation follows the light pulse, which means that a slow precursor must rise with a time constant of at least 40  $\mu\text{s}$ . Experiments with light pulses of shorter  $t_p$  and sufficient

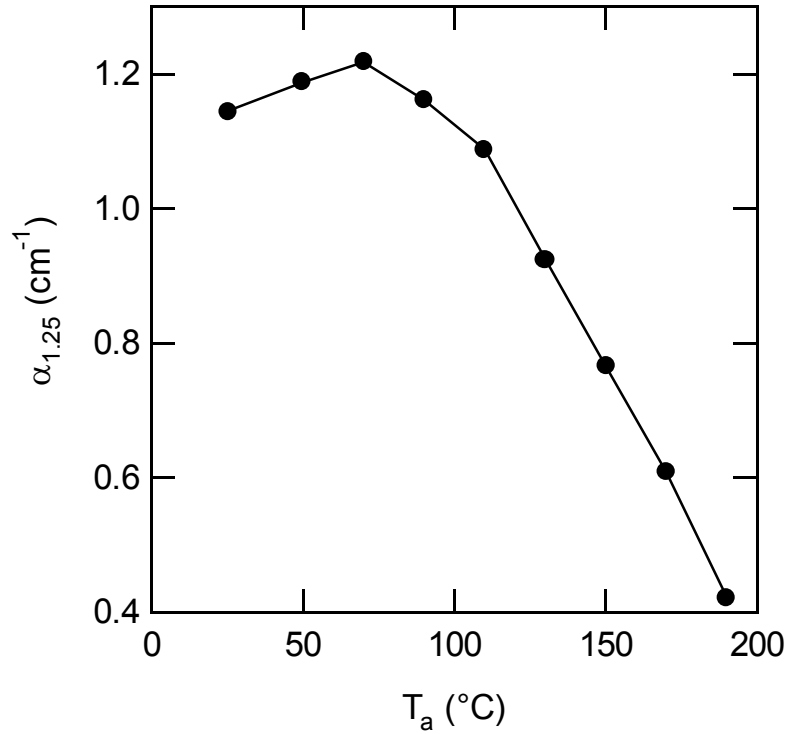
rectangular shape would have been possible technically, but of no use. The critical parameter, in an experiment like this, is the rise time of the recombining n and p, which is about 1.5  $\mu\text{s}$  at the used light intensities (Section 3.5.1.). For any pulse length shorter than 40  $\mu\text{s}$ , it will be difficult to distinguish the rise and decay of n and p from a slow precursor. Detailed studies using paired laser and flashlight pulses for degradation concluded that a slow precursor must have a time constant in the range of 0.1 - 10  $\mu\text{s}$  [27]. If this is the case, then the slow precursor is just outside the accessible range of the presented pulsed experiments.

## **4.2. Annealing of light induced defects**

Room temperature annealing during pulsed degradation leads to a problem in the understanding of  $\sigma_{\text{ph}}$  in a-Si:H, which is still not solved and subject of considerable speculation. Part of the light-degraded  $\sigma_{\text{ph}}$  recovers easily, and is responsible for the room temperature annealing effect observed in the pulsed degradation experiments. This section will state this problem in a much simpler and clearer way than it is possible with the data of the pulsed experiments. It focuses on the annealing behavior of light induced defects (LID) and examines their properties. In the next two sections, the results of isochronal (see 3.5.2.) and isothermal (see 3.5.3.) anneals of light degraded samples are presented. A typical light-induced degradation of  $\sigma_{\text{ph}}$  and  $(\mu\tau)^{-1}$  versus exposure time was shown in Figs. 3.4 and 3.6 in the previous chapter. From here on  $(\mu\tau)^{-1}$  instead of  $\sigma_{\text{ph}}$  will be used as the quantity that characterizes the state of degradation (see Section 3.4), because this section will focus on the role of LIDs as recombination centers.

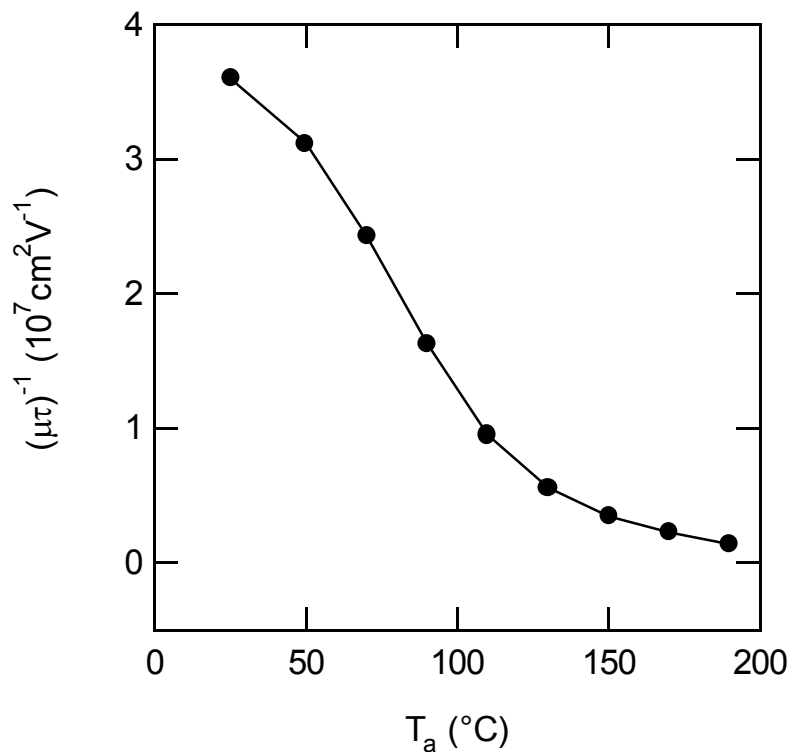
### **4.2.1. Isochronal step-wise annealing**

Fig. 4.6 shows  $\alpha_{1.25}$  versus isochronal (30 min) annealing temperature  $T_a$  (for experimental details, see Section 3.5.2.). The deep defect absorption increases slightly at low  $T_a$ , but drops significantly only above 110°C. This decrease is the annealing of the neutral dangling bond ( $D^0$ ) density ( $N_{\text{db}}$ ). With annealing activation energies ( $E_a$ ) for  $D^0$  of about 1.1 eV, there should indeed occur very little annealing below about 100°C. The annealing behavior of  $(\mu\tau)^{-1}$  is very different, as shown in Fig. 4.7. The density of recombination centers, represented by  $(\mu\tau)^{-1}$ , already decreases significantly during the first annealing step at 50°C. It seems that  $(\mu\tau)^{-1}$  and  $\alpha_{1.25}$  are not well correlated during annealing. In Fig. 4.8  $(\mu\tau)^{-1}$



**Figure 4.6:** Step-wise isochronal annealing of sample A after 73 minutes of light-induced degradation.  $\alpha_{1.25}$  is shown after annealing for 30 minutes each at increasing  $T_a$ .

of Fig. 4.7 is plotted versus  $\alpha_{1.25}$  of Fig. 4.6. Such a plot eliminates the parameter  $T_a$  of Figs 4.6 and 4.7 and allows to include the  $(\mu\tau)^{-1}$  versus  $\alpha_{1.25}$  data for degradation in the same graph. The relationship between  $(\mu\tau)^{-1}$  and  $\alpha_{1.25}$  is obviously linear during degradation. This is a very robust and widely observed relationship [7, 8, 29-31, 37]. The increase in  $D^0$  has therefore been the primary suspect for the cause of  $\sigma_{\text{ph}}$  degradation [6-8], though careful study of the annealing behavior calls this into question. During annealing, the data does not retrace the trajectory  $(\mu\tau)^{-1}$  versus  $\alpha_{1.25}$  taken during degradation. There are two regimes of annealing: First, up to 110°C  $(\mu\tau)^{-1}$  recovers by about 75% with only slight changes in  $\alpha_{1.25}$ . Then, above 110°C, the remaining 25% of  $(\mu\tau)^{-1}$  recovers roughly linearly with  $\alpha_{1.25}$ . Hence,  $(\mu\tau)^{-1}$  is not a single valued function of  $N_{\text{db}}$  [9, 37]. Similar results are observed in all samples investigated. Further, the literature shows no examples of intrinsic good quality samples with trajectories different from the one shown in Fig. 4.8.



**Figure 4.7:**  $(\mu\tau)^{-1}$  versus  $T_a$  for sample A measured at the same time as the data of Fig 4.6.

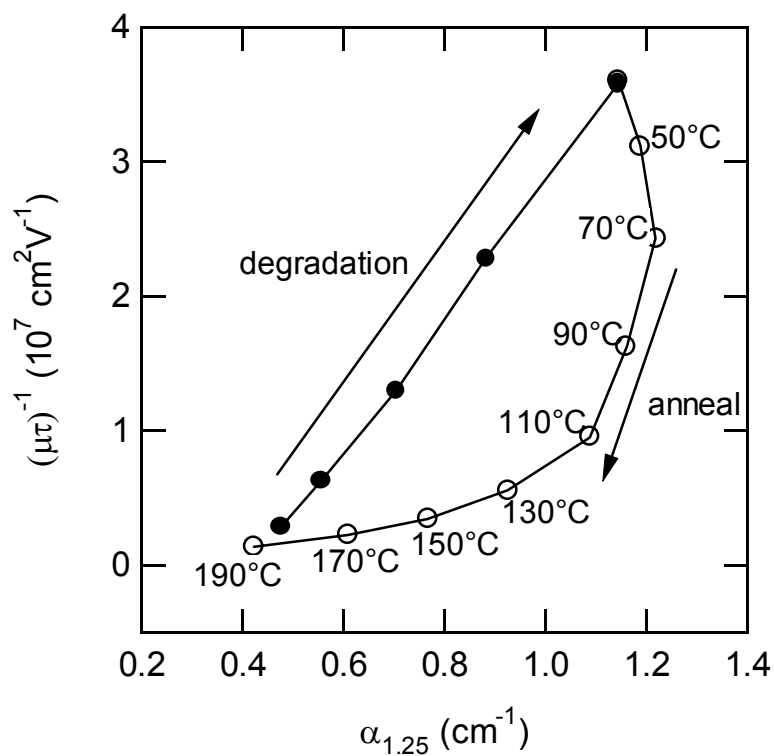


**Figure 4.8:** Combining the data of Figs. 4.6 and 4.7:  $(\mu\tau)^{-1}$  vs.  $\alpha_{1.25}$  for 73 min. degradation (filled circles) and 30 min. isochronal step-wise anneals (open circles) at the indicated  $T_a$ 's.

The integrated absorption  $\tilde{\alpha}_{1.1}$  is used to study deep defects closer to the conduction band (CB) than 1.25 eV. Fig. 4.9 shows  $\tilde{\alpha}_{1.1}$  versus  $\alpha_{1.25}$  for the same experiment as Fig 4.7 - 4.9. Now, the data are normalized to the annealed values before degradation, indicated by  $\alpha_{hv}(0)$ . During isochronal anneals, there is an increase in  $\tilde{\alpha}_{1.1}$  of about 30% with respect to its degraded value. At higher T,  $\tilde{\alpha}_{1.1}$  decreases linearly with  $\alpha_{1.25}$ . Such an increase in  $\alpha_{hv}$  for  $h\nu < 1.25$  eV was previously observed only in degradation and annealing experiments at extremely low temperatures ( $T < 50$  K) [38]. It is interesting to note that the transition between the increase and decrease of  $\tilde{\alpha}_{1.1}$  occurs at the same  $T_a = 110^\circ\text{C}$  at which  $(\mu\tau)^{-1}$  changes from the ‘fast’ (up to  $110^\circ\text{C}$ ) to the ‘slow’ (above  $110^\circ\text{C}$ ) recovery seen in Fig. 4.8. To clarify the situation, the normalized  $(\mu\tau)^{-1}$  versus  $\tilde{\alpha}_{1.1}$  is displayed in Fig. 4.10. During degradation the relationship between  $(\mu\tau)^{-1}$  and  $\tilde{\alpha}_{1.1}$  is linear, as for  $\alpha_{1.25}$  (Fig. 4.8). Surprisingly,  $\tilde{\alpha}_{1.1}$  has a roughly linear relationship to  $(\mu\tau)^{-1}$  (though with negative slope)

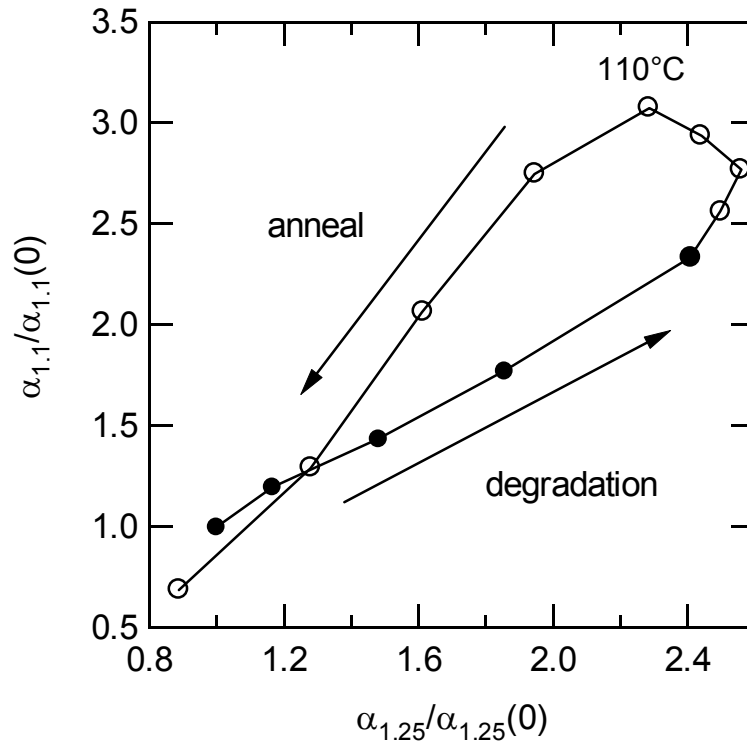


**Figure 4.9:**  $\tilde{\alpha}_{1.1}$  vs. the same  $\alpha_{1.25}$  data as Fig. 4.7; the  $110^\circ\text{C}$  transition between increase and decrease of  $\alpha_{1.1}$  is indicated.



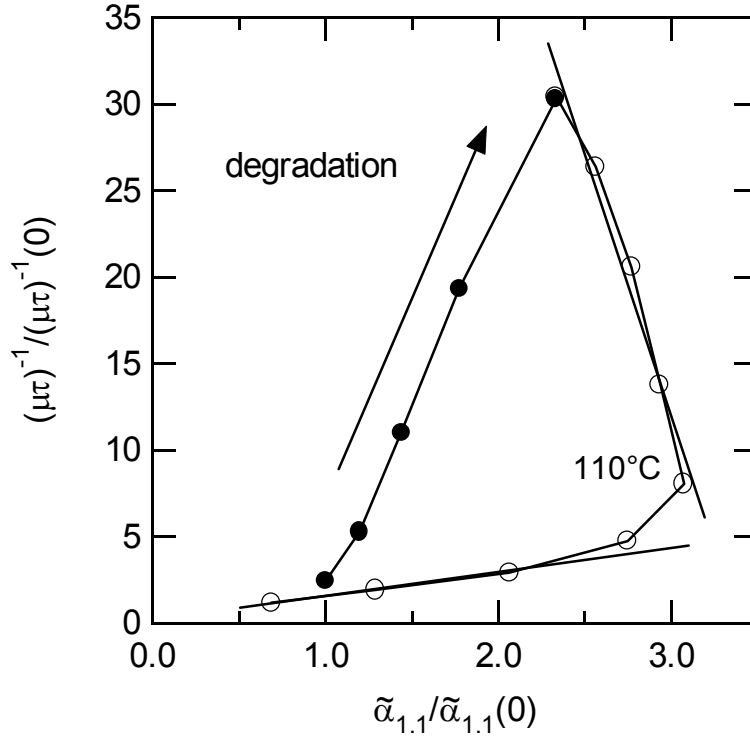


**Figure 4.10:**  $(\mu\tau)^{-1}$  vs.  $\tilde{\alpha}_{1,1}$ ; the transition  $T_a = 110^\circ\text{C}$  is indicated. Lines are guides to the eyes.

during its fast recovery below  $110^\circ\text{C}$ . In other words,  $\sigma_{\text{ph}}$  grows linearly with  $\tilde{\alpha}_{1,1}$ . Then during the slow recovery of  $(\mu\tau)^{-1}$  there is again a linear relationship between  $(\mu\tau)^{-1}$  and  $\tilde{\alpha}_{1,1}$ , but now with the expected sign of the slope. The separation of these two regions of linear slope at  $110^\circ\text{C}$  is seen very clearly in Fig. 4.10. In contrast to the breakpoint in  $\alpha_{1,25}$  shown in Fig. 4.8 is much more subtle.

The influence of the light-induced degradation on the dark Fermi level ( $E_F$ ) with respect to  $\alpha_{1,25}$  is shown in Fig. 4.12.  $E_F$  is calculated using  $\sigma_d = \sigma_0 \exp(-E_F/k_B T)$ , with  $\sigma_0 = 150 \Omega^{-1}\text{cm}^{-1}$  [55]. The increase of  $E_F$  is consistent with the observation that it moves closer to mid-bandgap during degradation [1, 35, 85]. Such shifts of  $E_F$  are, however, not the cause for light-induced degradation [35, 86, 87]. The change of  $E_F$  by about 40 meV in Fig. 4.11 appears to be small enough to support this idea. The data do not show a comparably obvious transition between two annealing regimes indicated by the previous figures. Only with some caution we may state that a significant decrease of  $E_F$  seems to appear for step-wise anneals above  $110^\circ\text{C}$ . The experimental uncertainty comes mainly from the long

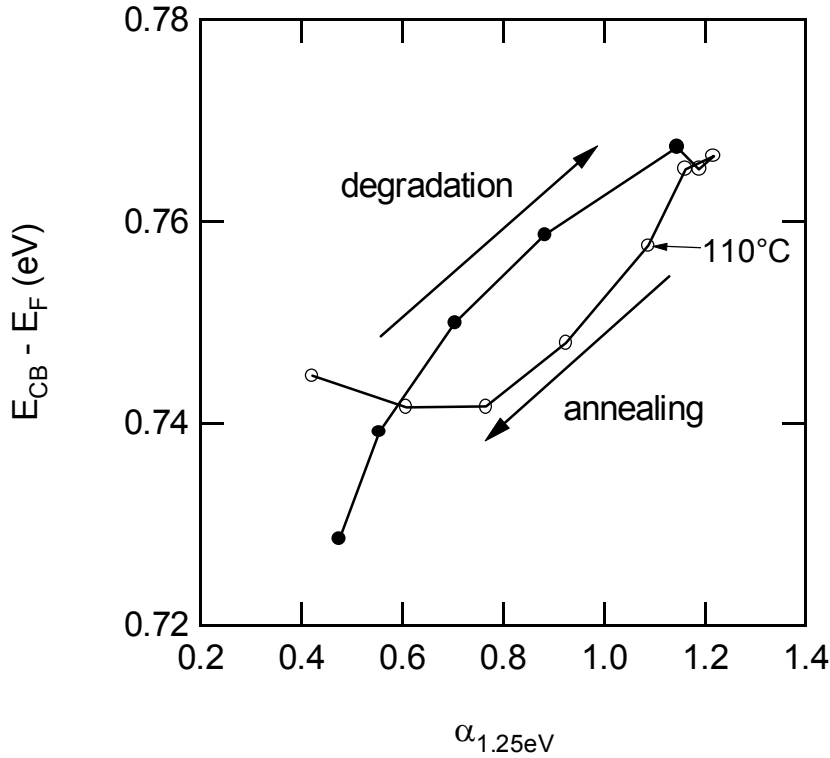


**Figure 4.11:** Dark Fermi energy  $E_F$  versus  $\alpha_{1.25}$  from the same step-wise anneal experiment as Fig. 4.8.

equilibration times of  $\sigma_d$ , especially during light-induced degradation, when trapped photo carriers have much less time to be emitted than during annealing. Within the experimental error the relationship between  $E_F$  and  $\alpha_{1.25}$  is roughly linear. The change in  $E_F$  cannot be explained by a statistical shift, which becomes visible with changing temperature [55], because the measurements for this stepwise annealing are always taken at room temperature.

Different exposure times do not significantly change the shape of the curves in Fig. 4.8. This is demonstrated in Fig 4.12, where the normalized  $(\mu\tau)^{-1}$  vs.  $\alpha_{1.25}$  is shown for different exposure times. A linear relationship with deep defect absorption during the slow anneal of  $(\mu\tau)^{-1}$  above 115°C is now clearly visible.

The fast and slow components in the  $(\mu\tau)^{-1}$  recovery can be used to characterize samples of different kind. This is demonstrated in Figs. 4.13 and 4.14, which show the loops of  $\Delta(\mu\tau)^{-1}$  versus  $\Delta\alpha_{1.25}$  and  $\Delta\tilde{\alpha}_{1.1}$ , respectively, of samples A (standard PECVD), E (HWCVD) and F (H diluted PECVD). Samples E and F were chosen for this investigation, because of their resistance to light-induced degradation [50, 88]. Table 4.1 summarizes some of the

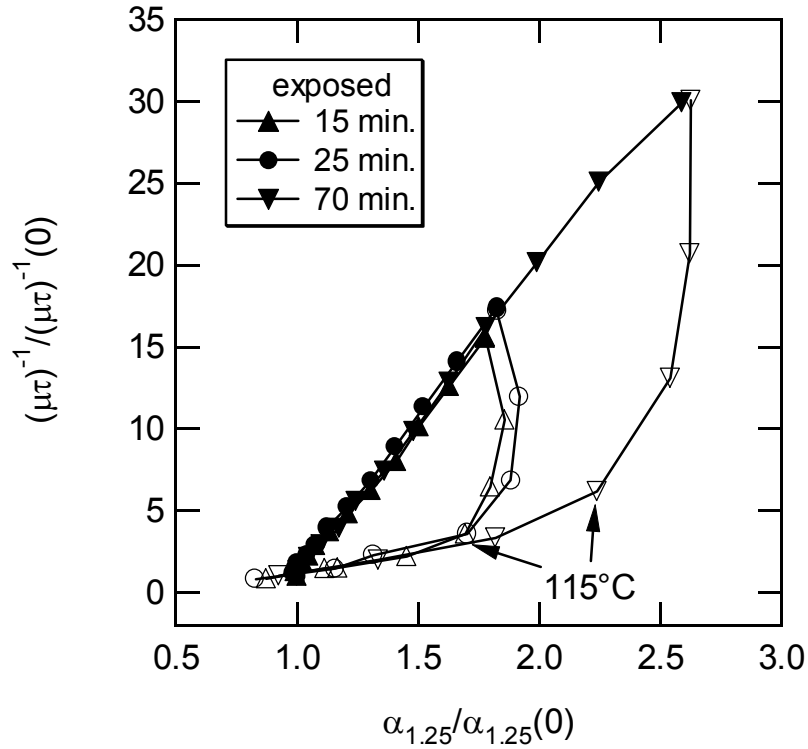


**Figure 4.12:** Step-wise anneal of sample A after 15, 25 and 73 minutes of  $200 \text{ mW/cm}^2$  exposure.  $T_a = 60, 90, 115, 140, 165,$  and  $190^\circ\text{C}$  for each experiment.  $T_a = 115^\circ\text{C}$  for each annealing curve is indicated by the arrows.

sample characteristics and the laser intensity during exposure. Hot wire deposited samples, like sample E, have in general higher values of defect densities in the annealed state, but they do not degrade as much as samples deposited by standard PECVD [88]. The three samples show characteristic differences for each  $\Delta(\mu\tau)^{-1}$  versus  $\Delta\alpha_{\text{hv}}$  loop. For example, the slopes during degradation are similar for sample A and E, but shallower for sample F [51]. Even

sample	depositions technique	exposed at ( $\text{mW/cm}^2$ )	annealed $(\mu\tau)^{-1}$ ( $\text{Vcm}^{-2}$ )	annealed $\alpha_{1.25}$ ( $\text{cm}^{-1}$ )
A	PECVD	200	$1.2 \times 10^6$	0.34
E	HWCVD	200	$1.0 \times 10^7$	6.5
F	H diluted	300	$1.5 \times 10^6$	0.41

**Table 4.1:** Legend for Figs. 4.14 and 4.15, exposure intensity and annealed values of  $(\mu\tau)^{-1}$  and  $\alpha_{1.25}$ .

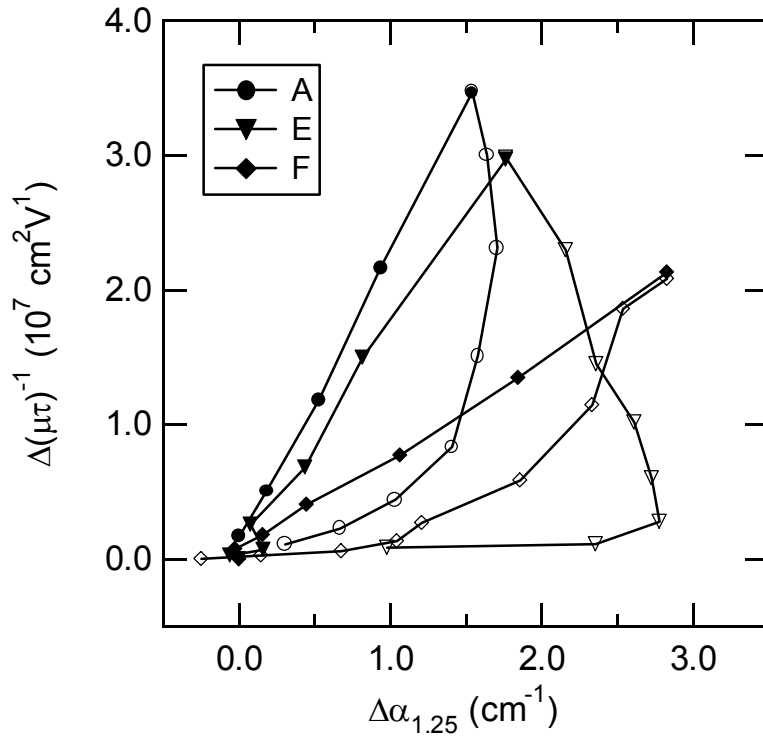


**Figure 4.13:**  $\Delta(\mu\tau)^{-1}$  vs.  $\Delta\alpha_{1,25}$  loops, for samples A, E and F.

though sample F was degraded with higher intensity than A and E, the  $(\mu\tau)^{-1}$  increased less than for the other samples, though at the same time  $N_{\text{db}}$  is higher in comparison. Again, this contradicts the assumption that there is one universal kind of  $D^0$  responsible for  $\sigma_{\text{ph}}$ . The slight  $\Delta\alpha_{1,25}$  increase of sample A is much more pronounced in sample E and does not appear at all in sample F. The  $\tilde{\alpha}_{1,1}$  measurements seem to amplify these increases. It is much higher in the fast annealing regime for sample E than sample A, whereas sample F shows at least a steeper decrease of  $\tilde{\alpha}_{1,1}$ . Simultaneously, the transition T between fast and slow annealing regime decreases from sample E to A to F, from 150 to 110 to 90°C. It is not obvious how these features connect to the different behavior of these samples during light-soaking, but it is unlikely that there is no connection at all. In the discussion chapter we will interpret this data within a self-consistent model.

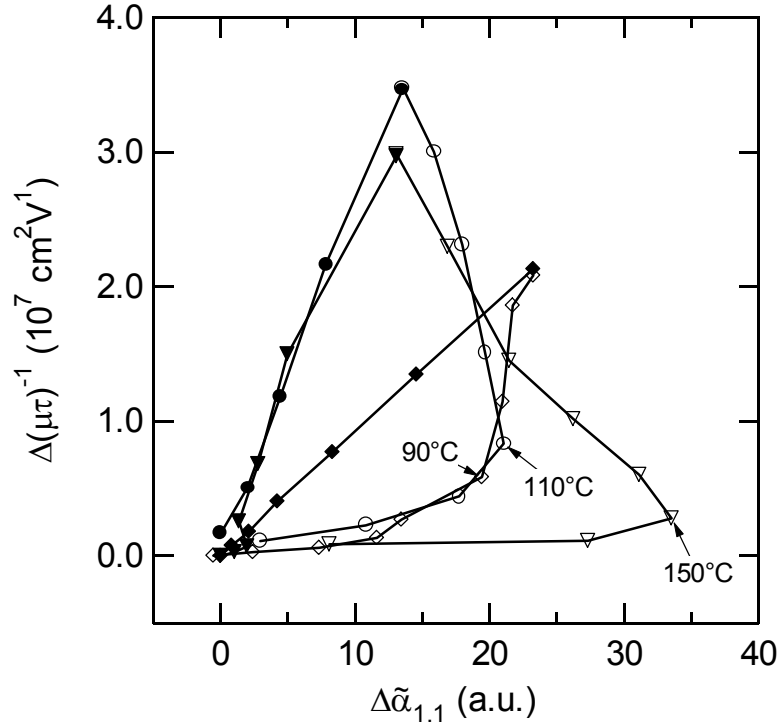
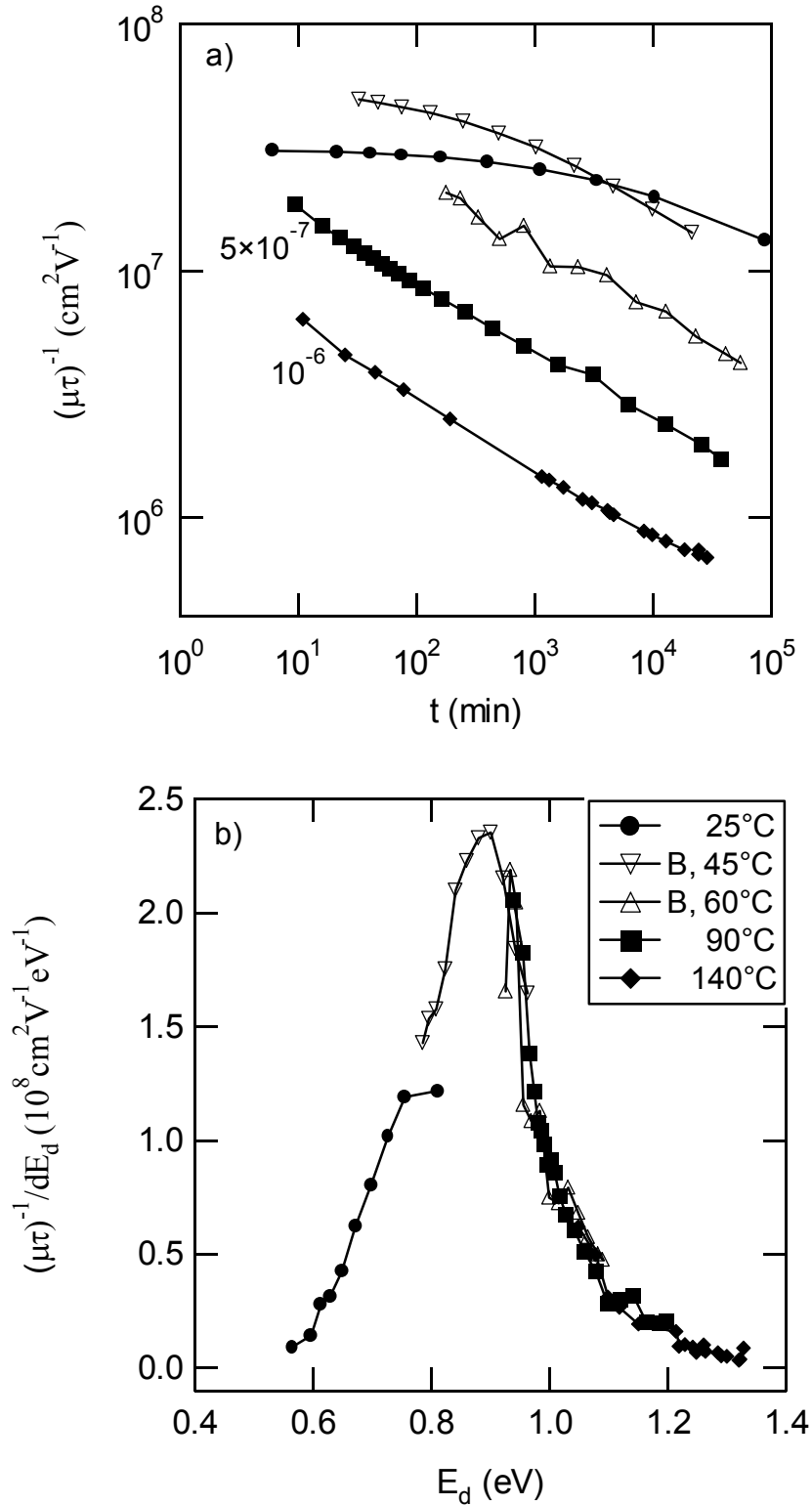


**Figure 4.14:**  $\Delta(\mu\tau)^{-1}$  vs.  $\Delta\tilde{\alpha}_{1,21}$  loops, for samples A, E and F. The transition temperature from fast to slow annealing regimes is indicated.

#### 4.2.2. Isothermal annealing at elevated temperatures

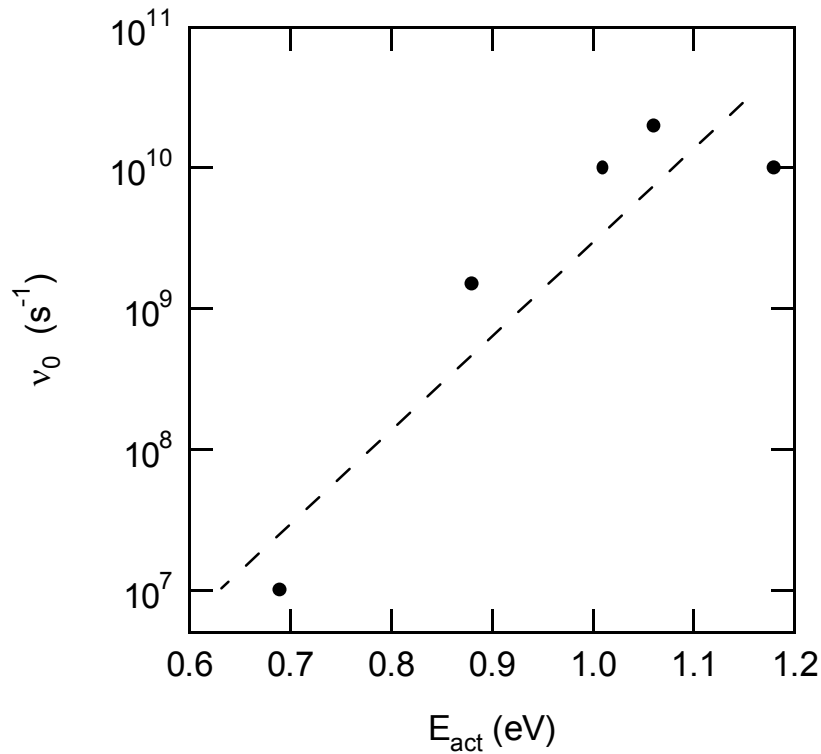
In this section, annealing activation energies ( $E_a$ ) for  $(\mu\tau)^{-1}$ ,  $\alpha_{1,25}$ , and  $\tilde{\alpha}_{1,1}$  are extracted from isothermal anneal experiments. This is done by introducing a demarcation energy  $E_d = k_B T_a \ln(v_0 t_a)$  for annealing (Equ. 2.15), with  $k_B$  the Boltzmann factor,  $T_a$  the annealing temperature,  $v_0$  a rate factor, and  $t_a$  the anneal time. All defects (represented by  $(\mu\tau)^{-1}$ ,  $\alpha_{1,25}$ , and  $\tilde{\alpha}_{1,1}$ ) with  $E_a \leq E_d$  anneal out very fast compared with  $t_a$ ; the ones with  $E_a > E_d$  anneal out very slowly compared to  $t_a$ . At constant  $T_a$ ,  $E_d$  increases logarithmically with  $t_a$ . Because we need to cover a wide range of  $E_a$ , it is necessary to isochronal anneal the samples at different  $T_a$ . Otherwise, the experiments would take too long (if  $T_a$  is rather small) or most of the defects will have annealed out (if  $T_a$  is chosen to high). The  $E_a$  distributions of  $(\mu\tau)^{-1}$ ,  $\alpha_{1,25}$ , and  $\tilde{\alpha}_{1,1}$  are calculated using the approach described in Section 2.3.

Fig. 4.16a shows how  $(\mu\tau)^{-1}$  recovers at different  $T_a$  with  $t_a$  for sample A and B. With the background of Section 4.1., it is not surprising that the defects determining  $(\mu\tau)^{-1}$  anneal



**Figure 4.15:** a) Sample A recovery of  $(\mu\tau)^{-1}$  with anneal time,  $t_a$ , at the indicated  $T_a$ .  $T_a = 45$  and  $60^\circ\text{C}$  data are of sample B.  $(\mu\tau)^{-1}$  was measured at level  $10^7 \Omega^{-1} \text{cm}^{-1}$  except for the three highest  $T_a$  as indicated in the graph. b)  $(\mu\tau)^{-1}$  versus  $E_d$  using the data of a).

out even at room temperature. The procedure described in Section 2.3. is applied to calculate the  $E_a$  distribution of  $(\mu\tau)^{-1}$ . However, if a constant  $\nu_0$  is assumed in  $E_d = k_B T_a \ln(\nu_0 t_a)$ , then the different  $T_a$  data do not give the same  $(\mu\tau)^{-1}(E_a)$  distribution. This is not very surprising, as  $\nu_0$  in a-Si:H follows the Meyer-Neldel rule [71], i.e. it depends on  $E_a$  in a-Si:H [72, 89]. In order to match the  $d(\mu\tau)^{-1}/dE_d(E_a)$  distributions measured at different  $T_a$ , the following procedure is applied:  $\nu_0$  is set to  $10^{10} \text{ s}^{-1}$  [8, 36] for the  $140^\circ\text{C}$  data. The best  $\nu_0$  for matching the  $140^\circ\text{C}$  data is use for each of the  $(\mu\tau)^{-1}(E_a)$  data. The  $\nu_0$  thus obtained are plotted in Fig. 4.16. The dashed line indicates a Meyer-Neldel slope of  $E_{MN} = 65 \text{ meV}$ , which is in the upper limit of the observed values [72, 89]. The  $\nu_0$  values of Fig. 4.16 are used for the calculations of the  $E_a$  distribution of  $\alpha_{1.25}$ , and  $\tilde{\alpha}_{1.1}$ . Fig. 4.15b displays the matched  $E_a$  distributions of  $(\mu\tau)^{-1}$  derived from the data in Fig. 4.15a, with a maximum of the distribution at about  $0.9 \text{ eV}$  [36].



**Figure 4.16:** *The change in  $\nu_0$  with  $E_{act}$ , typical for a Meyer-Neldel behavior. The line indicates an  $E_{MN} = 65 \text{ meV}$  and serves as a guide to the eye.*

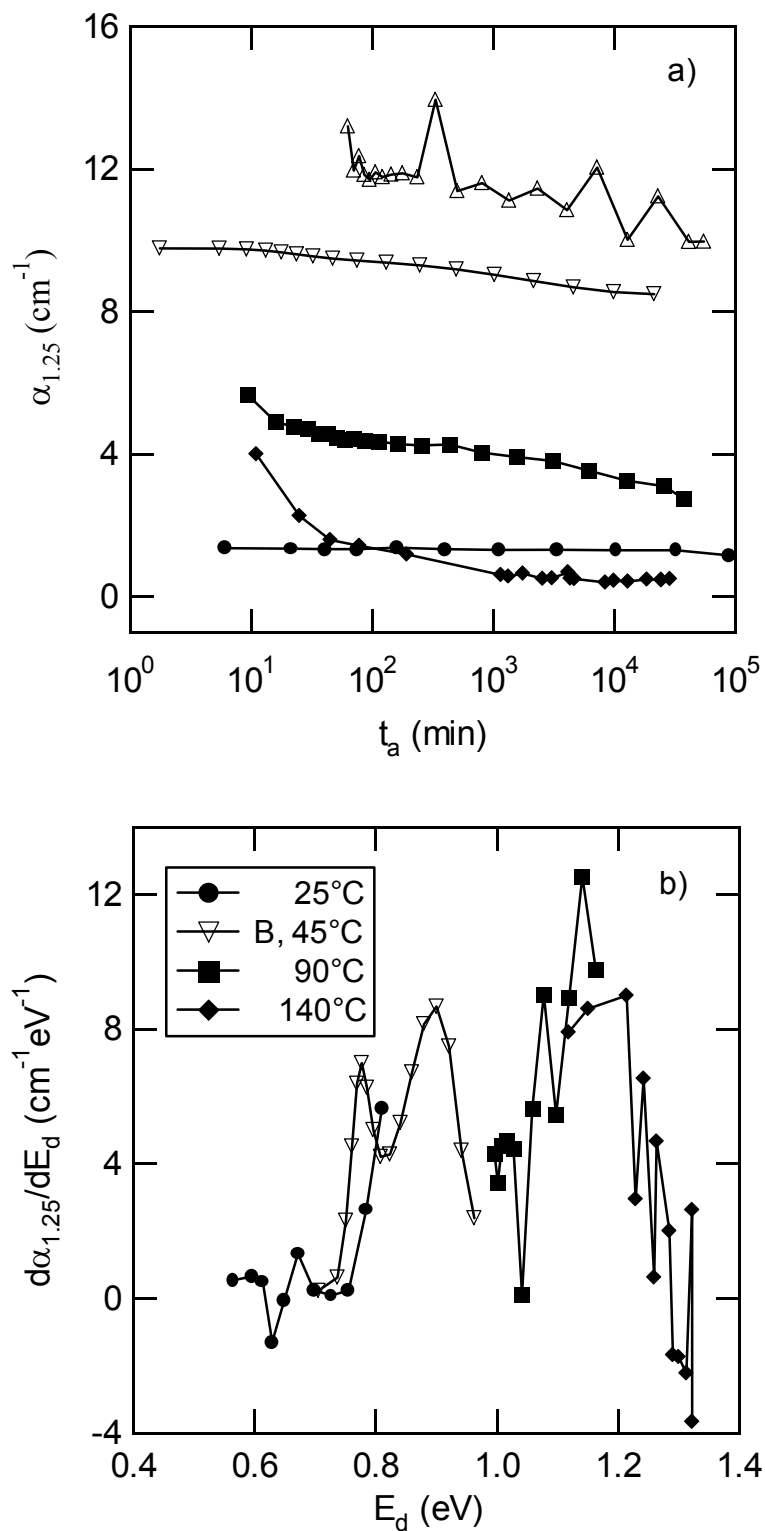
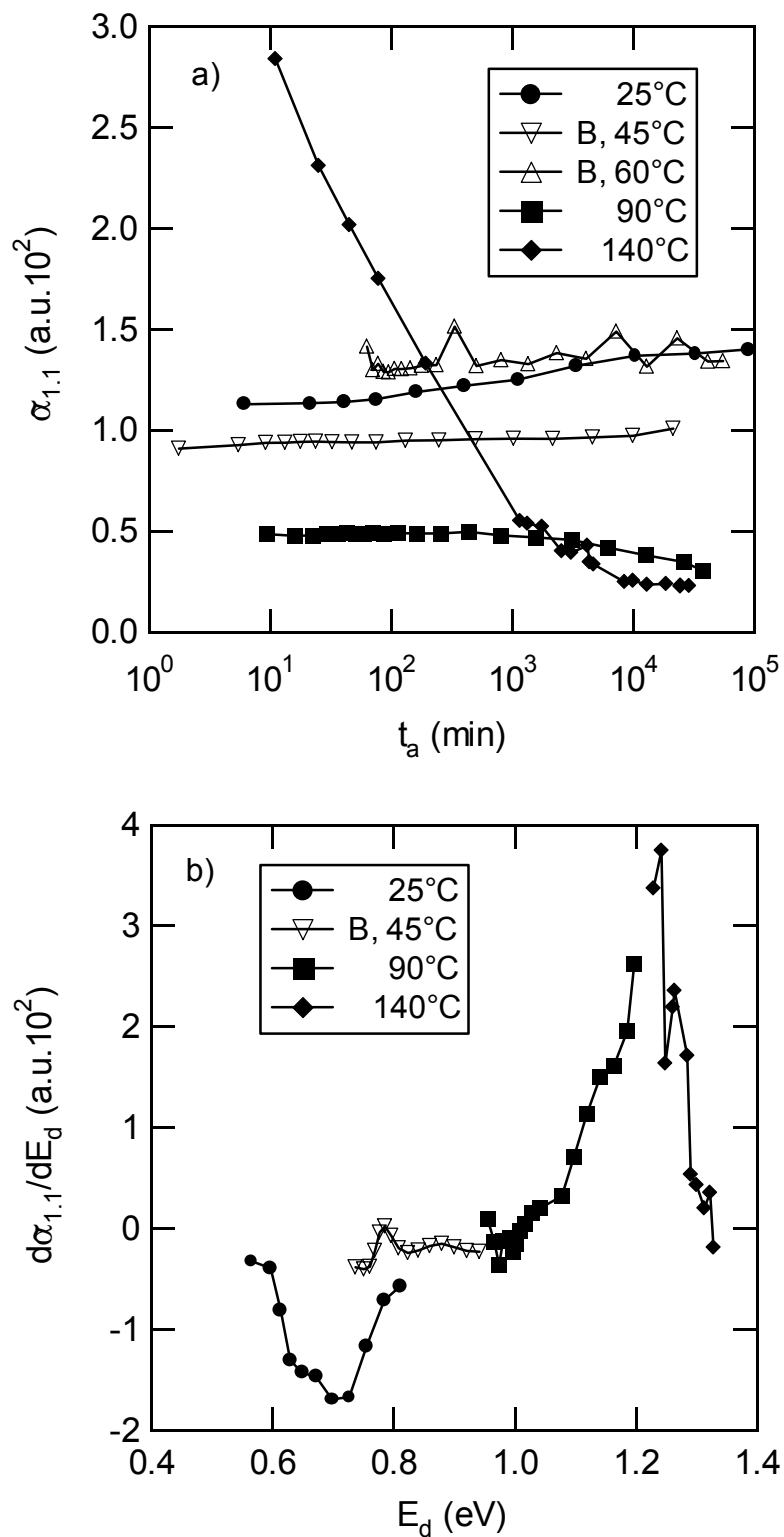


**Figure 4.17:** a) Isothermal anneal data of  $\alpha_{1,25}$  taken at the same time as the data of Fig. 4.15. b) Derivative of the data in a) with respect to the demarcation energy procedure described in the text. The 60°C data was not used because of its high noise level.



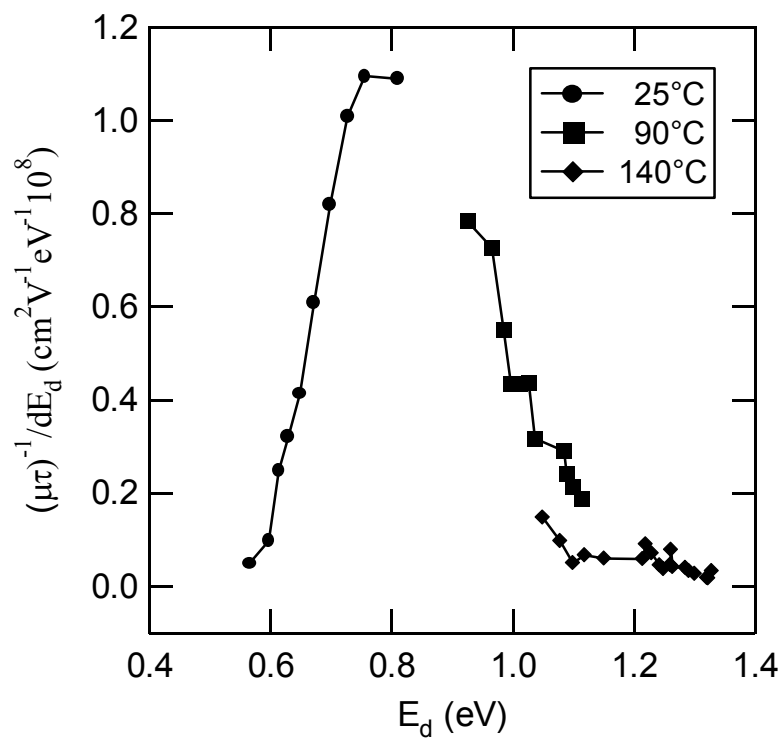
The deep defect absorption is measured at the same time as  $(\mu\tau)^{-1}$ . The recovery of  $\alpha_{1.25}$  for different  $T_a$  is shown in Fig. 4.17a. Because of the smaller photocurrents, the absorption data is considerably noisier than the  $(\mu\tau)^{-1}$  data. This noise is amplified, when the data of Fig. 4.17a is differentiated with respect to  $E_d$ . The result is shown in Fig. 4.17b. In this figure, some of the scattered data were removed for clarity and the 60°C derivative data is left out completely because its noise level is about 10 higher than the useful signal. Despite the noise, it is possible to identify a trend in the data of Fig. 4.17b. Two maxima can be identified, one at about 0.9 and the other somewhat higher at about 1.15 eV. Apparently, there is a contribution of defect annealing at 0.9 eV, which is the range at which the dominant  $(\mu\tau)^{-1}$  annealing takes place. The 1.2 eV component is expected. This  $E_a$  has often been observed in the annealing of  $D^0$  [36, 69, 70, 90]. It becomes again doubtful that the  $D^0$  dominate  $\sigma_{ph}$ , because of the 0.3 eV higher  $E_a$  compared to  $(\mu\tau)^{-1}$  (Fig. 4.15b). With respect to the upcoming  $\tilde{\alpha}_{1.1}$  data it shall be noted that the  $\alpha_{1.25}(E_a)$  spectrum in Fig. 4.17b is essentially zero below 0.8 eV.

Fig. 4.18 shows the annealing behavior of  $\tilde{\alpha}_{1.1}$ , which is of particular interest, because of the increase seen during isochronal anneals (see Fig. 4.10 and 4.14). The use of a cut-off filter for measuring  $\tilde{\alpha}_{1.1}$  results in a larger  $\sigma_{ph}$  at this photon energy with a reasonable noise level (except again for the 60°C data). An increase in  $\tilde{\alpha}_{1.1}$  is also observed for isothermal annealing at  $T_a = 25^\circ\text{C}$  (Fig. 4.18a). At first sight, the increase in  $\tilde{\alpha}_{1.1}$  seems to indicate an increase in defect density. However, as emphasized in Section 2.3.2. CPM measures the absorption due to excitation of carriers from *occupied* states. In Chapter 5, it will be argued that this increase in  $\tilde{\alpha}_{1.1}$  can be interpreted as a change in  $D^0$  occupation due to the annealing of a recombination center other than  $D^0$ . It is proposed that the annealing of recombination defects, to which ESR and CPM are not sensitive, can increase the occupancy of the DBs and therefore increase the signal measurable for  $\tilde{\alpha}_{1.1}$ . If the increase in  $\tilde{\alpha}_{1.1}$  is really a second order effect of recombination center annealing, then the  $\tilde{\alpha}_{1.1}$  signal during isothermal annealing can be used to calculate its  $E_a$ . This was done for Figs. 4.15b and 4.17b. The isothermal anneal data of  $\tilde{\alpha}_{1.1}$  is shown in Fig. 4.18a. Their derivative with respect to  $E_d$  is displayed in Fig. 4.18b (the derivative of the 60°C data is left out again, because it is too noisy). The increase of the 25°C  $\tilde{\alpha}_{1.1}$  signal corresponds to the negative derivative regime with its minimum at about 0.7 eV. In this regime, the  $E_a$  distribution of  $\alpha_{1.25}$  is flat and zero. Therefore, the data in Fig. 4.18b indicates a thermally activated process that is not connected



**Figure 4.18:** a) Isothermal annealing of  $\tilde{\alpha}_{1,1}$  at different  $T_a$  of samples A and B, measured at the same time as  $(\mu\tau)^{-1}$  of Fig. 4.15. b) Derivative of the data in a) except for the 60°C data, which has a very high noise level.

to the annealing of  $D^0$ . This is consistent with the assumption that a recombination defect other than  $D^0$  anneals in this regime. It is reasonable to identify again the maximum at about 1.2 eV with the annealing of  $D^0$ . Apparently, however, there is no annealing component in the 0.9 eV regime like in Fig. 4.17b for  $\alpha_{1.25}$ .



**Figure 4.19a:**

*Annealing activation energy distribution of  $(\mu\tau)^{-1}$  for sample C.*

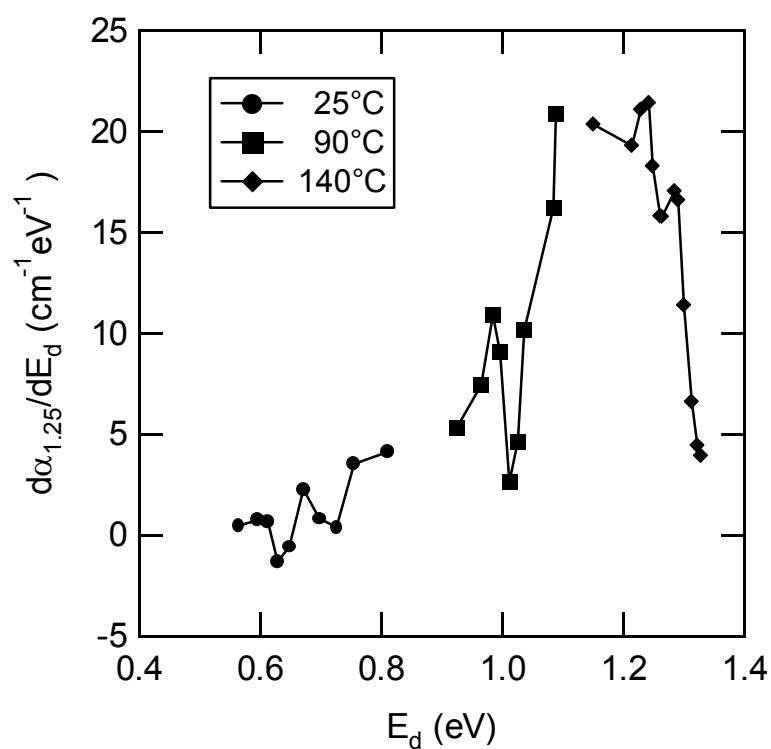


**Figure 4.19b:**

*Annealing activation energy distribution of  $\alpha_{1.25}$  for sample C.*

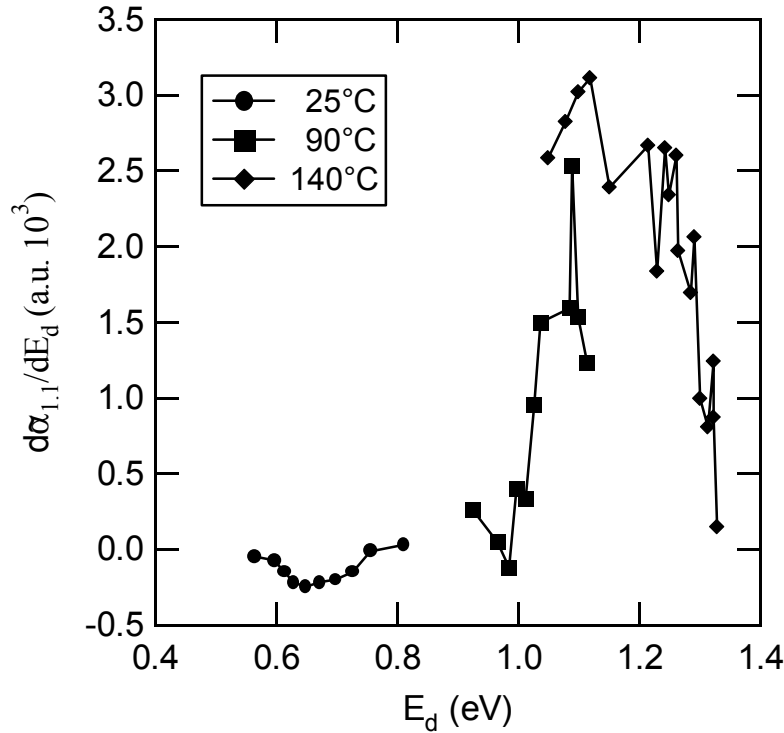


**Figure 4.19c:**

*Annealing activation  
distribution energy of  $\tilde{\alpha}_{1.1}$   
for sample C.*

The NREL PECVD sample C shows a similar behavior as samples A and B. In Fig. 4.19, the  $E_a$  spectra of  $(\mu\tau)^{-1}$ ,  $\alpha_{1.25}$ , and  $\tilde{\alpha}_{1.1}$  are displayed using the same values for  $\nu_0$  of Fig. 4.16 for the calculation of  $E_d^1$ . Fig. 4.19a shows that for sample C, the maximum of the  $(\mu\tau)^{-1}$  annealing seems to be shifted to a somewhat smaller value ( $\approx 0.8$  eV) compared to 0.9 eV in sample A and B. Whether or not this is a true shift between samples cannot be decided, because of the uncertainties in  $\nu_0(E_a)$ . In the  $\alpha_{1.25}$  versus  $E_d$  data of Fig. 4.19b the maximum for the  $D^0$  annealing is at 1.2 eV, which agrees with the data for sample A and B. The  $\tilde{\alpha}_{1.1}$  annealing shows a weak minimum at about 0.65 eV and a maximum at the  $D^0$  annealing maximum at 1.2 eV.

Summarizing the salient features of the  $(\mu\tau)^{-1}$ ,  $\alpha_{1.25}$ , and  $\tilde{\alpha}_{1.1}$  isothermal annealing experiments, we find that the  $E_a$  distribution of  $D^0$  ( $E_a \approx 1.2$  eV) is clearly different from the  $E_a \approx 0.8 - 0.9$  eV for  $(\mu\tau)^{-1}$ . There is a minimum in the  $\tilde{\alpha}_{1.1}$   $E_a$  distribution at around 0.7 eV, and a maximum at the same  $E_a$  as the  $D^0$  distribution.

<sup>1</sup> This is probably the reason why the  $(\mu\tau)^{-1}$  data of the different  $T_a$  do not match perfectly well. For different samples, there are most likely slightly different dependencies between the  $\nu_0(E_a)$  dependencies. But in lack of more information on  $\nu_0(E_a)$  for sample C, the chosen approach seems the best solution.

### 4.2.3. Connection between step-wise isochronal and isothermal annealing

In this section we will show how the fast ( $T_a \leq 110^\circ\text{C}$ ) and slow ( $T_a > 110^\circ\text{C}$ ) annealing regime in the isochronal step-wise anneals and the  $E_a < 1.0$  eV and  $E_a > 1.0$  eV regime in the isothermal experiments, respectively, are connected. For this purpose, sample A is isochronally step-wise annealed (as in Section 4.2.1) after isothermal anneals at different anneal temperature  $T_a$  and duration  $t_a$ . Fig. 4.20 sketches the experimental procedure and Fig. 4.21 summarizes the results in a  $(\mu\tau^{-1})$  versus  $\alpha_{1.25}$  plot. For this figure,  $(\mu\tau^{-1})$  and  $\alpha_{1.25}$  are normalized to their fully annealed values. The full and dashed lines represent the degradation and step-wise annealing of sample A, without any isothermal annealing. These are the equivalent data as in Fig. 4.8 of Section 4.2.1. and serve as a reference for the results of this section. For each experiment, sample A was degraded for 73 min at  $200 \text{ mWcm}^{-2}$ . The degradation data are not shown. The final degraded states after light-soaking are within about 20% of the reference data. The first measurement of each step-wise anneal data set is marked with the annealing time and temperature of the preceding isothermal anneals. The  $(\mu\tau^{-1})$  on  $\alpha_{1.25}$  data during isothermal room temperature annealing are also added in Fig. 4.20 and marked as (+).

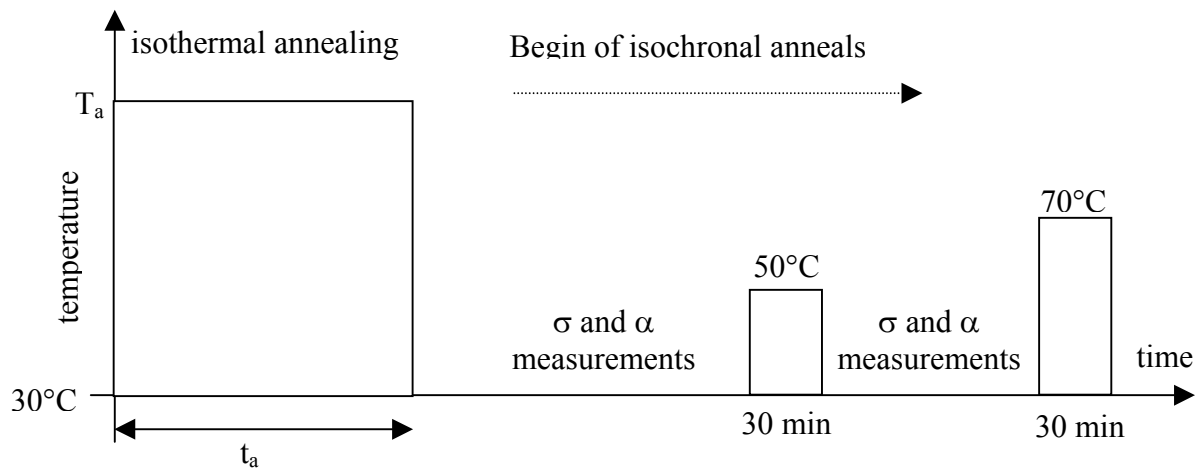


**Figure 4.20:** Schematic of the experimental procedure: After isothermal anneals of time  $t_a$  at temperature  $T_a$ , the sample is isochronal step-wise annealed as described in Section 3.5.2.

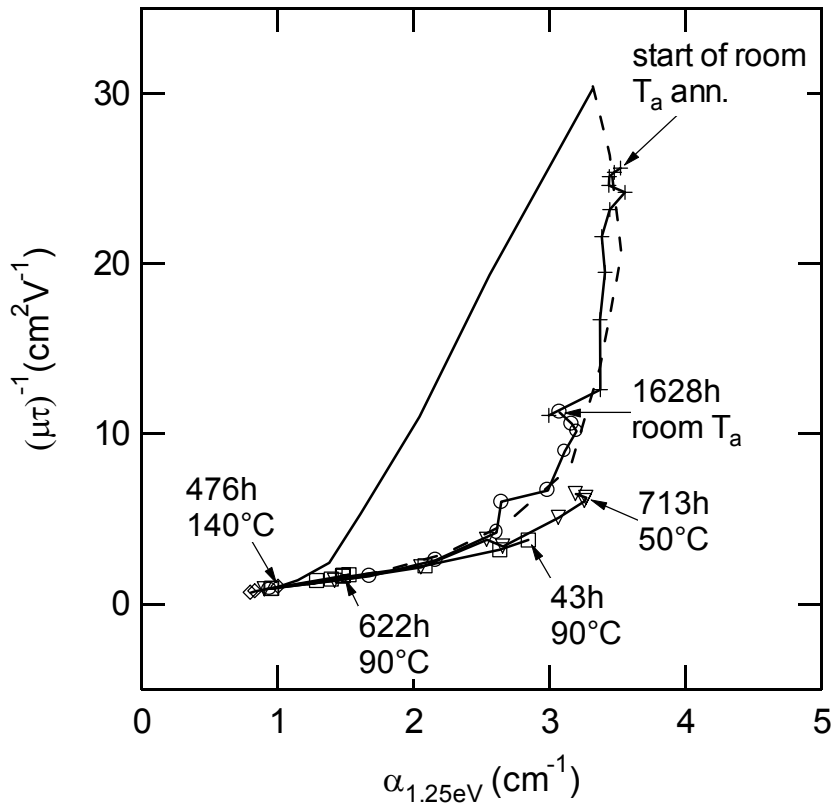


**Figure 4.21:** Step-wise anneal data after preceding isothermal anneals. The first point of each data set is labeled with the different  $t_a$  and  $T_a$  of the isothermal anneals. The full and dashed lines are data without isothermal annealing and serve as reference. The isothermal room  $T_a$  annealing data are also included.

The sample is closer to the fully annealed state whether it is annealed for longer times at the same  $T_a$ , e.g. 622 versus 43 h at 90°C in Fig. 4.21, or at higher  $T_a$  for about the same time, e.g. 622 h at 90°C versus 713 h at 50°C in this figure. All step-wise anneal data trace the reference data independent of their pretreatment. This includes the isothermal room temperature annealing. It is therefore possible to identify corresponding regimes in the step-wise and isothermal anneals data. In Figs. 4.15b and 4.19a, we see how  $(\mu\tau)^{-1}$  essentially anneals out for  $E_a < 1.0$  eV. This coincides with the fast  $(\mu\tau)^{-1}$  annealing below about 110°C in a step-wise anneal experiment. Similarly, the main part of the light-induced  $\alpha_{1.25}$  increase anneals out in the regime of  $E_a > 1.0$  eV (Figs. 4.17b and 4.19b), which corresponds to the slow anneal of  $(\mu\tau)^{-1}$  above about 110°C in the step-wise anneal experiment. We draw two conclusions from the correspondence of these regimes: (1) Below 110°C, during the fast recovery of  $\sigma_{ph}$ , exists a thermally activated process with  $E_a \approx 0.7$  eV, which is more likely to

be involved in the fast recovery of  $\sigma_{ph}$  than the  $D^0$ 's are. (2) During the slow anneal regime, above  $110^\circ\text{C}$  in step-wise anneal experiments, the  $D^0$  dominate ( $\mu\tau^{-1}$ ). This second conclusion has consequences for capture coefficient measurements. If these are measured with SWE experiments in the temperature regime of fast annealing, then the results will always contain components that are not determined by  $D^0$ 's, and result in too high values.

Next, we have a closer look at the transition between the fast and slow annealing regimes in step-wise anneal experiments. Heating the sample up to  $T_a = 90^\circ\text{C}$  brings us close to this transition (Figs. 4.9 and 4.10), and a following isothermal annealing at this  $T_a$  will cover both regimes, if the annealing time is long enough. The step-wise anneal data in Fig. 4.21 demonstrate that this is true for the isothermal annealing at  $T_a = 90^\circ\text{C}$  for 622 h. This indicates that the isothermal anneal ended close to the fully annealed state. Fig. 4.22 shows the  $T_a = 90^\circ\text{C}$ ,  $t_a = 622$  h isothermal anneal data in a ( $\mu\tau^{-1}$ ) versus  $\tilde{\alpha}_{1,1}$  plot. Clearly, there is an abrupt transition between two regimes after about 6 hs of annealing. The  $\tilde{\alpha}_{1,1}$  signal increases

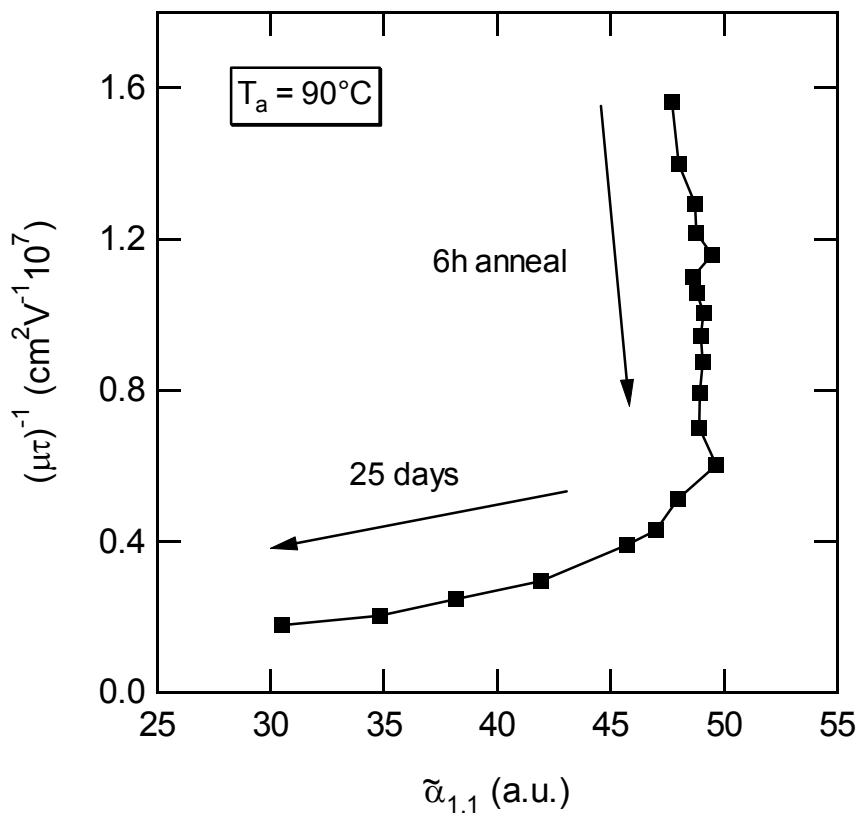


**Figure 4.22:**  $(\mu\tau)^{-1}$  versus  $\tilde{\alpha}_{1,1}$  for the isothermal anneal data at  $90^\circ\text{C}$ . The arrows indicate how the first 6 hs annealing are sufficient to get to the transition point, but 25 days for the remaining rest of the data.

slightly. This is the small remainder of the total  $\tilde{\alpha}_{1,1}$  increase and is barely visible in this figure, because most of it annealed out already (see Fig. 4.10). The two regimes can be identified as the fast and slow annealing regime in the step-wise anneal experiments, or as the two regimes above and below  $E_a \approx 1.0$  eV found in the isothermal experiments. The significance of this data is that they show how abrupt the transition between these two regimes happens. This becomes much clearer than in step-wise anneal experiments.

Fig. 4.23 shows the  $(\mu\tau)^{-1}$  versus  $\alpha_{1,25}$  data of sample A at the indicated temperatures. The transition between fast and slow annealing at  $90^\circ\text{C}$  is not as dramatic as in Fig. 4.22, but is nevertheless clear. Assuming that the  $D^0$  are the only recombination centers during the  $140^\circ\text{C}$  annealing, the slope in this graph determines the effectiveness of  $D^0$  to capture free electrons. It is related to the proportionality constants  $C$  between electron lifetime and defect density ( $N_{\text{db}} = 7.0 \times 10^{15} \text{cm}^{-2} \times \alpha_{1,25}$ ) introduced in Section 2.1. The dashed line is fitted by eye and with the slope determined by  $(\mu\tau)^{-1} = m \times \alpha_{1,25}$ ,  $C_{\text{db}}$  can be calculated as

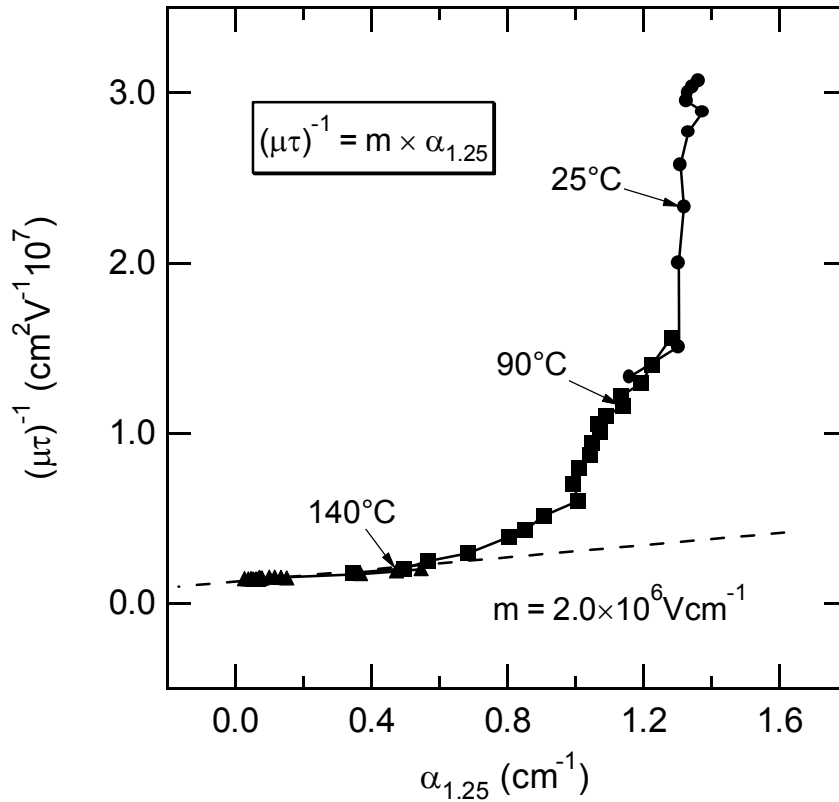


**Figure 4.23:**  $(\mu\tau)^{-1}$  versus  $\alpha_{1,25}$  for the isothermal anneal data at the indicated  $T_a$ . The slope for the linear relationship between  $(\mu\tau)^{-1}$  and  $\alpha_{1,25}$  is indicated for the  $140^\circ\text{C}$  data.



$C_{db} = (\mu \times m)/7.0 \times 10^{15} \text{ cm}^{-2}$ . With  $m = 2.0 \times 10^6 \text{ V cm}^{-1}$ ,  $\mu = 1 \text{ cm}^2 \text{ V}^{-1} \text{ s}^{-1}$  and assuming a purely ballistic model for  $C_{db}$  [36, 52] this yields  $2.9 \times 10^{-17} \text{ cm}^2$  for the  $D^0$  electron capture cross section. It is not surprising that this value is 10 – 100 smaller than reported by others [36, 61, 91]. Because those measurements are commonly done at room temperature, where the calculated capture cross section contains the high capture efficiencies of the fast annealing regime. The slope of the 25°C isothermal annealing data is nearly vertical (it is even negative for sample E, Fig. 4.13). If these data were interpreted as measurement for the electron capture efficiency of  $D^0$  ( $C_{db}$ ), then this would lead to the conclusion that during the fast annealing of  $(\mu\tau)^{-1}$ ,  $D^0$  have a  $C_{db}$  several order of magnitudes higher than during the following slow annealing process. Another approach is taken in Chapter 5.

In summary, there are two distinct regimes of annealing, which abruptly change from one to another. The first one is associated with the fast annealing of  $(\mu\tau)^{-1}$ . Its  $E_a$  is about 0.8 – 0.9 eV. There is no significant change in  $D^0$  density (measured by means of  $\alpha_{1.25}$ ), but the defect absorption signal  $\tilde{\alpha}_{1.1}$  is well correlated to the decrease in  $(\mu\tau)^{-1}$ . The  $\tilde{\alpha}_{1.1}$  signal increases instead of decreases during thermal annealing. In the second regime of annealing, the remainder of the light-induced  $(\mu\tau)^{-1}$  as well as all the entire  $D^0$  increase anneal out.

### **4.3. Light-induced degradation at elevated temperatures**

Section 4.2 dealt with the fast and slow  $(\mu\tau)^{-1}$  annealing component of light-soaked samples. This section looks in more detail into the consequences of these two components during degradation. We can expect that after light-soaking at elevated temperature ( $T_{\text{exp}}$ ), less of the fast annealing component remains than during room temperature light-soaking, because part of it has annealed already. For the experiments in this section, the annealed sample B is heated to different exposure temperatures  $T_{\text{exp}}$  each time, and then light soaked at  $300 \text{ mW cm}^{-2}$  for 73 min. The light-soaking is interrupted frequently, and all measurements are taken at  $T_{\text{exp}}$ .

Fig. 4.24 and 4.25 show  $(\mu\tau)^{-1}$  and  $\alpha_{1.25}$ , respectively, for sample B versus  $t_{\text{exp}}$  at the exposure temperatures ( $T_{\text{exp}}$ ) listed in the figure captions. Fig. 4.24 demonstrates not only how  $(\mu\tau)^{-1}$  decreases with increasing  $T_{\text{exp}}$  (see 3.5.3), but also how the power  $\delta \approx 0.3$  in the law  $(\mu\tau)^{-1} \propto t^{\delta}$  observed at room temperature decreases to a value of about 0.1. Similarly,

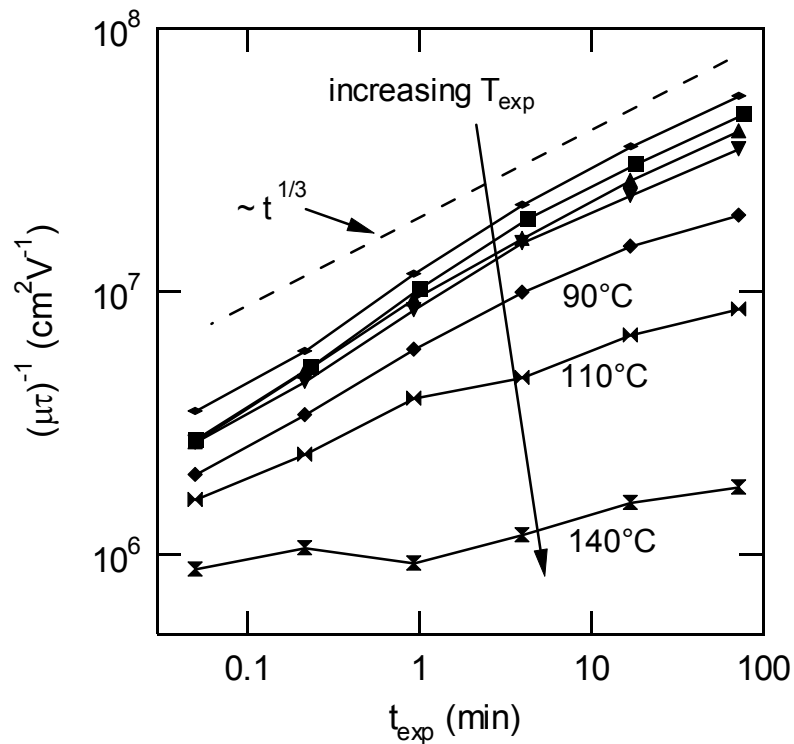


**Figure 4.24:**  $(\mu\tau)^{-1}$  versus  $t_{exp}$  for sample B during exposure at  $T_{exp} = 28, 40, 50, 60, 90, 110,$  and  $140^\circ\text{C}$ . Slope of  $1/3$  added for reference.

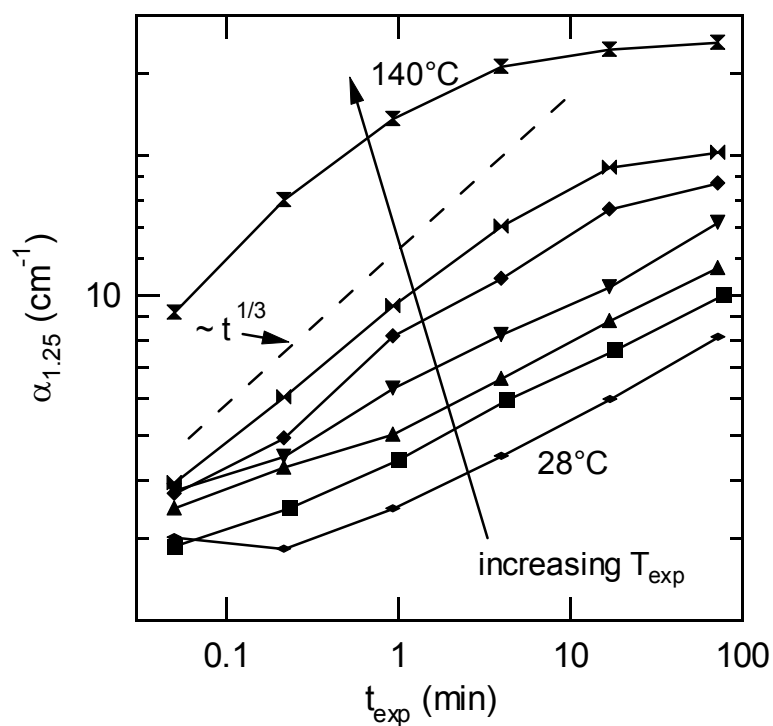


**Figure 4.25:**  $\alpha_{1.25}$  versus  $t_{exp}$  measured at the same time as Fig. 4.24.

Fig. 4.25 shows how  $\alpha_{1.25}$  increases due to the increase in  $T_{\text{exp}}$ . However, here  $\alpha_{1.25}(t)$  approaches  $t^{1/3}$  as  $T_{\text{exp}}$  increases. Also, for the highest  $T_{\text{exp}}$ ,  $\alpha_{1.25}$  clearly starts to saturate after about 10 min exposure. If  $(\mu\tau)^{-1}$  saturates at 140°C, it is not visible in Fig. 4.24 due to the small magnitude of the increase during degradation.  $(\mu\tau)^{-1}$  versus  $\alpha_{1.25}$  is plotted in Fig. 4.26 for each  $T_{\text{exp}}$  to check, whether the recombination centers created during illumination are related to the light-induced  $N_{\text{db}}$ . The data are corrected for their temperature dependence (see Section 3.5.3.), so that they can be compared to the data at 28°C; at all  $T_{\text{exp}}$   $(\mu\tau)^{-1}$  is linear proportional to  $\alpha_{1.25}$  [29]. The slopes from the relationship  $(\mu\tau)^{-1} = m \times \alpha_{1.25}$  are determined from Fig. 4.26 and plotted in Fig. 4.27. For  $T_{\text{exp}} = 110$  and 140°C, only the points taken before the saturation began were used for determining  $m$ . If  $D^0$  were the only recombination centers, then Fig. 4.27 would show that the capture efficiency of  $D^0$ s decreases between room  $T_{\text{exp}}$  and 140°C, by about a factor of 10. This is far less than the several orders of magnitude

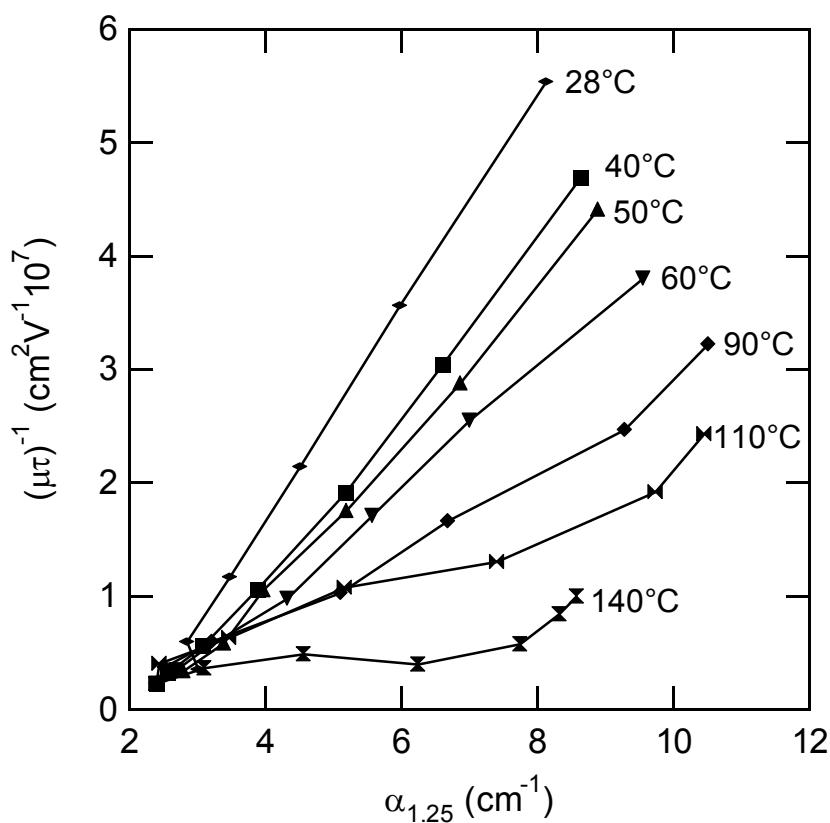


**Figure 4.26:**  $(\mu\tau)^{-1}$  versus  $\alpha_{1.25}$  at the indicated  $T_{\text{exp}}$ .  $(\mu\tau)^{-1}$  and  $\alpha_{1.25}$  are corrected for their temperature dependence in order to compare them to the 28°C data. Symbols correspond to Fig. 4.24 and 4.25.

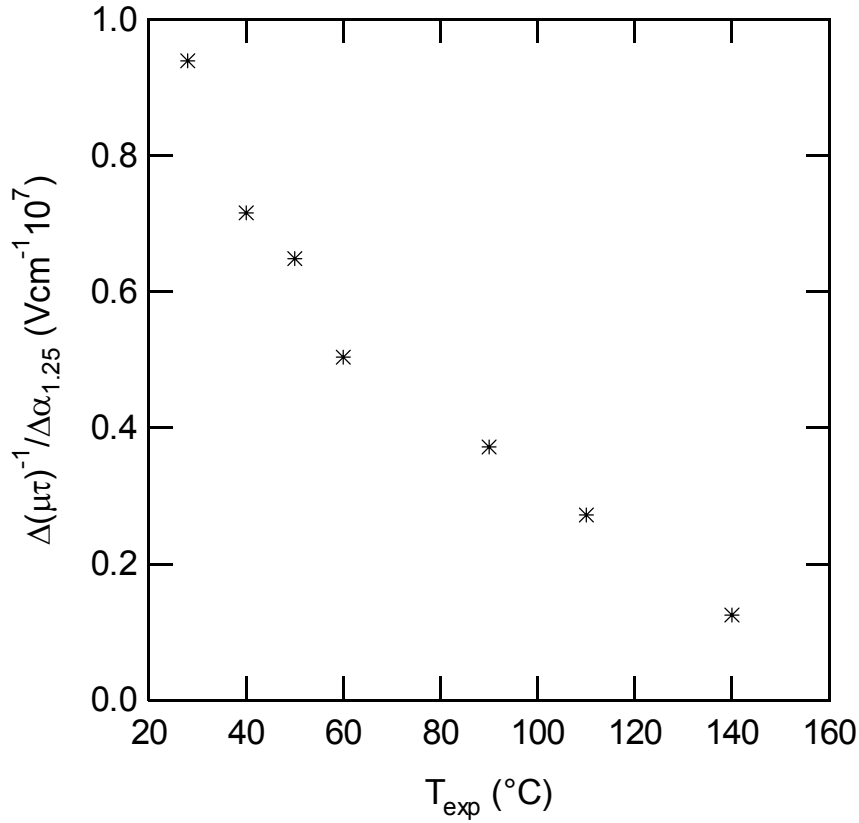


**Figure 4.27:** Slopes of Fig. 4.26 versus  $T_{exp}$ .

we would expect from our analysis of Fig. 4.23. Sections 4.1 and 4.2 suggest a degradation component not connected to  $D^0$ s. From the step-wise anneal data in Fig. 4.9 and 4.10, we

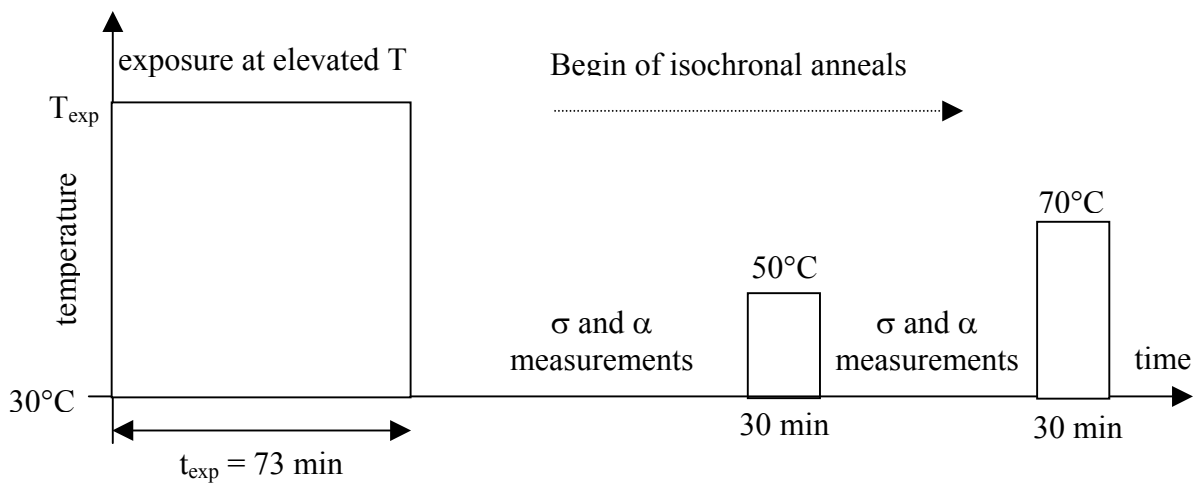


**Figure 4.28:** Schematic of the experimental procedure: After exposure at elevated  $T_{exp}$ , the sample is isochronal step-wise annealed as described in Section 3.5.2.

conclude that this component must be present during light-soaking below exposure temperatures of  $110^{\circ}\text{C}$ . It is therefore reasonable to assume that the decrease in slopes of Fig. 4.26 is significantly influenced by the reduced presence of this component. In the following, we will argue that the slope of the  $140^{\circ}\text{C}$  data in Fig. 4.26 presents a lower limit, i.e. any exposures for  $T_{\text{exp}} \geq 140^{\circ}\text{C}$  will yield the same slopes in a  $(\mu\tau)^{-1}$  versus  $\alpha_{1.25}$  plot.

During exposures above  $110^{\circ}\text{C}$ , the fast annealing component of  $\sigma_{\text{ph}}$  might be expected to anneal during degradation. If this is the case, then only  $D^0$ 's determine  $\sigma_{\text{ph}}$ , and therefore  $(\mu\tau)^{-1}$  should depend linearly on  $\alpha_{1.25}$  during degradation *and* annealing. In other words, the anneal data should retrace the degradation data in a  $(\mu\tau)^{-1}$  versus  $\alpha_{1.25}$  plot. This is in contrast

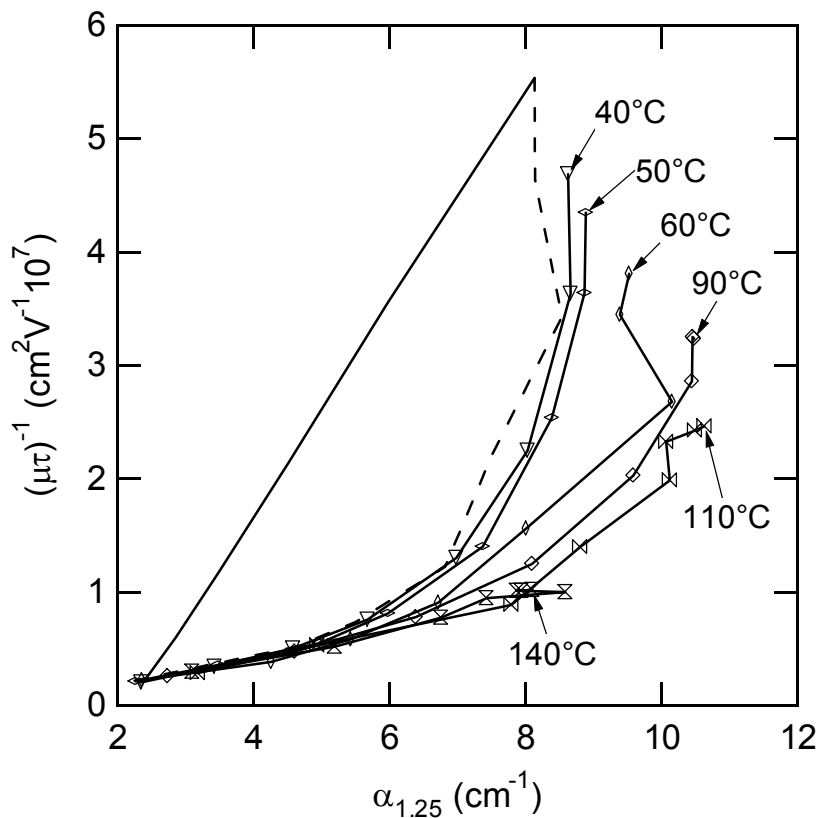


**Figure 4.29:**  $(\mu\tau)^{-1}$  versus  $\alpha_{1.25}$  for the step-wise anneals after exposure at the indicated  $T_{\text{exp}}$  for 73 min. All measurements are done at room temperature. Same symbols as in Fig. 4.24 (open instead of filled). As a reference, the data of an exposure at room temperature (full line) followed by a step-wise anneal (dashed line) are included.

to the behavior seen in Fig. 4.8:  $(\mu\tau)^{-1}$  is not a one-valued function of  $\alpha_{1.25}$ . To check this hypotheses, a very similar procedure as in Section 4.2.3. with isothermal anneals is used. After each exposure, the sample is step-wise annealed at elevated temperature. The procedure is sketched in Fig. 4.28. Fig. 4.29 shows all of the step-wise anneals after light-soaking at elevated  $T_{\text{exp}}$  together with a room T exposure and a subsequent step-wise anneal as reference. Less of the fast  $(\mu\tau)^{-1}$  anneal component remains as the samples are exposed at higher  $T_{\text{exp}}$ . After the exposure at 140°C, only the slow component remains, which decreases linearly with  $\alpha_{1.25}$ . Combined with the linear relationship between  $(\mu\tau)^{-1}$  and  $\alpha_{1.25}$  during degradation (Fig. 4.26), this means that the degradation and annealing curve lie on top of each other.

There is a second trend visible in Fig. 4.29:  $\alpha_{1.25}(73\text{min})$  grows with increasing  $T_{\text{exp}}$  up to  $T_{\text{exp}} = 110^\circ\text{C}$ , i.e. the creation efficiency of  $D^0$  grows with increasing  $T_{\text{exp}}$  in this temperature range [8]. For  $T_{\text{exp}} > 110^\circ\text{C}$ ,  $\alpha_{1.25}(73\text{min})$  decreases again, which is due to the onset of DB annealing above 110°C, and which is also visible in the shift of the saturation

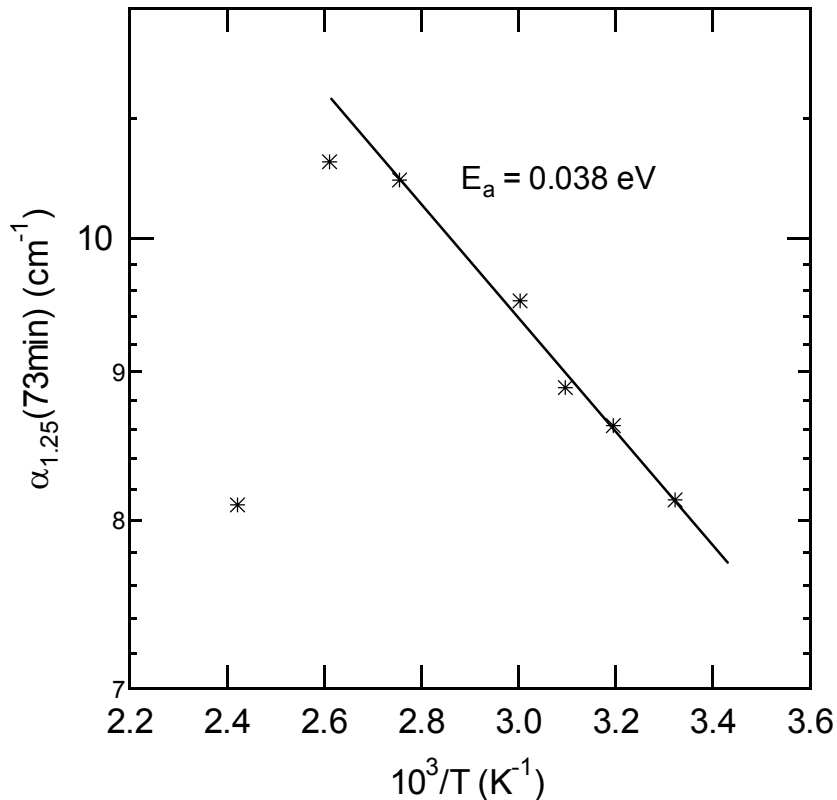


**Figure 4.30:** Arrhenius plot of  $\alpha_{1.25}(73\text{min})$  from the exposure at elevated temperature (Fig. 4.25); the line is fitted by eye.

onset to shorter times with increasing  $T_{\text{exp}}$  (Fig. 4.25). The change from the increase to the decrease of  $\alpha_{1.25}(73\text{min})$  happens at about  $110^\circ\text{C}$ , exactly when  $(\mu\tau)^{-1}$  changes from fast to slow recovery. This behavior becomes most obvious, when  $\alpha_{1.25}(73\text{min})$  is plotted in an Arrhenius plot. This is done in Fig. 4.30. A line is fitted by eye to the data for  $T_{\text{exp}} < 110^\circ\text{C}$ . The activation energy of degradation derived from this slope is 38 meV and in excellent agreement with previous measurements of the activation energy for  $D^0$  creation by light-soaking [8, 35, 92]. In this figure, the deviation from this activated behavior can now clearly be seen for  $T > 110^\circ\text{C}$ . It seems as if the reduction of the fast  $\sigma_{\text{ph}}$  annealing component is closely connected to the  $D^0$  creation during light soaking.

Fig. 4.31 is the same as Fig. 4.29, except that  $\tilde{\alpha}_{1.1}$  replaces  $\alpha_{1.25}$  on the ordinate. This figure is shown mainly for completeness. The figure demonstrates again that the fast annealing component is closely connected to the increase in  $\tilde{\alpha}_{1.1}$ .

This section showed the connection between the two annealing regimes and light-induced degradation. Light-soaking appears to be compounded of a degradation and an

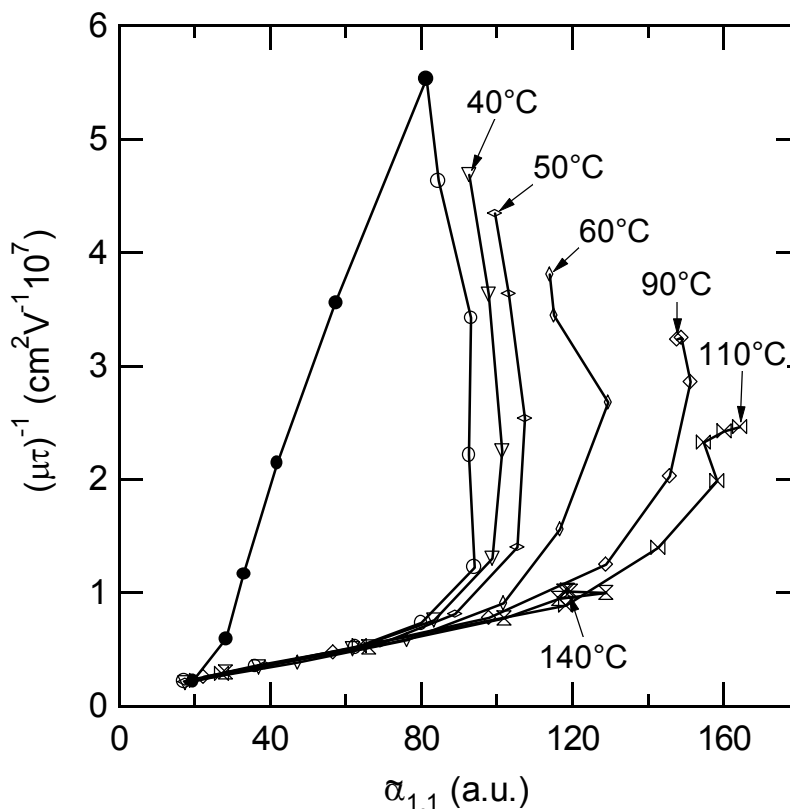


**Figure 4.29:** Same as Fig. 4.27, using  $\tilde{\alpha}_{1.1}$  instead of  $\alpha_{1.25}$ .

annealing part [37, 92]. For higher exposure temperature, the fast component anneals out easier during degradation. Nevertheless, independent of the exposure temperature, this fast annealing component of degradation is always created in fixed proportion to  $D^0$ , so that  $\sigma_{ph}$  and  $D^0$  always have a linear relationship during degradation [29]. For sufficiently high exposure temperature ( $> 110^\circ\text{C}$ ), the fast component anneals out immediately, and degradation and annealing should retrace themselves in a  $\sigma_{ph}$  versus  $D^0$  plot.



#### 4.4. Summary of results

The experimental results in this chapter are separated into exploring the dynamics of the SWE with pulsed light illumination, and into the examination of the recombination centers that are responsible for changes in  $\sigma_{\text{ph}}$ . The main results are:

- For pulse lengths equal and larger than 40  $\mu\text{s}$ , the degradation is fast enough to follow the light pulses.
- The pulsed degradation results are always affected by an annealing component.
- The upper limit for a slower precursor during degradation is 40  $\mu\text{s}$ .
- The photoconductivity is inverse proportional to the  $D^0$  density *during light-soaking*.
- During annealing, the photoconductivity is *not* dominated by  $D^0$ .
- An abrupt transition exists between *two* annealing regimes.
- Two annealing activation energies are measured. One of them is identified as the annealing of  $D^0$ .
- The absorption of the smallest energy illumination increases linearly with photoconductivity during annealing.
- Already during light-soaking, the recombination centers start to anneal.

## 5. Discussion

This section concentrates on the light-induced degradation of  $\sigma_{\text{ph}}$  (SWE) [1] and discusses how the recombination of photo-generated carriers can change during illumination and annealing of a-Si:H. The results of Chapter 4 clearly demonstrated that two components influence the light-degraded  $\sigma_{\text{ph}}$ . It was also shown that these two components have different anneal kinetics and are therefore easily distinguished only during thermal anneals of light-soaked samples. The rather abrupt transition from fast to slow annealing of the light-degraded  $\sigma_{\text{ph}}$  constrains models of degradation and annealing of recombination centers in a-Si:H.

The two major classes of models, which could explain the results of Chapter 4, are introduced in Section 5.1. They are referred to as ‘one-defect’ and ‘two-defect’ model. In the one-defect model it is assumed that neutral dangling bonds ( $D^0$ ) are the only light-induced recombination centers in a-Si:H. Two-defect models assume that there is an additional defect, which acts as an important recombination center. Based on the data of Chapter 4, it is argued that the two-defect model is more plausible. Section 5.2 analyzes in more detail the consequences of two light-induced recombination centers and demonstrates their consistency with the results in Chapter 4 and other research. The increase of  $\tilde{\alpha}_{1,1}$  and its inverse linear relationship to  $(\mu\tau)^{-1}$  during the fast annealing regime of  $\sigma_{\text{ph}}$  is a new result that was presented in Chapter 4. It is explained in Section 5.3 within the two-defect model by hypothesizing the disappearance of an effective recombination center in the upper half of the bandgap. This conclusion is supported in Section 5.4 by a model simulation of changes in  $(\mu\tau)^{-1}$ ,  $\alpha_{1,25}$ , and  $\tilde{\alpha}_{1,1}$  due to the changes in occupancy of bandgap states during light-induced degradation and thermal annealing.

### 5.1. One or two light-induced recombination centers?

In this section we discuss whether it is possible to explain the light-induced degradation and annealing of  $\sigma_{\text{ph}}$  with one single kind of recombination center, or whether the data require at least two of them. In Section 2.1, the light-induced  $\sigma_{\text{ph}}$  decrease in intrinsic a-Si:H samples was traced to a decrease in electron lifetime,  $\Delta(\tau^{-1})$ . Equ. 2.4 includes only the contributions to lifetime changes from light-induced recombination centers, with densities  $N_j^{\text{LID}}$ , and proportionality constants  $C_j^{\text{LID}}$ . Changes in  $\Delta(\tau^{-1})$  can be due to changes in  $N_j^{\text{LID}}$ ,  $C_j^{\text{LID}}$  or both. One well-established recombination center in a-Si:H is the neutral Si dangling bond ( $D^0$ ). They have states at mid-bandgap, which capture electrons long enough to enable

recombination with a hole before they are thermally reemitted to the conduction band (CB). First, we describe the consequences of assuming that  $D^0$ s are the only recombination centers present in a-Si:H; we refer to this approach as the ‘one-defect’ model. After that, we demonstrate how the data are described with the ‘two-defect’ model, with a second kind of recombination center in addition to the  $D^0$ .

### 5.1.1 One-defect model

In the one-defect model, one assumes that the neutral DB ( $D^0$ ) is the only recombination center in a-Si:H [6, 7]. This is a straightforward and common approach, because during light-induced degradation of  $\sigma_{ph}$  the density of  $D^0$  ( $N_{db}$ ) rises [3, 4] and  $\sigma_{ph}$  remains inversely proportional to the increasing  $N_{db}$  [7, 8, 29, 31]. It is worth noting that this conclusion has frequently been drawn only from light-induced degradation data [6-8]. If the  $D^0$  are the only recombination centers, then Equ. 2.4 has only one term

$$\Delta(\tau^{-1}) = C_{db} N_{db}. \quad (5.1)$$

However, the isothermal anneal data in Section 4.2.1. (e.g. Fig. 4.8) show that for nearly every  $N_{db}$  there are two  $\sigma_{ph}$  values. In the one-defect model, we must therefore either conclude 1) that  $C_{db}$  in Equ. 5.1 can take different values in different locations, resulting in a distribution of values [32, 93] correlated with anneal activation energy or 2) that  $C_{db}$  is not constant during annealing [94]. However, each approach would require additional assumptions about the  $D^0$  that have not been confirmed experimentally.

First, we examine the assumption that the  $C_{db}$  are time-independent, but have a distribution of values [93], depending on the environment of the  $D^0$  [95] and correlated to the anneal energy. The energy dissipated in the recombination event can only be released by phonons, because the recombination event via  $D^0$ s is mainly non-radiative at room temperature [95, 96]. The coupling of the DBs to the lattice could influence the efficiency of the  $D^0$  recombination [32], and this coupling might depend on the environment.

Low temperature experiments by the Fritzsche group indicate the range of annealing activation energy ( $E_a$ ) that the  $D^0$  must have to accommodate the data. After  $\sigma_{ph}$  is degraded at below 40 K, the changes begin to anneal at about 150 K [37]. That is, the  $D^0$ s must have a broad annealing activation energy ( $E_a$ ) distribution that is at least as low as about 0.2 - 0.4 eV [37, 93]. This distribution must have its maximum at about 1.2 eV as determined by the present measurements of  $\alpha_{1,25}$  during anneal (Section 4.2.2.) and by ESR measurements [8,

36]. Further, the  $D^0$ s must have capture efficiencies correlated to their  $E_a$  [33]:  $C_{db}$  must be much smaller for  $D^0$  with small  $E_a$  compared to  $C_{db}$  for  $D^0$  with high  $E_a$ . Further, the sharp transitions in the anneal data would require the  $E_a$  distribution of  $D^0$  to have two distinct regimes below and above  $E_a \approx 1.0$  eV (Section 4.2.3.). The density of  $D^0$  for  $E_a < 1.0$  eV must be relatively small, to explain why they are difficult to detect by deep defect measurements [8, 36]. At the same time, these defects must have a high recombination efficiency for electrons, to explain the fast recovery of  $\sigma_{ph}$  for anneals below  $110^\circ\text{C}$  (Fig. 4.8). The other regime covers the  $D^0$ 's with  $E_a > 1.0$  eV. It contains the majority of the  $D^0$ s, which have very small recombination efficiencies. This feature of the model would explain the slow recovery of  $\sigma_{ph}$  for anneal temperatures above  $110^\circ\text{C}$ . Thus,  $E_a \approx 1.0$  eV would separate two distinct subsets of  $N_{db}$  with respect to their recombination efficiencies. But this is the essential idea behind the two-defect model, which distinguishes two different kinds of recombination centers, even if both are DBs. Therefore, the further discussion of DBs with significantly different recombination efficiencies is continued in Section 5.1.2.

Now we discuss the possibility that  $C_{db}$  is not time-independent, but instead changes during annealing. A very general approach is that structural changes [20, 21] drastically reduce  $C_{db}$  during anneals at  $T_a < 110^\circ\text{C}$ . Some light-soaking and anneal experiments were interpreted to involve changes in the local environment of  $D^0$ s due to hydrogen rearrangements [32]. To explain abrupt transitions like in Figs. 4.10 and 4.22, these rearrangements must occur suddenly, which requires additional assumptions that are not supported by the experiment. Alternatively,  $C_{db}$  might depend on potential fluctuations. Changes of such fluctuations were inferred from the light-induced increase of the activation energy difference between dark conductivity ( $\sigma_d$ ) and thermoelectric power [97]. This result was interpreted as the light-induced increase of inhomogeneously distributed charged centers. These potential fluctuations do not change the mobility during light-induced degradation [6, 43-46], but the charged centers most likely represent alternative electron recombination paths to  $D^0$ , instead of influencing  $C_{db}$ . In this case, the observed potential fluctuation supports the two-defect model described in Section 5.1.2. If this is not the case, then the potential fluctuations must have a selective influence on the  $C_{db}$  such that  $N_{db}$  can be divided into two subsets. Similarly to the scenario in the last paragraph, the two subsets can be interpreted as two different kinds of recombination centers, which again leads to a two-defect model.

Another possibility to explain the dramatic reduction of  $C_{db}$  is that the charge state of the defects changes during light-soaking, i.e., they “recharge” and their effectiveness as recombination centers decreases. For example, if light-induced  $D^0$  defects recharge into

negatively charged DBs ( $D^-$ ) during the initial fast recovery of  $(\mu\tau)^{-1}$ ,  $C_{db}$  would decrease dramatically, because  $D^-$ s cannot trap another electron. This would effectively eliminate  $D^0$  as electron trapping centers, and  $\sigma_{ph}$  would increase [94]. The data of Fig. 4.8 would require that about 75% of  $D^0$  be transformed to  $D^-$ . However, such a large change in the paramagnetic center density during low T annealing of light-induced defects is not observed in ESR experiments. For example, Dersch et al. find a decrease in ESR signal of less than 5% during an anneal at 120°C for 30 minutes [4]. The same argument applies if one considers the possibility that light-created  $D^+$  recharge into  $D^0$  during the initial fast recovery of  $(\mu\tau)^{-1}$ . The  $D^0$  would still act as recombination centers, but  $C_{db}(D^0) \ll C_{db}(D^+)$ , and  $\sigma_{ph}$  would increase. In this case a large increase in the  $D^0$  ESR signal should be observed, in contrast to experiments [4]. Only if these two recharging schemes are combined, there is no change in the ESR signal during the initial fast recovery of  $(\mu\tau)^{-1}$ : If the same number of light-induced  $D^+$  simultaneously transform into  $D^0$  as light-induced  $D^0$  transform into  $D^-$ , then there would be no change detectable in the  $D^0$  ESR signal. The net result would be a decrease in the  $D^+$  density and an increase in the  $D^-$  density. But this scenario is excluded by combined ESR and CPM measurements, because absorption measurements like CPM excite electrons from both  $D^0$  and  $D^-$ , while ESR cannot detect the non-paramagnetic  $D^-$ . The larger  $D^-$  density during the fast annealing of  $(\mu\tau)^{-1}$  (compared to the degradation) would thus lead to a significantly different relationship between  $N_{db}$  (measured with ESR) and  $\alpha_{1.25}$  (measured with CPM) during degradation and annealing, but this is not observed [32].

Thus, the data presented here might be explained by the one-defect approach, but this would require many additional assumptions about the  $D^0$  that are not supported by other observations. The simpler assumption of two recombination centers agrees far better with the results of Chapter 4 and with other experiments.

### 5.1.2 Two-defect model

Two main arguments emerge from the data in Chapter 4, which suggest that two defects are responsible for the behavior of  $(\mu\tau)^{-1}$  during light-induced degradation and thermal annealing of a-Si:H: (1) the abrupt changes in  $(\mu\tau)^{-1}$  versus deep defect absorption (Figs. 4.10 and 4.22), and (2) the two different  $E_a$  energies for  $(\mu\tau)^{-1}$  and deep defects (Fig. 4.15, 4.17b, 4.18b, 4.19). Section 5.2 will further demonstrate the overall consistency of a two-defect model and its agreement with the data of Chapter 4 and other experiments. The possibility that there are more than two recombination centers [98] cannot be excluded. However, only

two are necessary to explain the data. If we assume two recombination centers, Equ. 2.4 becomes

$$\Delta(\tau^{-1}) = C_{db}N_{db} + C_{pr}N_{pr}. \quad (5.2)$$

This is an extension of Equ. 5.1, adding a second recombination center in addition to  $D^0$ . We call the second defect *primary recombination* centers (pr-centers), because they dominate  $\sigma_{ph}$  in light-degraded samples. In the two-defect model, each kind of defect has its unique proportionality constant, which remains constant during light-soaking and annealing. For consistency with Figs. 4.8, 4.12, and 4.13,  $C_{pr} \gg C_{db}$ . The other salient feature deduced from these figures is that the pr-centers do not show an obvious absorption signal.<sup>2</sup> The two annealing regimes can now be identified with the independent annealing of pr-centers and  $D^0$ s. The fast annealing regime is associated with the annealing of pr-centers. Because pr-centers dominate  $\sigma_{ph}$ , their  $E_a$  (0.8 – 0.9 eV) is reflected in the  $(\mu\tau)^{-1}$  annealing data (Figs. 4.15, 4.19). The slow annealing regime is dominated by the annealing of  $D^0$  (Figs. 4.22, 4.23, 4.26 and 4.29), which anneals with  $E_a \approx 1.2$  eV (Figs. 4.17 - 4.19). Section 2.1 stated that the proportionality constants can also represent different recombination paths to the same recombination center. In principle, this might be possible; the formalism to describe the changes in  $\sigma_{ph}$  with Equ. 5.2 is the same as in the two-defect model. The arguments for two distinct recombination paths and the listed properties of the pr-centers would then apply to a ‘pr-path’ instead to a pr-center. However, the description with two distinct different recombination centers appears more reasonable, because of the experimental evidence described in the next paragraph.

The pr-centers were introduced above without any microscopic model because the experiments of Chapter 4 can only make statements about the recombination of photo-induced carriers. No unambiguous statement about the microscopic realization of the entity ‘pr-center’ can be made from the results presented here. But, even though there is no direct measurement for the pr-centers, there is considerable experimental [9, 31, 35-37, 50, 87, 92, 99, 100] and theoretical [10, 91, 101-103] evidence that fits well into the picture of a second recombination center. Several authors provided evidence for the existence and the light-induced increase of states at about 0.4 eV above mid-bandgap ( $\approx 0.5$  eV from the CB) [92, 104, 105]. A detailed investigation about the effects of these states on  $\sigma_{ph}$  during light-

---

<sup>2</sup> Section 5.3 will demonstrate that the increase in  $\tilde{\alpha}_{1,1}$  can be interpreted as indirect CPM signature of pr-centers.

soaking and annealing has not been reported. However, if these light-induced states have a high capture efficiency for electrons [91], they would be good candidates for the pr-centers and might readily capture a hole to complete the recombination. Being located above mid-bandgap, they should be unoccupied in the dark and could well be positively charged [10, 35]. This would explain why these states are difficult to detect with CPM, which is only sensitive to states occupied with electrons (Section 2.2.2.). Also, unoccupied states such as positively charged DBs ( $D^+$ ) are not paramagnetic in intrinsic a-Si:H, which could explain why they are not detected by ESR. The large capture efficiency for electrons and the difficulty of detection with CPM and ESR are the salient features of pr-centers. But, even if the pr-centers do not have yet a direct microscopic signature, there is far more evidence for their existence than for variation or time-dependence of  $D^0$  capture efficiencies, which would be required to explain the experiments with one-defect models.

Even though we cannot determine the microscopic entity acting as pr-centers, it is possible to identify good microscopic candidates. One possibility are  $D^+$ s that are created during light-soaking [10] in regions of positive potential fluctuations [106]. Their different energetic location in the bandgap might be responsible for the different annealing activation energy ( $E_a$ ) compared to  $D^0$ s [106, 107]. The second possibility is positively-charged mobile hydrogen [108, 109] that is created when recombination excites H from Si-H bonds [11]. This species would be metastable in positive potential fluctuations, but during anneals below 110°C, it might escape the fluctuations and recombine with a DB.

## 5.2. Consequences of a second recombination center

This section discusses in more detail the consequences of postulating two distinct recombination centers in a-Si:H, and assuming that one of them is  $D^0$ . The consistency of a two-defect model with the data of Chapter 4 and other work is examined. For simplicity, the capture efficiencies  $C_{pr}$  and  $C_{db}$  in Equ. 5.2 are each considered constant during degradation and annealing, although they could, in principle, have a distribution of values.

One consequence of Fig. 4.9 is that the pr-centers are not directly detectable by deep defect absorption measurements. Therefore, slopes in  $(\mu\tau)^{-1}$  versus  $N_{db}$  graphs can only be used to determine  $C_{db}$  in special cases. These slopes are actually a compound of  $C_{pr}$  and  $C_{db}$  (Equ. 5.2), which becomes clear by rewriting Equ. 5.2 as

$$\Delta(\tau^{-1}) = \left( C_{db} + C_{pr} \frac{N_{pr}}{N_{db}} \right) N_{db} = (C_{db} + C_{pr} k_s) N_{db}. \quad (5.3)$$

with

$$k_s = \frac{N_{pr}}{N_{db}}. \quad (5.4)$$

For easy comparison with the measurements of  $(\mu\tau)^{-1}$  and  $\alpha_{1.25}$  that are presented in Chapter 4, Equ. 5.3 is rewritten as

$$\Delta(\mu\tau^{-1}) = \mu^{-1}(C_{db} + C_{pr}k_s)A_{CPM}\Delta\alpha_{1.25} = m\Delta\alpha_{1.25}. \quad (5.5)$$

Here,  $A_{CPM} = N_{db}/\alpha_{1.25} \approx 7.0 \times 10^{15} \text{ cm}^{-2}$  is the proportionality constant between  $N_{db}$  measured by ESR and  $\alpha_{1.25}$  measured by CPM [32]. The slope  $m$  is the proportionality constant between  $(\mu\tau)^{-1}$  and  $\alpha_{1.25}$  (slopes in Fig. 4.8, 4.12, 4.13 and Section 4.2.3) and is defined by Equ. 5.5

$$m = \mu^{-1}A_{CPM}(C_{db} + C_{pr}k_s). \quad (5.6)$$

Equ. 5.6 expresses that the slope  $m$  in  $(\mu\tau)^{-1}$  versus  $\alpha_{1.25}$  graphs are determined by the sum of the proportionality constants of the two involved recombination centers, where the relative contribution of each type of defect depends on the defect density ratio  $k_s$  (Equ. 5.4).

$C_{pr}$  and  $N_{pr}$  cannot be separately determined by the experiments presented here, only their product  $C_{pr}N_{pr}$ . For the  $D^0$ ,  $C_{db}$  can be determined, but only when the pr-centers do not influence  $\tau^{-1}$ , i.e., for those cases where  $k_s = 0$ . In this case, Equ. 5.6 becomes

$$m_{db} = \mu^{-1}A_{CPM}C_{db}. \quad (5.6a)$$

This condition is met, for example, during the slow anneal regime, after all pr-centers have annealed in the fast annealing regime (Section 4.2.3.). By comparison with Equ. 5.6, we find that this slope is always smaller by  $\mu^{-1}A_{CPM}C_{pr}k_s$  than during degradation, when pr-centers together with  $D^0$  determine  $\sigma_{ph}$ . The next sections show the limits to  $k_s$  derived from the present data and illustrate how the faster annealing of the pr-centers compared to  $D^0$  influences light-induced degradation.



### 5.2.1. Linear relationship between $(\mu\tau)^{-1}$ and $\alpha_{1.25}$

Figs. 4.8, 4.12 and 4.13 show that for one  $N_{db}$  value there are two  $\sigma_{ph}$  values [9, 30, 31, 37]. At the same time, the linearity between  $\sigma_{ph}$  and inverse spin density or deep defect absorption is a robust relationship [7, 8, 29-31, 37], which has led to the conclusion that neutral  $D^0$  are the only light-induced recombination centers in a-Si:H [7, 8]. Equ. 5.3 demonstrates that  $(\mu\tau)^{-1}$  (or the inverse of  $\sigma_{ph}$ ) can be proportional to  $N_{db}$  during degradation even though  $\sigma_{ph}$  is determined by the pr-centers. This occurs if  $k_s$  in Eqs. 5.3 - 5.6 is constant for a given sample during light soaking. That is, pr-centers and  $D^0$  must be created simultaneously and in fixed proportion during illumination. Under these circumstances  $(\mu\tau)^{-1}$  will always be linearly proportional to  $N_{db}$  even though it is determined by the pr-centers, because  $C_{pr} \gg C_{db}$  (Equ. 5.3). An estimate of  $N_{pr}/N_{db}$  during degradation is obtained by taking the ratio of Equ. 5.6 and 5.6a and substituting the expression for  $k_s$  of Equ. 5.4:

$$\frac{N_{pr}}{N_{db}} = \left( \frac{m}{m_{db}} - 1 \right) \frac{C_{db}}{C_{pr}}. \quad (5.7)$$

This expression depends on  $C_{pr}/C_{db}$ . From Fig. 4.8, the present experiments reveal  $m/m_{db} \approx 10$ .  $C_{pr}/C_{db}$  can be estimated from  $\sigma_{ph}$  models. Such models find good agreement between experiment and model only when they assume two recombination centers of significant different electron capture efficiencies. One model finds  $C_{pr}/C_{db} \approx 10$  [91, 102], and Equ. 5.7 then yields  $N_{pr} \approx N_{db}$ . This result is very sensitive to  $C_{pr}/C_{db}$ : if  $C_{pr}/C_{db} = 100$  (a typical ratio assumed for charge to neutral capture rates of defects), then  $N_{pr}$  would be ten times smaller than  $N_{db}$ .

Because of the lower  $E_a$  of the pr-centers, the difference in the influence of pr-centers on  $(\mu\tau)^{-1}$  becomes apparent in anneal experiments for long exposure times ( $t_{exp}$ ) and at elevated  $T_{exp}$  (described in the next sections). Fig. 4.12 demonstrates that  $k_s$  must be constant during degradation during the light-soaking times  $t_{exp}$  that were studied. If  $k_s$  were not constant, the subsequent annealing would differ significantly for different  $t_{exp}$ . This finding is supported by the modeling of CPM spectra of annealed and degraded samples [110]. The pr-centers and the  $D^0$  might be created in fixed proportion during degradation for several reasons. For example, if light-soaking creates recombination centers spatially randomly in the lattice and the charge state of a light-created DB depends on the local environment [106], a light-created DB could end up in different charged states [10]. The individual probabilities of creating  $D^+$ ,  $D^0$  or  $D^-$  might be different, but more important, if they remain constant during

light-soaking, then the ratio of their increasing densities would be fixed during degradation. Each charge state of the DBs would be expected to have different capture efficiencies for electrons and holes. Alternatively, if light excites H from deeply bonded Si-H sites [11], DBs and mobile H would naturally be created in equal numbers. The mobile H could be positively charged and act as pr-center.

### 5.2.2. Temperature dependence of light-induced degradation

The T dependence of  $k_s$  can be found by examining the T dependence of the degradation at elevated exposure temperature,  $T_{\text{exp}}$ . Fig. 4.26 demonstrates that  $m$ , and with it  $k_s$ , is temperature dependent, i.e.,  $k_s = k_s(T_{\text{exp}})$ . This decrease of  $k_s$  with increasing  $T_{\text{exp}}$  is a natural consequence of the lower annealing activation energy of the pr-centers compared to the  $D^0$  defects. Although pr-centers are created simultaneously with  $D^0$ , we would expect that during any light exposure at elevated  $T_{\text{exp}}$  a larger fraction of the pr-centers than of the  $D^0$  will anneal away. The  $N_{\text{pr}}$  that remains after light-soaking depends on  $T_{\text{exp}}$  and can be written as

$$N_{\text{pr}}(T_{\text{exp}}) = \int_{E_d}^{\infty} N_{\text{pr}}(E_a) dE. \quad (5.8)$$

Here  $N_{\text{pr}}(E_a)$  is the distribution of pr-center anneal activation energies. The lower limit of the integral  $E_d = kT_{\text{exp}} \ln(v_0 t_{\text{exp}})$  is the same demarcation energy introduced in Equ. 2.15 of Section 2.3. [73]. One assumes that the full range of the pr-center  $E_a$  distribution is always created during light soaking, but that all pr-centers with  $E_a < E_d$  anneal out immediately. For present experiments, this means that for fixed  $t_{\text{exp}}$ , the part of the light-induced  $N_{\text{pr}}$  (Equ. 5.8) that remains after  $t_{\text{exp}}$  decreases with  $T_{\text{exp}}$ . As the contribution of the pr-centers decreases,  $k_s(T_{\text{exp}})$  (Equ. 5.4) and  $m(T_{\text{exp}})$  (Equ. 5.6) decrease as well. This effect is seen in Fig. 4.27. Above some critical temperature, only  $D^0$  defects remain. That is,  $k_s \approx 0$ , and  $m$  approaches a constant value of  $m_{\text{db}}$  (Equ. 5.6a).<sup>3</sup> Thus, during high T creation, as during the high T annealing regime,  $k_s \approx 0$  indicates that  $(\mu\tau)^{-1}$  depends on  $D^0$  alone. Recall (Section 4.3: Figs. 4.26 and 4.29) that  $(\mu\tau)^{-1}$  depends linearly on  $D^0$  during degradation *and* annealing for  $T_{\text{exp}} \geq 140^\circ\text{C}$ .

The previous paragraph already indicated that the slopes  $m(T_{\text{exp}})$  contain information about the  $E_a$  distribution of the pr-centers. This can be seen by inserting the expression for

<sup>3</sup> A necessary condition for this conclusion is that few  $D^0$  anneal out during light-soaking. The observed linear relationship between  $(\mu\tau)^{-1}$  and  $N_{\text{db}}$  during light soaking (Fig. 4.26) support this assumption.

$N_{pr}$  (Equ. 5.8) into Equ. 5.4 and the resulting equation into Equ. 5.6. This manipulation shows that  $m$  depends on  $E_a$ ; taking the derivative of  $m(E_a)$  with respect to  $E_d$  leads to

$$\frac{dm(E_a)}{dE_d} = -\frac{A_{CPM}C_{pr}}{\mu N_{db}} N_{pr}(E_d), \quad (5.9)$$

an expression for the  $E_a$  distribution of the pr-centers, which can be compared to the isothermal annealing results (Figs. 4.15 and 4.19a). To this end,  $T_{exp}$  in Fig. 4.27 is converted into  $E_d = kT_{exp} \ln(v_0 t_{exp})$  using the Meyer-Neldel  $v_0$  values discovered in the anneal experiments (Fig. 4.16). Next, the derivative of  $m(E_a)$  is taken with respect to this  $E_d$  and is plotted versus  $E_d$  in Fig. 5.1. Based on Equ. 5.9, this figure should display the  $E_a$  distribution of the pr-centers. The fact that the distribution is not zero for  $E_a < 0.7$  eV agrees well with the conclusions from the annealing of pr-centers created at low  $T$ , which suggested that  $N_{pr}(E_a)$  has a lower  $E_a$  limit of about 0.2 eV. However, the data does not agree with the

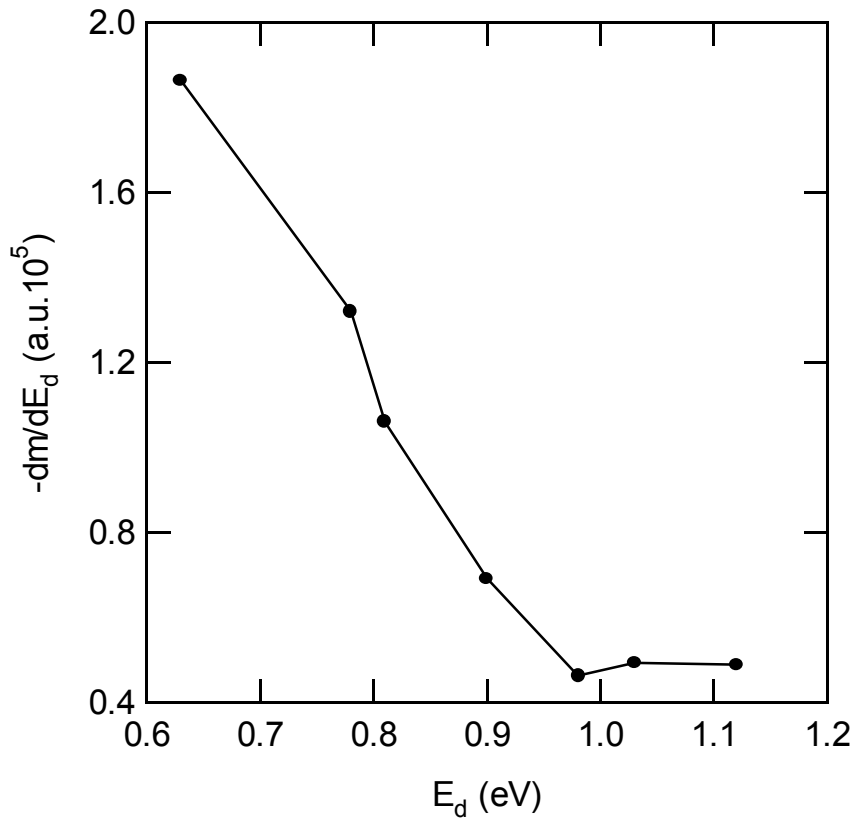


**Figure 5.1:** Negative derivative of the data in Fig. 4.27 with respect to  $E_d$  plotted vs.  $E_d$

$N_{pr}(E_a)$  found from the isothermal anneal data (Figs. 4.15b and 4.19a). There,  $N_{pr}(E_a)$  is close to zero for  $E_a < 0.7$  eV. This is not surprising, because in the isothermal anneal experiments pr-centers below 0.7 eV have most likely annealed already between light-soaking and the beginning of the measurements. Nevertheless, Figs. 5.1, Figs. 4.15 and 4.19a agree rather well in one common feature:  $N_{pr}(E_a) \approx 0$  for  $E_a > 1$  eV, where the  $D^0$  are expected to anneal. Thus, the data of the degradation experiments agree rather well with the findings deduced from the isothermal anneal experiments.

### 5.2.3. Annealing of pr-centers

An important property of pr-center is  $C_{pr} \gg C_{pr}$ , i.e., the pr-centers dominate  $\sigma_{ph}$ . This dominance is the reason why the data in Figs. 4.15 and 4.19a can be interpreted as the  $E_a$  distribution of pr-centers,  $N_{pr}(E_a)$ . This paragraph will show that  $N_{pr}(E_a)$  is created during light-soaking with a much broader width. It will be argued that only the high  $E_a$  part of  $N_{pr}(E_a)$  is left, which does not anneal during light-soaking. The low energy limit of  $N_{pr}(E_a)$  can be obtained by analysis of the results of Stradins et al. [37]. The authors found a much higher degradation of  $\sigma_{ph}$  at  $T_{exp} = 4.2$  K than at room T. The dramatic recovery of  $\sigma_{ph}$  with annealing, without the simultaneous recovery of  $D^0$  [37], suggests that a high density of pr-centers is created during 4.2 K illumination. It cannot anneal out during degradation, because  $T_{exp}$  is too low. During subsequent step-wise anneals, the degraded  $\sigma_{ph}$  starts to anneal out at about 150 K. This marks the beginning of the pr-center annealing. Equ. 5.6 and 5.8 suggests that  $m = \text{constant}$  for  $T_{exp}$  up to 150 K, and it would lead to  $N_{pr}(E_a) = 0$  from Equ. 5.9. The beginning of the recovery at this temperature then allows an estimation of the low  $E_a$  limit of the pr-center  $E_a$  distribution. With the definition of  $E_d$ , and  $t_a = 10$  min and  $v_0 \approx 10^4$  s<sup>-1</sup> found by extrapolation the data in Fig. 4.16, this lower limit of  $E_a$  can be estimated to about 0.2 eV. During subsequent step-wise annealing at higher  $T_{exp}$ ,  $\sigma_{ph}$  recovers dramatically. Inspection of the Stradins et al. data [37] shows a broad maximum of  $\sigma_{ph}$  recovery at  $T_a \approx 250 - 300$  K. This corresponds to an  $E_a$  of about 0.5 – 0.6 eV. This low temperature range was not accessible in the present work. Therefore, only the  $N_{pr}(E_a)$  for  $E_a$  greater than about 0.6 eV is measurable (Figs. 4.15, 4.19a and 5.1).

### 5.2.4. Change in $(\mu\tau)^{-1}$ degradation for long exposure times

When  $k_s = 0$ ,  $(\mu\tau)^{-1}$  depends on  $D^0$  only. As mentioned above, this is the case both for the high T regime of “slow annealing” and for the light exposure above some critical temperature; in both cases  $k_s = 0$ , because  $N_{pr} = 0$ . There is, however, a situation where  $N_{pr} \neq 0$  and  $\Delta(\mu\tau)^{-1}$  should depend on  $D^0$  only. After a certain exposure time,  $t_{exp}$ , the creation

of pr-centers will be in balance with its thermal annealing, and  $N_{pr}$  saturates. Because the pr-centers have a lower  $E_a$  than the  $D^0$ ,  $N_{pr}$  should saturate long before  $N_{db}$  saturates. This expectation is supported by the experiment: after a certain exposure time  $t_{exp}^{tr}$ ,  $(\mu\tau)^{-1}$  saturates, while  $N_{db}$  keeps growing [51, 91]. Only at much longer  $t_{exp}$  will the  $D^0$  creation be balanced by its thermal annealing and  $N_{db}$  saturates, so that the light-induced effects will be completely saturated. For  $t_{exp} > t_{exp}^{tr}$ , but before  $N_{db}$  has saturated, only the  $D^0$ s are responsible for changes in  $\sigma_{ph}$ . These conclusions are corroborated by degradation experiments of standard and hydrogen-diluted PECVD samples at different exposure temperatures,  $T_{exp}$ . In a  $(\mu\tau)^{-1}$  versus  $\alpha_{1,2}$  plot, the slopes  $m$  suddenly decreases in each case at a  $t_{exp}^{tr}$ , which depends on  $T_{exp}$  and the kind of sample [51]. It is important that in all cases the slopes change to similar values,  $1.5 - 2.5 \times 10^6 \text{ Vcm}^{-1}$ . Moreover, these values are in reasonable agreement with the slopes found during slow anneal of light-degraded  $(\mu\tau)^{-1}$  (Figs. 4.12 and 4.13) and exposure at  $T_{exp} = 140^\circ\text{C}$  (Figs. 4.26 and 4.29), namely  $2 - 6 \times 10^6 \text{ Vcm}^{-1}$ . The following conclusions can be drawn from these results: 1) For  $t_{exp} < t_{exp}^{tr}$ ,  $\sigma_{ph}$  is dominated by pr-centers until the pr-centers reach equilibrium at  $t_{exp}^{tr}$ . 2) For  $t_{exp} > t_{exp}^{tr}$ ,  $\sigma_{ph}$  is determined by one kind of recombination center, which we identify with  $D^0$ . 3) The  $D^0$  are the common recombination centers for all samples in these experiments. Further, the high limit of the  $E_a$  pr-distribution can be corroborated again, this time using  $t_{exp}^{tr}$ . This is possible, because the first light-created pr-centers start to anneal at  $t_{exp}^{tr}$ . Using  $kT_{exp}\ln(v_0 t_{exp}^{tr})$ ,  $t_{exp}^{tr} \approx 30$  hours and  $T_{exp} = 75^\circ\text{C}$  for standard PECVD samples [51, 91], we obtain about 0.9 eV, which is in good agreement with Figs. 4.15b, 4.19a and 5.1. The hydrogen-diluted sample shows an interesting feature: in the same kind of exposure experiment,  $t_{exp}^{tr}$  is significant smaller than for the standard PECVD samples [51]. The calculation yields a high limit of the  $E_a$  pr-center distribution of about 0.75 eV. This might be connected to the reduced light-induced degradation of hydrogen-diluted samples compared to standard PECVD samples (Fig. 4.13)[51].

We showed in this section how  $(\mu\tau)^{-1}$  can be dominated by pr-centers, but still appear to be inversely proportional to  $N_{db}$  during certain regimes of light-induced degradation and annealing. Standard and hydrogen-diluted samples degrade differently (Fig. 4.13 and 4.14); nevertheless, all of them have  $D^0$ s as recombination centers. The commonly studied saturation of  $\sigma_{ph}$  during light-soaking at room temperature is only the saturation of the pr-centers. The saturation of degradation is not completed until much longer  $t_{exp}$ , when  $D^0$  creation is in balance with their annealing.

### 5.3. $\tilde{\alpha}_{1.1}$ during degradation and annealing

The increase of  $\tilde{\alpha}_{1.1}$  during the fast annealing regime of  $\sigma_{\text{ph}}$  is unexpected, because it appears to indicate an increase in deep defect density. Of course, defect densities normally decrease during a-Si:H annealing after light soaking. This section describes how this increase and its inverse linear relationship to  $(\mu\tau)^{-1}$  can be explained within the two-defect model.

In Section 2.2.2., the measurement of deep defect absorption by the constant photocurrent method (CPM) was described. In this section it was emphasized that CPM is based on transitions of electrons from occupied states into the conduction band (CB), i.e., the defect densities themselves are not measured directly. A correlation to the defect density is possible only if the occupancy of the defects is always (at least approximately) constant. Tracing changes in the occupancy of the defect states during annealing is the key to understand the counter-intuitive increase in  $\tilde{\alpha}_{1.1}$ . The measurement of  $\sigma_{\text{ph}}$  and defect absorption requires the illumination of the sample, which causes a redistribution of electrons in the localized states in the band gap. In Section 2.3.2., the Simmons and Taylor statistics were briefly introduced to illustrate how the occupancy of states can be described with a modified Fermi function ( $0 \leq f \leq 1$ ) and by the definition of electron and hole quasi-Fermi levels [60]. The splitting of the quasi-Fermi levels, defined as the energetic distance between electron and hole quasi-Fermi levels, becomes wider as the densities of free electrons and holes increases. These densities are smaller after light-induced degradation, because there are more recombination centers present in the material than in the annealed state. As a consequence, the quasi-Fermi level splitting becomes smaller with degradation. When the sample is annealed, the pr-centers anneal out first because of their lower  $E_a$ . Nearly all pr-centers should have annealed out in a step-wise anneal experiment after heating the light-exposed sample to 110°C (Fig. 4.10). The increase of  $\sigma_{\text{ph}}$  indicates a rise in the electron quasi-Fermi level. This increases the occupation of unannealed states in the bandgap and is most pronounced for the deep defects. As a result, their CPM signal grows.

The 1.25 eV photon energy for the measurements of the  $D^0$  density is chosen so that all electrons occupying the  $D^0$  are excited to the CB. As expected, Fig. 4.8 does show a small increase in  $\alpha_{1.25}$  when the light-soaked sample is annealed at  $T_a = 70^\circ\text{C}$ . This must be interpreted as an increase in occupancy, because at 70°C,  $N_{\text{db}}$  would be quite constant or perhaps anneal slightly. Of course, this occupation-induced increase in  $\alpha_{1.25}$  during step-wise anneals is small (about 10%) compared to the absolute degraded  $\alpha_{1.25}$  value. The following will show that this relative increase is the essential difference of the  $\tilde{\alpha}_{1.1}$  compared to the  $\alpha_{1.25}$  measurement. In contrast to the 1.25 eV photons for  $\alpha_{1.25}$ , the  $h\nu \leq 1.1$  eV photons in the  $\tilde{\alpha}_{1.1}$

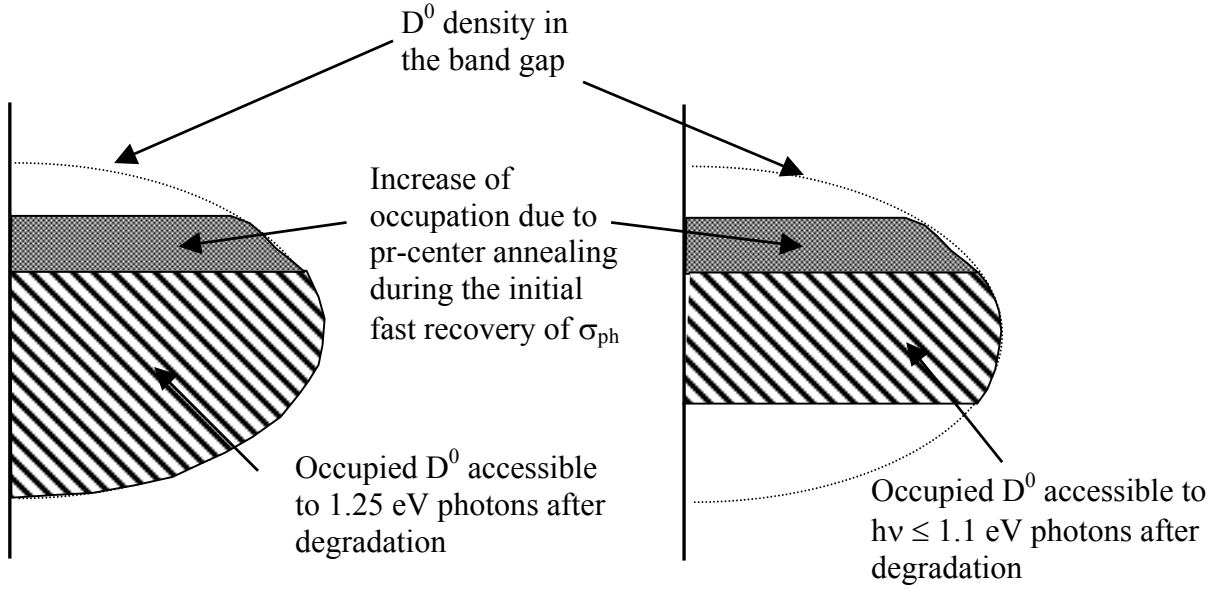


**Figure 5.2:** Schematic of the increase in accessible occupied  $D^0$  for  $\tilde{\alpha}_{1.1}$  and  $\alpha_{1.25}$  CPM measurements after degradation and after the pr-centers have annealed. The ratio of the gray to the hatched area represents the increase of the absorption measurements during the initial fast annealing of  $(\mu\tau)^{-1}$ .

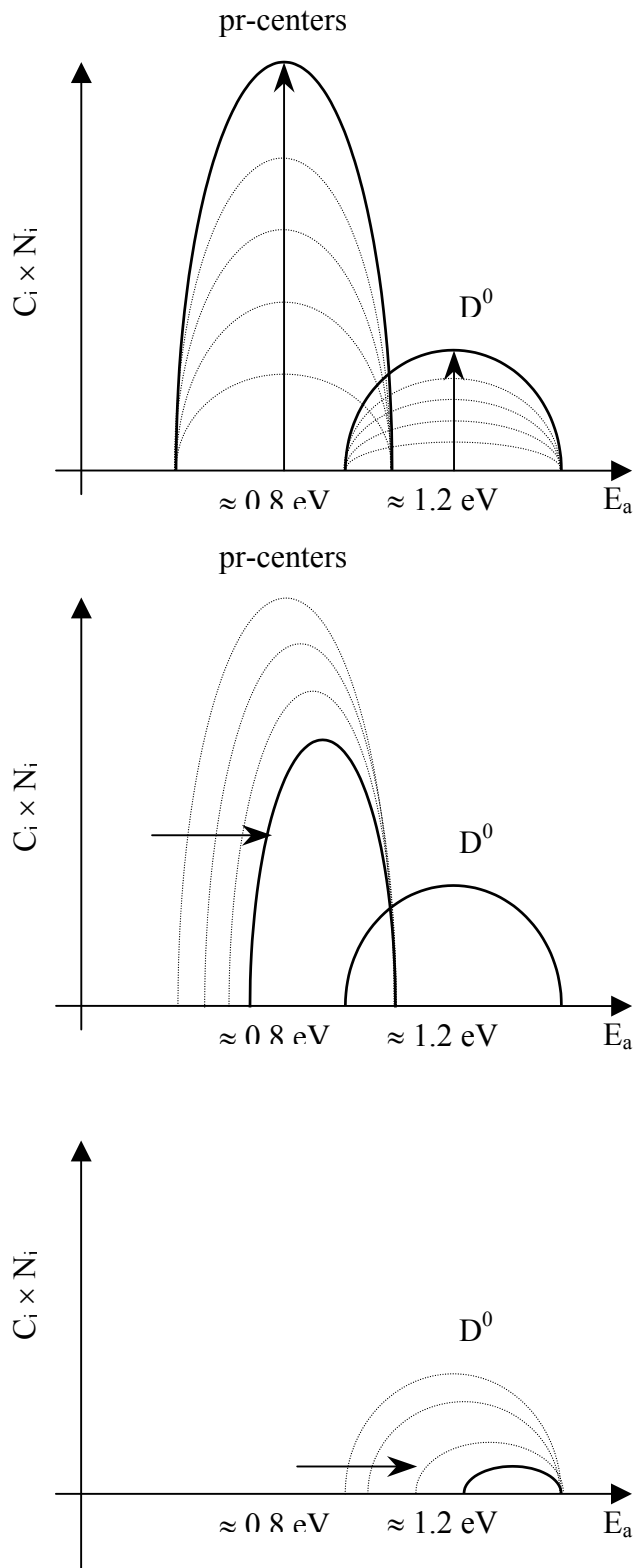
measurement excite electrons from only part of the occupied  $D^0$  distribution. The *absolute* increase in  $D^0$  occupancy is accessible to both the  $\alpha_{1.25}$  and the  $\tilde{\alpha}_{1.1}$  measurement. Therefore the *relative* increase compared to the degraded state is much larger for  $\tilde{\alpha}_{1.1}$  compared to  $\alpha_{1.25}$ . This occupation-induced effect is sketched and compared for  $\alpha_{1.25}$  and the  $\tilde{\alpha}_{1.1}$  in Fig. 5.2. It explains why during step-wise annealing in the fast  $(\mu\tau)^{-1}$  annealing regime the increase of  $\alpha_{1.25}$  (Figs. 4.8 and 4.10) is enhanced in the  $\tilde{\alpha}_{1.1}$  data (Figs. 4.13 and 4.14). The occupation-induced increase in  $\tilde{\alpha}_{1.1}$  is also clearly seen in the isothermal anneal data (Fig. 4.18a) and shows up as negative derivative (Figs. 4.18b and 4.19c). This is due to the algorithm used to find the  $E_a$  distributions: A decrease in absorption appears as positive derivative, an increase as negative derivative. The occupation-induced increase in  $\alpha_{1.25}$  cannot be identified (Figs. 4.17 and 4.19b) because of the noise. Remarkably, Sample E shows an increase during step-wise annealing by over 50% even for  $\alpha_{1.25}$ . In the framework of the proposed quasi-Fermi shift mechanism this could be explained by a larger energetic distance between the  $D^0$  states and the CB. As the annealing continues, the  $D^0$  begin to anneal.  $N_{db}$  will decrease and overwhelm the occupation-induced increase of the absorption. From this point on,  $\tilde{\alpha}_{1.1}$  and  $\alpha_{1.25}$  decrease at linearly proportional rates (Fig. 4.9) and  $(\mu\tau)^{-1}$  (Figs. 4.8, 4.10 and 4.12) is also changing linearly with the absorptions. The opposing effects of occupation-induced

increase and  $D^0$ -anneal decrease of the  $\alpha_{1.25}$  absorption is most likely the reason why the  $(\mu\tau)^{-1}$  versus  $\alpha_{1.25}$  data in Fig. 4.9 does not exhibit a sharp corner: the relatively small increase in  $\alpha_{1.25}$  is gradually compensated by the beginning of  $D^0$  annealing. For the same reason, the minimum of the  $\tilde{\alpha}_{1.1}(E_a)$  distribution, Figs. 4.18 and 4.19c, is shifted to lower values compared to the  $(\mu\tau)^{-1}(E_a)$  maximum in Figs. 4.15 and 4.19a, respectively. If both effects, the occupation-induced increase and the  $D^0$ -anneal decrease of  $\tilde{\alpha}_{1.1}$ , would influence the changes in  $\tilde{\alpha}_{1.1}$  equally, then the  $\tilde{\alpha}_{1.1}(E_a)$  distribution would be zero exactly between the  $E_a$  distribution maxima of pr-centers (0.9 eV) and  $D^0$  (1.2 eV). However, because the  $D^0$ -annealing dominates the absorption measurements,  $\tilde{\alpha}_{1.1}(E_a) = 0$  is closer to the  $E_a$  distribution maxima of the pr-center. The occupation-induced changes explain why we associated the initial increase of the degraded  $\tilde{\alpha}_{1.1}$  to the annealing of an effective recombination center. Because  $\tilde{\alpha}_{1.1}$  increases simultaneously with  $\sigma_{ph}$  (Figs. 4.10 and 4.14) [37], the significant decrease in electron recombination is the simplest self-consistent model to explain the increase of  $\tilde{\alpha}_{1.1}$  during annealing.

An increase in absorption for  $h\nu \leq 1.1$  eV photons has been previously observed only in low  $T_{exp}$  experiments as the sample is step-wise annealed after light soaking at 4.2 K [37, 38]. The authors suggest that this increase is caused by a relative shift of the deep defect levels in the bandgap closer to the conduction band edge. However, it seems much more straightforward to assume an increase in occupancy of the deep defects than to postulate an additional defect relaxation process. Especially, because these significant increase in absorption for  $h\nu \leq 1.1$  eV is always accompanied by the simultaneous dramatic recovery of  $\sigma_{ph}$  [37], which indicates an increase in charge carriers and an increase of the quasi-Fermi level splitting in the material.

This section is concluded with the remark that the existence of two recombination centers and their changing densities creates a complex picture of the occupancies of states in the bandgap. As stated in Section 2.2.1., each kind of state in the gap must be considered separately. For example, Fig. 4.8 demonstrates that  $\sigma_{ph}$  of the 110°C anneal data point can also be reached by light-soaking at much lower  $N_{db}$ . The occupancy of pr-centers and  $D^0$ , however, will obviously be very different. It is conceivable that these changes in occupancy are responsible for the observed change of the transport path with light soaking in modulated photocurrent [111] and potential fluctuation [97] experiments.





(a) Light-induced degradation:

The arrows indicate that pr-centers and  $D^0$  are created in fixed proportion.

$\sigma_{ph}$  is inversely proportional to  $N_{db}$ , but dominated by the pr-centers.

(b) Initial fast annealing of  $(\mu\tau)^{-1}$ :

pr-centers anneal and  $\sigma_{ph}$  recovers dramatically,  $N_{db}$  remains constant.

(c) Slow annealing of  $(\mu\tau)^{-1}$ :

The remainder of the  $\sigma_{ph}$  decrease anneals out and depends inversely on  $N_{db}$ .

**Figure 5.3:** Schematic of the three regimes responsible for the changes in  $\sigma_{ph}$ : (a) light-induced degradation, (b) initial fast annealing of  $(\mu\tau)^{-1}$ , and (c) slow  $(\mu\tau)^{-1}$  annealing. The products of the defect densities and their capture efficiencies are plotted against the annealing activation energy ( $E_a$ ).

### 5.4. Simulation

To verify that the occupation-induced changes in  $\tilde{\alpha}_{1,1}$  proposed in Section 5.3 are reasonable, this section shows the results of a simplified simulation of the processes responsible for the changes in  $(\mu\tau)^{-1}$ ,  $\alpha_{1,25}$  and  $\tilde{\alpha}_{1,1}$  during light-induced degradation and thermal annealing. The simulations are based on the two-defect model and a simplified increase and decrease of defect densities, which is sketched in Fig. 5.3. The products of densities and capture efficiencies for each kind of recombination center are plotted on the abscissa. These products represent the effect that the pr-centers and the  $D^0$ s have on  $\sigma_{ph}$ . The simulation uses the simple density of states (DOS) distribution (Fig. 2.2) and the Simmons and Taylor statistics [60] described in Section 2.2.1. The pr-centers are accounted for by a Gaussian function of the same width as the  $D^0$ , with its maximum at 0.5 eV from the CB. The absorption for  $\alpha_{1,25}$  is calculated by Equ. 2.11, and  $\tilde{\alpha}_{1,1}$  by integrating the absorption coefficients ( $\alpha_{hv}$ ) for photon energies  $h\nu \leq 1.1$  eV

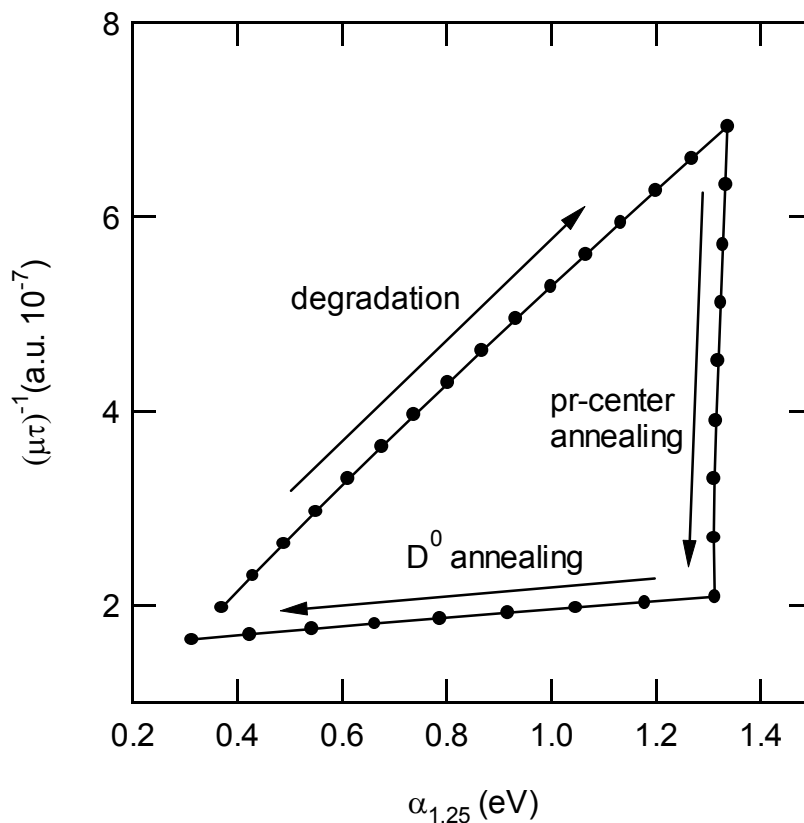


**Figure 5.4:** Simulation of the degradation and annealing behavior of  $(\mu\tau)^{-1}$  and  $\alpha_{1,25}$ .

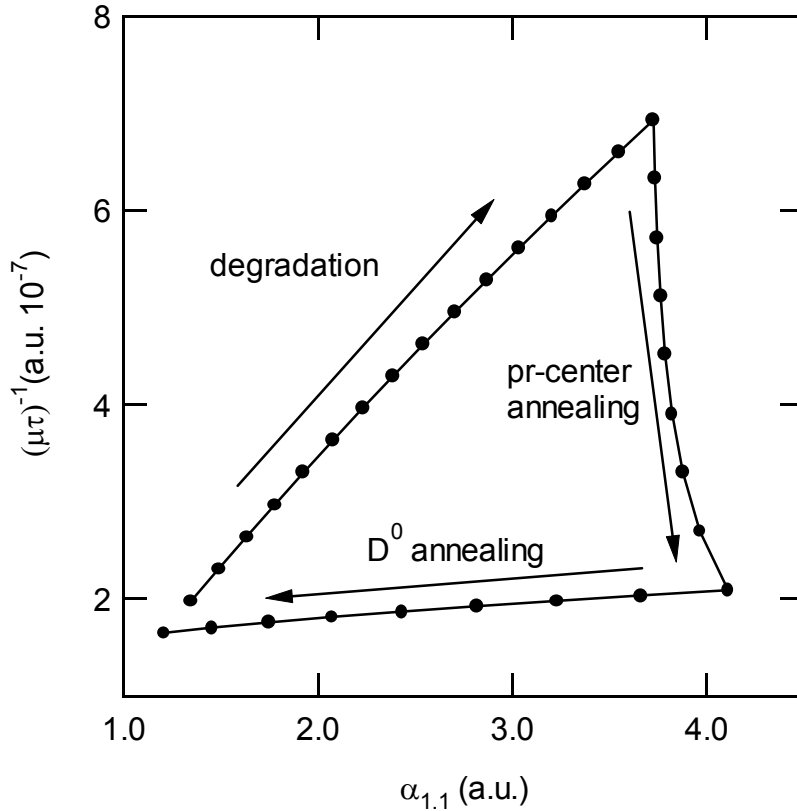


**Figure 5.5:** Simulation of the degradation and annealing behavior of  $(\mu\tau)^{-1}$  and  $\tilde{\alpha}_{1,1}$ .

$$\tilde{\alpha}_{1,1} = \int_0^{1.1eV} \alpha_{hv} dh\nu . \quad (5.11)$$

The constants used are  $C_{db} = 3 \times 10^{-10} \text{ cm}^5 \text{ s}^{-2} \text{ V}^{-1}$  (Section 4.2.3.) and  $C_{pr} = 10 \times C_{db}$  [91, 102]. This accounts for the higher recombination rate through the pr-centers. The electron-hole capture efficiency ratios are assumed to be  $r(\text{DB}) = 0.1$  and  $r(\text{pr-centers}) = 10$ , and the light-induced generation rate of electron-hole pairs is set to  $G = 10^{14} \text{ cm}^{-3}$ . The light-induced creation of pr-centers and  $D^0$ s in fixed proportion (Fig. 5.3a) is implemented by simultaneously incrementing  $N_{pr}$  and  $N_{db}$  in 16 steps of  $10^{15} \text{ cm}^{-3}$ .  $(\mu\tau)^{-1}$  (in arbitrary units),  $\alpha_{1,25}$  and  $\tilde{\alpha}_{1,1}$  are calculated after each step. The annealing is implemented in two steps. First the density of pr-centers is reduced in 8 steps to the annealed value (Fig. 5.3b) to represent the slow  $\sigma_{ph}$  annealing regime. Then the  $D^0$  density is reduced in 8 steps to the annealed value to simulate the slow  $\sigma_{ph}$  annealing regime (Fig. 5.3c).

Figs. 5.4 and 5.5 show the result of these simulations. Despite the simplicity of the model, the qualitative agreement with the data in Figs. 4.8 and 4.10 is good. In both figures,  $(\mu\tau)^{-1}$  is linearly proportional to  $\alpha_{1.25}$  and  $\tilde{\alpha}_{1.1}$  during degradation, as  $N_{\text{pr}}$  and  $N_{\text{db}}$  rise in fixed proportion. In Fig. 5.4,  $(\mu\tau)^{-1}$  recovers dramatically due to the annealing of the pr-centers, without significant changes in  $\alpha_{1.25}$ . That is, the simulation confirms that the occupation of the pr-centers is small enough that they are not visible in the  $\alpha_{1.25}$  CPM measurements, but nevertheless have a significant influence on  $(\mu\tau)^{-1}$ . The calculated data in 5.4 shows a more abrupt transition to the slow annealing regime than is observed in Fig. 4.8. This is due to the time-separation of the decrease of pr-centers and of the  $D^0$  in the calculation. In reality, the  $E_a$  distribution of these defects overlap, and  $D^0$  annealing will begin before pr-center annealing has ended. Fig. 5.5 dramatically shows that  $\tilde{\alpha}_{1.1}$  can indeed increase due to changes in  $D^0$  occupancy, thereby confirming that the occupation-induced model of the absorption increase is reasonable.

## 5.5. Summary and Conclusions

Amorphous silicon is an important material for applications like solar cells and flat panel displays, because it can be deposited cheaply on large areas. However, the metastable degradation of photoconductivity ( $\sigma_{\text{ph}}$ ) under carrier injection and illumination (the Staebler-Wronski effect) prevents its widespread application. The research efforts dealing with the Staebler-Wronski effect focus on the created metastable defects. These are considered the origin of the light- or injection-induced changes in  $\sigma_{\text{ph}}$ . The creation mechanism and the influence of these defects on  $\sigma_{\text{ph}}$  are not fully understood, which hinders the mitigation or elimination of the deleterious effects of the Staebler-Wronski effect. This thesis has utilized  $\sigma_{\text{ph}}$  measurements to reexamine the defect creation mechanism and the influence of light-induced defects on  $\sigma_{\text{ph}}$ : 1) Degradation by pulsed illumination limited the timescale for the degradation caused by electron-hole recombination. 2) Combined degradation and anneal experiments established that more than one recombination defect or pathway is created by degradation. 3) Experimental methods are established that allow to separately study each of the recombination defects or pathways.

The first part of the work deals with the timescales of degradation. These can be investigated, for example, by high intensity pulsed laser degradation. The results of these and other experiments could not be explained by electron-hole recombination alone. It was suggested that there is a precursor to degradation other than electron-hole recombination, for example, mobile hydrogen or structural changes. By comparing  $\sigma_{\text{ph}}$  degradation with continuous (CW) and pulsed illumination, the suggestion of a precursor to degradation that is slower than electron-hole recombination was tested for the first time. The shortest reasonable pulse lengths are determined by the intensity dependent  $\sigma_{\text{ph}}$  response to the light pulses. No differences that could be accounted for by the rise-time of a slow precursor were found. Nevertheless, by combining the results of different pulsed degradation experiments, limits for the time constants of a slow precursor could be established. The experiments thus show that any degradation process slower than the electron-hole recombination dynamics must still be faster than 40  $\mu\text{s}$ . Later work confirmed this result, but found a timescale in the microsecond range [Stradins, 2000 #172].

The second part of this work dealt with the metastable changes of charged carrier recombination. We compared  $\sigma_{\text{ph}}$  and defect densities ( $N_{\text{db}}$ ) during light-induced degradation and thermal annealing. The inverse proportionality between  $\sigma_{\text{ph}}$  and  $N_{\text{db}}$  during illumination was established as a robust relationship. During step-wise isochronal and isothermal anneal

experiments, however, a fast and a slow anneal component of the light-degraded  $\sigma_{\text{ph}}$  was identified. This fast annealing component is of vital importance for the understanding of metastability in a-Si:H. To better understand this phenomenon, a more complete study of the low (20 - 140°C) temperature annealing of photoconductivity degradation was undertaken. The step-wise and isothermal annealing experiments strongly suggest that a recombination center other than  $D^0$  is the origin of this fast annealing component. This recombination center dominates  $\sigma_{\text{ph}}$  and was named the primary recombination (pr) center. These pr-centers cannot be detected directly by either ESR or optical defect absorption measurements. The annealing activation energy ( $E_a$ ) distribution was determined and found to have a maximum at about 0.85 eV. However, it must be concluded from low temperature experiments that the pr-centers are created with a much wider  $E_a$  distribution reaching to at least 0.2 eV and with a maximum at about 0.6 eV. In contrast, the measured  $E_a$  distribution of the  $D^0$  agrees well with the data found in the literature. It is about 0.3 eV higher than the value found for the pr-centers for the room temperature illumination experiments. Good candidates for the microscopic entity of the pr-centers might be positively charged dangling bonds or positively charged mobile hydrogen, which could have states in the upper half of the a-Si:H bandgap. The existence and creation of states above mid-bandgap have been suggested and measured previously, though their connection to low-T annealing of photoconductivity was not examined.

The apparent contradiction that during light-soaking (but not during annealing)  $\sigma_{\text{ph}}$  appears to be inversely proportional to  $N_{\text{db}}$  is solved by the following picture of the light-induced degradation and annealing-induced recovery. During light soaking the pr-centers and the  $D^0$  are created simultaneously and in fixed proportion. Thus,  $\sigma_{\text{ph}}$  shows an inverse dependency on  $N_{\text{db}}$ , although it is actually controlled by the pr-centers. During annealing the pr-centers anneal out first because of their smaller  $E_a$ , and  $\sigma_{\text{ph}}$  recovers dramatically. A side effect of this dramatically reduced electron recombination is the increase of  $D^0$  occupancy in the bandgap, which appears as increase in the defect absorption below 1.1 eV. Only higher T (> 110°C) annealing removes the  $D^0$ . During this phase  $\sigma_{\text{ph}} \propto N_{\text{db}}^{-1}$ , this time because the  $D^0$  are the only remaining recombination centers. The clear transition between pr-center and  $D^0$  annealing is observed for the first time. This scenario solves the apparent contradiction that  $\sigma_{\text{ph}} \propto N_{\text{db}}^{-1}$  during light-induced degradation and the observation of two  $\sigma_{\text{ph}}$  values for one  $N_{\text{db}}$ .

Numerous experiments in the literature can be understood with this idea of the light-induced creation of a second recombination center besides  $D^0$ . For example, the fast

annealing of the pr-centers can be traced to the very effective light-induced  $\sigma_{\text{ph}}$  degradation at low temperatures and can be connected to light-soaking at temperatures above 20 °C. At degradation temperatures above about 110 °C, the pr-centers anneal so fast that only  $D^0$  remain, and  $\sigma_{\text{ph}}$  depends on  $N_{\text{db}}$  alone. For any degradation temperature below about 110°C,  $\sigma_{\text{ph}}$  will be dominated by pr-centers. Another situation where  $\sigma_{\text{ph}}$  is inversely proportional to  $N_{\text{db}}$  are very long exposure times. It is commonly observed that  $\sigma_{\text{ph}}$  degradation saturates before  $N_{\text{db}}$ . This is a consequence of the smaller  $E_a$  of the pr-center (which dominate  $\sigma_{\text{ph}}$ ) compared to  $D^0$ . The light-induced increase in pr-centers will equilibrate with its thermal annealing much earlier than the  $D^0$ . Further light-soaking increases  $N_{\text{db}}$ , which saturate at even longer times.

The two  $\sigma_{\text{ph}}$  annealing regimes are observed in different kinds of samples. Differences in the details of the degradation and annealing behavior of  $\sigma_{\text{ph}}$  can be explained by the amount of pr-centers created simultaneously with  $D^0$  during light-soaking. It appears that the capacity for pr-center creation depends on the deposition technique, e.g. hydrogen-diluted PECVD or HWCVD a-Si:H. The experiments with these samples demonstrated how combined degradation and annealing experiments can be used to characterize samples and determine the suitability for solar cell and other applications. On more general terms, this investigation clearly shows that any research that examines the relationship between  $\sigma_{\text{ph}}$  and light-induced recombination centers must clearly distinguish the effect of pr-centers and  $D^0$  on  $\sigma_{\text{ph}}$ . The experiments in this thesis demonstrated how this can be achieved, for example, by isochronal and isothermal anneals.

## References

1. Staebler, D.L. and Wronski, C.R., Appl. Phys. Lett., 1977. **31**: p. 292.
2. See, e.g., *Aniversary of the Staebler-Wronski Effect in Amorphous and Microcrystalline Silicon Technology-1997*, **467** edited by E.A. Schiff, M. Hack, S. Wagner, R. Schropp, I. Shimizu (Materials Research Society, Pittsburgh, 1997).
3. Hirabayashi, I., Morigaki, K., and Nitta, S., Jpn. J. Appl. Phys., 1980. **19**(7): p. L357.
4. Dersch, H., Stuke, J., and Beichler, J., Appl. Phys. Lett., 1981. **38**(6): p. 456.
5. Heck, S. and Branz, H.M. in *Amorphous and Heterogeneous Silicon Thin Films - 2000*, **609**, A3.2.
6. Street, R.A., Appl. Phys. Lett., 1983. **42**(6): p. 507.
7. Kida, H., Yamagishi, H., Kamada, T., Okamoto, H., and Hamakawa, Y. in *Technical Digest of the International PVSEC-1*, **B-IIp-5**, 417.
8. Stutzmann, M., Jackson, W.B., and Tsai, C.C., Phys. Rev. B, 1985. **32**(1): p. 23.
9. Han, D. and Fritzsche, H., J. Non-Cryst. Sol., 1983. **59&60**: p. 397.
10. Schumm, G., Phys. Rev. B, 1994. **49**: p. 2427.
11. Branz, H.M., Phys. Rev. B, 1999. **59**: p. 5498.
12. Brodsky, M.H. and Title, R.S., PRL, 1969. **23**(11): p. 581.
13. Chittick, R.C., Alexander, J.H., and Sterling, H.F., J. Electrochem. Soc. (USA), 1969. **116**(1): p. 77.
14. Pankove, J.I., Lampert, M.A., and Tarnag, M.L., Appl. Phys. Lett., 1978. **32**(7): p. 439.
15. Sol, N., Kaplan, D., Dieumegard, D., and Dubreuil, D., J. Non-Cryst. Solids (Netherlands), 1980. **35-36**(pt.1): p. 291.
16. Mahan, A.H., Nelson, B.P., Salamon, S., and Crandall, R.S., J. Non-Cryst. Solids (Netherlands), 1991. **137-138**(pt.2): p. 657.
17. Nakamura, N., Watanabe, K., Nishikuni, M., Hishikawa, Y., Tsuda, S., Nishiwaki, H., Ohnishi, M., and Kuwano, Y., J. Non-Cryst. Solids, 1983. **59/60**: p. 1139.
18. Stutzmann, M., Phil. Mag. B, 1987. **56**(1): p. 63.
19. Street, R.A., Physica B, 1991. **170**: p. 69.
20. Fritzsche, H., Solid State Commun., 1995. **94**(12): p. 953.
21. Fritzsche, H. in *Amorphous and Microcrystalline Silicon Technology-1997*, **467**, 19 .
22. Hata, N., Kamei, T., Okamoto, H., and Matsuda, A. in *Amorphous and Microcrystalline Silicon Technology-1997*, **467**, 61.



23. Fritzsche, H., *J Non-Cryst Solids*, 1995. **190**: p. 180.
24. Gotoh, T., Nonomura, S., Nishio, M., Masui, N., Nitta, S., Kondo, M., and Matsuda, A., *J. Non-Cryst. Solids*, 1998. **227-230**: p. 263.
25. Stutzmann, M., Nunnenkamp, J., Brandt, M.S., and Asano, A., *Phys. Rev. Lett.*, 1991. **67**(17): p. 2347.
26. Tzanetakis, P., Kopidakis, N., Androulidaki, M., Kalpouzos, C., Stradins, P., and Fritzsche, H. in *Amorphous Silicon Technology-1995*, **377**, 245.
27. Stradins, P., Kondo, M., and Matsuda, A. in *Amorphous and Heterogeneous Silicon Thin Films - 2000*, **609**, A3.1.
28. Heck, S. and Branz, H.M. in *Amorphous and Heterogeneous Silicon Thin Films: Fundamentals to Devices -1999*, **557**, 347.
29. Benatar, L., Grimbergen, M., Fahrenbruch, A., Lopez-Otero, A., Redfield, D., and Bube, R.H. in *Amorphous Silicon Technology-1992*, **258**, 461.
30. Stradins, P., Kondo, M., and Matsuda, A., *IEEE*, 2000.
31. Heck, S. and Branz, H.M., *Appl. Phys. Lett.*, 2001. **79**(19): p. 3080.
32. Stradins, P., Shimizu, S., Kondo, M., and Matsuda, A. in *Amorphous and Heterogeneous Silicon - Based Films - 2001*, **664**, A12.1.
33. Zhang, Q., Takashima, H., Zhou, J., Kumda, M., and Shimizu, T. in *Amorphous Silicon Technology-1994*, **336**, 269.
34. Zhang, Q., Takashima, H., Zhou, J., Kumda, M., and Shimizu, T., *Jpn. J. Appl. Phys.*, 1995. **34**(11, part 1): p. 5933.
35. Fuhs, W., *ANNALEN DER PHYSIK*, 1985. **42**: p. 187.
36. Qiu, C., Li, W., Han, D., and Pankove, J., *J. Appl. Phys.*, 1988. **64**(2): p. 7137.
37. Stradins, P. and Fritzsche, H., *Phil. Mag. B*, 1994. **69**: p. 121.
38. Stradins, P. and Fritzsche, H. in *Amorphous and Microcrystalline Silicon Technology-1997*, **467**, 85.
39. Cohen, M.H., Fritzsche, H., and Ovshinsky, S.R., *PRL*, 1969. **22**(20): p. 1065.
40. Tiedje, T., Cebulka, J.M., Morel, D.L., and Abeles, B., *Phys. Rev. Lett.*, 1981. **46**(21): p. 1425.
41. Hoheisel, M. and Fuhs, W., *Phil. Mag. B*, 1988. **57**: p. 411.
42. Eliat, A., Adriaenssens, G.J., and Yan, B. in *Amorphous and Microcrystalline Silicon Technology-1998*, **507**, 661.

43. Fuhs, W., Milleville, M., and Stuke, J., *Physica Status Solidi B*, 1978. **89**(2): p. 495.
44. Wang, Q., Antoniadis, H., and Schiff, E.A., *Appl. Phys. Lett.*, 1992. **60**(22): p. 2791.
  
45. Hattori, K., Hirao, T., Iida, M., and Okamoto, H., *J Non-Cryst Solids*, 2000. **266-269**: p. 352.
46. Kunst, M., *private communications*. 2002.
47. Street, R.A., *Appl. Phys. Lett.*, 1982. **41**(11): p. 1960.
48. Han, D., Melcher, D.C., Schiff, E.A., and Silver, M., *Phys. Rev. B*, 1993. **48**: p. 8658.
49. Crandall, R.S., in *Semiconductors and Semimetals*. 1984. p. 243.
50. Wronski, C.R. in *Amorphous and Microcrystalline Silicon Technology-1997*, **467**, 7.
51. Pearce, J., Niu, X., Koval, R., Ganguly, G., Carlson, D., Collins, R.W., and Wronski, C.R. in *Amorphous and Heterogeneous Silicon Thin Films - 2000*, **664**, A12.3.
52. Rose, A., *Concepts in Photoconductivity and Allied Problems*, ed. R.E. Kreiger. Vol. 12. 1963, New York: Huntington. 362.
53. Shockley, W. and Read, W.T., *Phys. Rev.*, 1952. **87**: p. 835.
54. Pierz, K., Mell, H., and Terukov, J., *J. Non-Cryst. Solids*, 1985. **77&78**: p. 547.
55. Overhof, H. and Thomas, P., *Electronic Transport in Hydrogenated Amorphous Semiconductors*. Springer Tracts in Modern Physics. Vol. 114. 1989, Berlin Heidelberg New York London Paris Tokyo: Springer-Verlag.
56. Sasaki, M., Okamoto, S., Hishikawa, Y., Tsuda, S., and Nakano, S., *Solar Energy Materials and Solar Cells*, 1994. **34**: p. 541.
57. Stoddart, H.A., Vardeny, Z., and Tauc, J., *Phys. Rev. B*, 1988. **38**(2): p. 1362.
58. Vanecek, M., Kocka, J., Stuchlik, J., Kozisek, Z., Stika, O., and Triska, A., *Sol. Energy Mater. (Netherlands)*, 1983. **8**(4): p. 411.
59. Jensen, P., *Solid State Communications*, 1990. **76**(11): p. 1301.
60. Simmons, J.G. and Taylor, G.W., *Phys. Rev. B*, 1971. **4**(2): p. 502.
61. Vaillant, F. and Jousse, D., *Phys. Rev. B*, 1986. **34**(6): p. 4088.
62. Pandya, R., Zafar, S., and Schiff, E.A. in *Materials Issues in Amorphous-Semiconductor Technology*, **70**, 155.
63. Zafar, S. and Schiff, E.A., *Thin Solid Films*, 1988. **164**: p. 239.
64. Vanecek, M., Kocka, J., Stuchlik, J., and Triska, A., *Solid State Commun.*, 1981. **39**(11): p. 1199.
65. Jackson, W.B., Nemanich, R.J., and Amer, N.M., *Phys. Rev. B*, 1983. **27**: p. 4861.

- 
66. Pierz, K., Fuhs, W., and Mell, H., *Phil. Mag. B*, 1991. **63**(1): p. 123.
  67. Lee, C., Ohlsen, W.D., Taylor, P.C., Ullal, H.S., and Ceasar, G.P., *Phys. Rev. B*, 1985. **31**: p. 100.
  68. Eser, E., *J. Appl. Phys.*, 1986. **59**(10): p. 3508.
  69. Stutzmann, M., Jackson, W.B., and Tsai, C.C., *Phys. Rev. B*, 1986. **34**(1): p. 63.
  70. Matsuura, H., *Appl. Phys. Lett.*, 1989. **54**(4): p. 344.
  71. Meyer, W. and Neldel, H., *Zeitschr. f. techn. Physik*, 1937. **12**: p. 588.
  72. Crandall, R.S., *Phys. Rev. B*, 1991. **43**(5): p. 4057.
  73. Jackson, W.B., Stutzmann, M., and Tsai, C.C., *Phys. Rev. B*, 1986. **34**(1): p. 54.
  74. Shimizu, S., Stradins, P., Kondo, M., and Matsuda, A. in *Amorphous and Heterogeneous Silicon - Based Films - 2001*, **664**, A14.2.
  75. Stutzmann, M., Nunnenkamp, J., Brandt, M.S., Asano, A., and Rossi, M.C., *J. Non-Cryst. Solids*, 1991. **137-138**: p. 231.
  76. Tzanetakis, P., Kopidakis, N., and Fritzsche, H., *J. Non-Cryst. Solids*, 1996. **198-200**: p. 276.
  77. Stradins, P. and Fritzsche, H., *J. Non-Cryst. Solids*, 1996. **198-200**: p. 432.
  78. Tzanetakis, P., Kopidakis, N., Androulidaki, M., Kalpouzios, C., Stradins, P., and Fritzsche, H., *J. Non-Cryst. Solids*, 1996. **198-200**: p. 458.
  79. Stradins, P., Kondo, M., and Matsuda, A., *J. Non-Cryst Solids*, 2000. **266-269**: p. 405.
  80. Zapletal, J., Fejfar, A., Hamied, S.F.A., Sipek, E., Pelant, I., Kocka, J., Juska, G., Yokoi, T., Azuma, M., Mahan, H., and Crandall, R.S. in *12th E-PVSEC*.
  81. Hof, C., Ziegler, Y., Platz, N., Wyrsh, N., and Shah, A. in *17th International Conference on Amorphous and Microcrystalline Semiconductors - Science and Technology (ICAMS 17)*, **227-230**, 287.
  82. Nonomura, S., Yoshida, N., Gotoh, T., Sakamoto, T., Kondo, M., Matsuda, A., and Nitta, S., *J. Non-Cryst Solids*, 2000. **266-269**: p. 474.
  83. Masson, D.P., Ouhlal, A., and Yelon, A., *J Non-Cryst Solids*, 1995. **190**(1-2): p. 151.
  84. footnote, *see e.g., Proceedings of the 18. ICAMS, J. Non-Cryst. Solids 266-269*.
  85. Stradins, P., Tran, M., and Fritzsche, H., *J. Non-Cryst Solids*, 1993. **164-166**: p. 175.
  86. Skumanich, A., Amer, N.M., and Jackson, W.B., *Phys. Rev. B*, 1985. **31**(4): p. 2263.
  87. Tran, M., Fritzsche, H., and Stradins, P. in *Amorphous Silicon Technology-1993*, **297**, 195.

88. Mahan, A.H. and Vanecek, M., AIP Conference Proceedings, 1991(234): p. 195.
89. Irsigler, P., Wagner, D., and Dunstan, D.J., Solid State Phys., 1983. **16**: p. 6605.
90. Jackson, W.B. and Stutzmann, M., Appl. Phys. Lett., 1986. **49**(15): p. 957.
91. Bube, R.H., Benatar, L., and Bube, K.P., J. Appl. Phys., 1996. **79**(4): p. 1926.
  
92. Schumm, G. and Bauer, G.H., Phys. Rev. B, 1989. **39**(8): p. 5311.
93. Zhang, Q., Kumda, M., and Shimizu, T., Jpn. J. Appl. Phys., 1993. **32**: p. L371.
  
94. Shepard, K., Smith, Z.E., Aljishi, S., and Wagner, S., Appl. Phys. Lett., 1988. **53**(17): p. 1644.
95. Stradins, P., Kondo, M., Hata, N., and Matsuda, A. in *Amorphous and Microcrystalline Silicon Technology-1998*, **507**, 723.
96. Street, R.A., Phys. Rev. B, 1981. **23**(2): p. 861.
97. Hauschildt, D., Fuhs, W., and Mell, H., Phys. Stat. Sol. (B), 1982. **111**: p. 171.
98. Jiao, L., Semoushikina, S., Lee, Y., and Wronski, C.R. in *Amorphous and Microcrystalline Silicon Technology-1997*, **467**, 233.
99. Wronski, C.R., J. Non-Cryst. Sol., 1983. **59&60**: p. 401.
100. Ganguly, G., Yamasaki, S., and Matsuda, A., Phil. Mag. B, 1991. **63**(1): p. 281.
101. Sakata, I., Yamanaka, M., Numase, S., and Hayashi, Y., Jpn. J. Appl. Phys., 1991. **30**(9B): p. L1616.
102. Gunes, M. and Wronski, C.R., Appl. Phys. Lett., 1992. **61**(6): p. 678.
103. Yang, L. and Chen, L., Appl. Phys. Lett., 1993. **63**(3): p. 400.
104. Tanielian, M.H., Goodman, N.B., and Fritzsche, H., J. de Physique, 1981. **42**: p. C4.
105. Guha, S., Huang, C.Y., and Hudgens, S.J., Phys. Rev. B, 1984. **29**(10): p. 5995.
106. Branz, H.M. and Silver, M., Phys. Rev. B, 1990. **42**(12): p. 7420.
107. Stutzmann, M., in *Amorphous and Microcrystalline Semiconductor Devices, Vol. II: Materials and Device Physics*, J. Kanicki, Editor. 1992, Artech House: Boston. p. 129.
108. Seager, C.H. and Anderson, R.A., Appl. Phys. Lett., 1988. **53**: p. 1181.
109. Van de Walle, C.G., Denteneer, P.J.H., Bar-Yam, Y., and Pantelides, S.T., Phys. Rev. B, 1989. **39**: p. 10791.
110. Siebke, F., Stiebig, H., Abo-Arais, A., and Wagner, H., Solar Energy Materials and Solar Cells, 1996. **41/42**: p. 529 .
111. Schumm, G., Nitsch, K., and Bauer, G.H., Phil. Mag. B, 1988. **58**: p. 411.

## Acknowledgements

I am grateful for all the help that I received during my graduation program. This work would not have been possible without the support of many people.

First of all I want to thank Prof. Dr. Walther Fuhs, who agreed to supervise this project and made it possible to conduct the major part of my work at the National Renewable Energy Laboratory (NREL). Special thanks to Dr. Howard Branz at NREL, who not only supervised and frequently discussed my work with me, but also cleared in front and behind the scenes bureaucratic obstacles, connected to being an 'alien' in the USA. Beyond his duties as supervisor, he made the research we shared as interesting and enjoyable as possible.

My thanks to Prof. Dr. P. Thomas, who agreed to co-referee this thesis, and to Prof. Dr. G. Weiser and Prof. Dr. H. Bäßler who agreed to be on my defense committee.

The diversity of research is reflected in my thesis by the different places where my samples came from. I want to thank H. Fritzsche (University of Chicago), C. Wronski (Penn State University), A. Matsuda, P. Stradins (both National Institute of Advanced Industrial Science and Technology), H. Mell (University of Marburg) and B. Nelson (NREL) for growing and providing samples.

I always enjoyed and greatly appreciate the discussions with R. Crandall, P. Stradins and M. Stutzmann. Also, Prof. Stutzmann was so kind to borrow me the sample with pre-deposited Ni-meander for sample temperature measurements.

For technical help I want to thank B. Nelson. If he did not have an answer, he knew somebody who should. Q. Wang gave me a great deal of help and set an example of calm and patience whenever it came to computer problems. P. Tzanetakis took the time during a busy sabbatical visit to build a fast current-to-voltage converter for my research. All the members of the amorphous Silicon group had always an open ear for my requests for help, which I gratefully acknowledge.

Every research has, like life, its ups and downs. I thank all my friends who helped me to stay sane during my down periods and to see beyond such times. Representative for all who I cannot list for lack of space, I name Bill McMahon. He introduced me to rock climbing and to a great number of very interesting people. His encouragements based on his experience as grad student were at times invaluable.

Solveig Anders read with patience and at times under pressure my manuscript. Her advice and support reached far beyond such technical help and cannot easily be expressed, therefore I leave it.

## Lebenslauf

- 26.04.1963 geboren in Karlsruhe
- 1969 - 78 Grund- und Hauptschule Elchesheim-Illingen
- 1978 - 82 Berufsausbildung zum Elektroinstallateur
- 1982 - 83 Berufsaufbauschule in Rastatt mit Abschluss der Mittleren Reife
- 1983 - 86 Kolping Kolleg in Rheinstetten mit Abschluss der Allgemeinen Hochschulreife
- 1986 – 88 Zivildienst
- 1988 - 95 Physikstudium an der Universität Tübingen
- 1995 - 96 Wissenschaftlicher Mitarbeiter and der University of Chicago, USA.
- 1997 - 01 Wissenschaftlicher Mitarbeiter in der Forschungsgruppe “Amorphes Silizium” am National Renewable Energy Laboratory, Golden, CO
- 2001 – 02 Wissenschaftlicher Mitarbeiter am Hahn-Meitner-Institut Berlin